Synthesis and electrochemical properties of high-entropy spinel oxides, cobalt atomic clusters and zinc oxide as electrode materials for rechargeable zinc-air batteries

Lesego Gaolatlhe (1683815)

A thesis presented to the University of the Witwatersrand in fulfillment of the thesis requirement for the degree of Doctor of Philosophy in Chemistry

Supervisor

Professor Kenneth I. Ozoemena

2024

DECLARATION

I affirm that this thesis was independently researched and is a faithful record of the original research work that I carried out. All sources have been quoted, indicated, and supported by a list of citations. The thesis is being presented to the School of Chemistry, Faculty of Science at the University of the Witwatersrand for consideration for a Doctor of Philosophy degree. This work has never before been submitted in whole or in part to a different higher education institution for consideration of any degree.

Signature:  Date: 25 July 2024

DEDICATION

This document is dedicated to my family, with loving memories of my grandparents Thabo Jacob Tladi and Kedibone Margret Tladi.

ACKNOWLEDGEMENTS

The completion of this thesis is deeply indebted to the support and encouragement I have received from numerous individuals. I extend my sincere gratitude and appreciation to the following people for their invaluable guidance and assistance.

My unwavering gratitude goes to God, all praise, glory, and honor to Him. This work would not be possible if it was not for His spirit which enables me.

My deepest gratitude goes to Professor Kenneth I. Ozoemena, my PhD supervisor. His unwavering belief in my potential and willingness to guide me into a new field of study was instrumental in this project's success. I am particularly thankful for his constant support, insightful guidance, and encouragement throughout my studies.

A special thank you to Dr. Adewale Ipadeola for always availing himself to assist in laboratory experiments, helping me understand certain concepts, proofreading my work, and counsel from my MSc throughout my PhD studies.

I would like to thank Dr. Aderemi Haruna for his eye for detail, synthesis skills, and insightful directions throughout this work.

To Professor Caren Billing and Professor Neil J. Covil for opening their research laboratories and allowing the use of their equipment. Their assistance has been instrumental in the successful completion of my research project.

I would like to thank all of my colleagues and friends who have helped me along the way. Dr. Thapelo Mofokeng, Dr. Augustus K. Lebechi, Miss Refiloe P. Modise, Dr. Patrick V.Mwonga, and Miss Petra Dinham for their contribution throughout this work.

Additionally, I would like to express my gratitude to my friends, cousins, and colleagues during this trying road. Although it was not simple, your encouragement and inspiration kept me going.

My gratitude goes to the staff members of the Microscopy and Microanalysis Unit (MMU) at the University of the Witwatersrand for giving training and support with electron microscopy work.

An extended gratitude to the Materials Electrochemistry and Energy Technologies (MEET) and Catalysis and Materials (CAT-MAT) for their tremendous assistance and collaboration during this study. Their insightful discussions and readiness to share their expertise during group meetings played a big role in my research findings.

This work would not have been possible without funding from the National Research Foundation (NRF) and the Department of Science and Innovation (DSI) under the Freestanding, Innovation and Scarce Skills Development Fund Masters scholarship, and the University of the Witwatersrand Postgraduate Merit Award (PMA) for financial support throughout my PhD project.

Lastly, to my family my late grandparents, Kedibone Margret Tladi and Thabo Jacob Tladi, this is bittersweet, I had wished that you would cross the finish line with me. But I know you are as proud of me in the next life as you would have been in this one. To my mother Moira Gaolatlhe and father Peter Gaolatlhe, I thank you for your prayers that kept me going when I did not have the strength to. To my bother Kagiso Gaolatlhe and my two beautiful nieces, thank you for always cheering me on.

RESEARCH OUTPUTS

List of publications

1. **L. Gaolatlhe**, A.K. Lebechi, A.B. Haruna, T.P. Mofokeng, A.K. Ipadeola, O.E. Bankole, K.I. Ozoemena, Co atomic clusters MOF-derived carbon for high-performance oxygen electrochemistry and rechargeable zinc-air battery, Electrochimica Acta, 2024 (Under review).

2. **L. Gaolatlhe**, A.K. Lebechi, A.B. Haruna, T.P. Mofokeng, K.I. Ozoemena, Noble metal-free bifunctional high-entropy spinel oxide for reversible zinc-air battery, Energy and Environmental Science, 2024 (Under review).

3. **L. Gaolatlhe**, K.I. Ozoemena, Polymer-coated zinc oxide: a promising anode material for next-generation rechargeable zinc-air batteries, Energy Advances, 2024 (Under review).

4. A.K. Ipadeola, A.K. Lebechi, **L. Gaolatlhe**, Aderemi B. Haruna, Mira Chitt, Kamel Eid, Aboubakr M. Abdullah, Kenneth I. Ozoemena, Porous high-entropy alloys as efficient electrocatalysts for water-splitting reactions, Electrochemistry Communications, **136** (2022) 107207.

5. Dr. A.K. Ipadeola, Dr. A.B. Haruna, **L. Gaolatlhe**, A.K. Lebechi, Dr. J. Meng, Prof. Q. Pang, Dr. K. Eid, Prof. A.M. Abdullah, Prof. K.I. Ozoemena, Efforts at enhancing bifunctional electrocatalysis and related events for rechargeable zinc-air batteries, ElectroChemChem, **8** (2021) 3998-4018.

6. Dr. A.K. Ipadeola, Dr. A.B. Haruna, **L. Gaolatlhe**, A.K. Lebechi, Dr. J. Meng, Prof. Q. Pang, Dr. K. Eid, Prof. A.M. Abdullah, Prof. K.I. Ozoemena, Cover profile: efforts at enhancing bifunctional electrocatalysis and related events for rechargeable zinc-air batteries, ElectroChemChem, **8** (2021) 3992-3992.

PATENT

K.I. Ozoemena, A.B. Haruna, **L. Gaolatlhe**, A.M. Mongwe, Rechargeable metal-air batteries, electrocatalysts and high-entropy materials thereof, Provisional Patent, European Patent Office, Serial No. 2037911, Filed 10 June 2024.

PRESENTATIONS

1. L. Gaolatlhe, A.K. Lebechi, A.B. Haruna, Kenneth I. Ozoemena “Starved Co-MOF-derived carbon as an electrocatalyst for alkaline oxygen reactions for rechargeable zinc-air battery” Poster presentation at the 33rd Annual meeting of the Catalysis Society of South Africa (CATSA), 2023.

2. L. Gaolatlhe, K.I Ozoemena “Polymer coated zinc oxide as a potential anode material in rechargeable zinc-air batteries” Oral presentation at the 32nd Annual meeting of the Catalysis Society of South Africa (CATSA), 2022.

PROFESSIONAL ASSOCIATION

1. Member, South African Chemical Institute.

2. Member, International Society of Electrochemistry.

AWARDS, HONOURS AND PRICES

1. Awarded the prestigious s DSI-NRF Centre of Excellence in Strong Materials, 2020-2023.

2. Postgraduate Merit Award at the University of the Witwatersrand, Johannesburg, South Africa, 2020-2023.

3. Paper featured on the cover of ChemElectroChem 2021, European Chemical Societies Publishing, Wiley-VCH.

ABSTRACT

This thesis investigated cathode and anode electrode materials for application in rechargeable zinc-air battery (RZAB). Two types of cathode materials were strategically studied in RZAB applications: (a) **cobalt carbon composites** of (i) cobalt atomic clusters (Co AC@C_{BPDC}) and (ii) cobalt nanoparticles (Co NP@C_{BPDC}), and (b) **high-entropy spinel oxide** (HESOx, containing five transition metals – Cu, Mn, Fe, Ni, and Co). The activities of these materials toward oxygen reduction reaction (ORR) and oxygen evolution reaction (OER) were investigated in both half- and full-cell configurations as a proof-of-concept in RZAB cells in alkaline electrolyte. Considering that conventional zinc plate has several short-comings as an anode for RZAB, a new material, polydopamine-derived carbon-coated zinc oxide (ZnO@PDA-DC), was also synthesised and applied in RZAB as a possible alternative anode to the popular zinc plate.

First, Co AC@C_{BPDC} and Co NP@C_{BPDC} were prepared using the metal-organic framework (MOF) route through the microwave-assisted solvothermal method and acid treatment. From the XRD results, the spectra showed dominant {111} and {200} phases, characteristic of metallic cobalt with a face-centred cubic (fcc). There were trace amounts of CoO observed indicating the coexistence of Co/CoO. From TEM imaging, Co AC@C_{BPDC} was highly defective with a visible porous carbon structure than its counterpart (Co NP@C_{BPDC}) and showed dispersed atomic clusters. BET data showed that Co AC@C_{BPDC} had a higher surface area (144.8 m^2/g) than the Co NP@C_{BPDC} (33.25 m^2/g). The improved physicochemical merits of the Co AC@C_{BPDC} allowed for better ORR and OER activities than the Co NP@C_{BPDC} in terms of low half-way potential ($E_{1/2}$), onset potential (E_{onset}), overpotential at 10 mA/cm^2 (η_{10}), potential gap (ΔE) between the overpotential of OER and the halfway potential, and a higher kinetic current density (j_k). The enhanced electrochemistry of the Co AC@C_{BPDC} was attributed to the defects created by the acid treatment. As proof of real-life applicability, the Co AC@C_{BPDC} electrocatalyst delivered an excellent air cathode in a parallel plate RZAB cell with notable OCV (1.23 V), peak power density (49.9 mW/cm^2), areal energy density (477 mAh/cm^2), long-term stability for 210 h, enhanced voltage

retention, Coulombic efficiency (ca. 100 %) and DOD (51.3%), comparable to literature. In addition, an all-solid-state RZAB based on the Co AC@C_{BPDC} catalyst gave a higher and constant OCV (1.73 V) at varied bending angles (0 – 180 degrees) and excellent stability.

Second, new HESOx materials were prepared via the Pechini method at two different annealing temperatures of 500 and 750 ^{o}C (abbreviated herein as HESOx-500 and HESOx-750). P-XRD results showed that these are inverse spinel oxides, with {311} as the dominant phase. HR-TEM images proved that they are single nanocrystalline materials. XRD and BET data showed that the HESOx-500 is smaller in size, more porous, and has a higher surface area than its counterpart (HESOx-750). HESOx-500 showed superior ORR performance with an onset potential of 0.93 V and a $E_{1/2}$ of 0.88 mV. The OER performance also showed improved η_{10} compared to IrO_2 with an overpotential of 340 mV at a current density of 10 mA/cm^2, and a 45 $\pm$ 5.0 mV/dec Tafel slope, above the performance of IrO_2 (66 $\pm$ 6.1 V/dec). The ΔE of HESOx-500 was 0.69 V. The material was further tested as a cathode material in a RZAB cell. The optimised RZAB cell showed remarkable performance with a theoretical potential of 1.67 V and long-term stability of 375 h at 10 mA/cm^2. The performance was attributed to the high-entropy compositional design with a high number of surface oxygen vacancies and different metal oxidation states.

Finally, having dealt with the issue of bifunctionality in RZAB, a new ZnO@C anode material was also considered. The ZnO@PDA-DC (where PDA-DC means polydopamine-derived carbon) was used due to its ability to form Zn^{2+} pathways. Electrochemical potentiodynamic polarisation tests were performed to understand and compare the corrosion inhibition effects in an alkaline medium (6 M KOH). The ZnO@PDA-DC showed better corrosion inhibition properties than the zinc plate and other samples: low corrosion current (i_{corr} = 0.107 uA/cm^2) and corrosion potential (E_{corr} = 1.077 V), and a mixed inhibition effect, indicating reduced hydrogen evolution reaction and zinc dissolution. Due to the excellent corrosion inhibition properties of the ZnO@PDA-DC, it was then evaluated in the RZAB cell. The shallow galvanostatic charge-discharge cycle stability at 2 mA/cm^2 was able to maintain 150 h in a RZAB at a voltage gap of 0.76 V to 0.80 V. The results demonstrated that enhanced rechargeability is possible with ZnO@PDA-DC for RZAB.

TABLE OF CONTENTS

LIST OF FIGURES

LIST OF TABLES

LIST OF SCHEMES

NOMENCLATURE

A_{Zn}:	Geometric area of the zinc anode
$A_{cathode}$	Geometric area of the air cathode
β:	Absorption equilibrium constant/Full-width at half-maximum
BI:	Bifunctionality index
C_{o_2}:	Oxygen concentration
C_{dl}:	Double layer capacitance
CPE1:	Constant phase element of the double layer capacitance
CPE2:	Constant phase element of the surface film resistance
$E_{1/2}$:	Half-wave potential
E_{corr}:	Corrosion potential
E_{onset}:	Onset potential
eV:	Electron volt
F:	Faraday Constant
h_{Zn}	height of the Zn
i_{corr}:	Corrosion current density
j:	Current density
j_d/j_L:	Diffusion-limiting current
j_k:	Kinetic current density
K-L:	Koutecky-Levich
mA/cm^2:	Milliampere per square centimetre
mAh/cm^2:	Milliampere hour per square centimetre
mAh/g_{Zn}:	Milliampere hour per gram of zinc
mg/cm^2:	Milligram per square centimetre

mAh/cm^3:	Milliampere
mV/dec:	Millivolt(s) per decade
mV/s:	Millivolt(s) per second
mW/cm^2:	Milliwatt per square centimetre
N:	Number of equimolar components
ρ_{Zn}:	Bulk Zn density
S_{mix}:	Mixing entropy
$\mu A/cm^2$:	Microampere per square centimetre
γ:	Kinematic viscosity
V_{Zn}:	Volume of the Zn electrode
Wh/kg:	Watt hour per kilogram
ω:	Angular frequency/Rotation speed
φ:	Work function
Z':	Imaginary impedance
Z'':	Real impedance
η_{10}:	OER potential at current density of 10 mA/cm^2
η:	Overpotential
ΔE:	The difference between onset potential and half-wave potential

LIST OF ABBREVIATIONS

Ar:	Argon
Ag/AgCl:	Silver-silver chloride
BET:	Brunauer-Emmett-Teller
BPDC:	4.4-Biphenyldicarboxylic acid
CB:	Carbon black
CCAs:	Complex concentrated alloys
CD:	Charge-discharge
CIF:	Crystallographic information file
Co AC@C_{BPDC}:	Cobalt atomic clusters MOF-derived carbon
Co NP@C_{BPDC}:	Cobalt nanoparticles MOF derived carbon
DOD:	Depth of discharge
E_{corr}:	Corrosion current
E_f:	Fermi energy
$E_{cut-off}$:	High-binding-energy secondary cut-off
E_{VBM}:	Valence band maximum
EIS:	Electrochemical impedance spectroscopy
EDS:	Energy Dispersive X-Ray Spectroscopy
EG:	Ethylene glycol
EPR:	Electron paramagnetic resonance spectroscopy
FT-IR	Fourier-transform infra-red spectroscopy
GCD:	Galvanostatic charge-discharge
HEA:	High-entropy alloy
HEO:	High-entropy oxide
HER:	Hydrogen evolution reaction

HESOx	High-entropy spinel oxide
HESOx-500:	High-entropy spinel oxide annealed at 500 ^{o}C
HESOx-750:	High-entropy spinel oxide annealed at 750 ^{o}C
hv:	Incident photon energy
IL:	Ionic liquid
IP:	Ionisation potential
LSV:	Linear sweep voltammetry
LPR:	Linear polarisation resistance
MAB:	Metal-air battery
MOF:	Metal-organic framework
MPEAs:	Multiple principal element alloys
N_2:	Nitrogen gas
O_C:	Chemisorbed oxygen
O_V:	Oxygen vacancy
O_L:	Lattice oxygen
OCV:	Open circuit voltage
OCP:	Open circuit potential
OER:	Oxygen evolution reaction
ORR:	Oxygen reduction reaction
PTFE	Poly(tetrafluoroethylene)
PDA:	Polydopamine
PVA:	Poly(vinyl alcohol)
P-XRD:	Powder X-ray diffraction
R_p:	Polarisation resistance
RDE:	Rotating disk electrode
RRDE:	Rotating ring disk electrode

RHE	Reversible hydrogen electrode
RTIL:	Room temperature ionic liquid
rpm:	Rotations per minute
RZAB:	Rechargeable zinc-air battery
SEM:	Scanning electron microscopy
TEM:	Transmission electron microscopy
TGA:	Thermogravimetric analysis
UPS:	Ultraviolet photoelectron spectroscopy
XPS:	X-ray photoelectron spectroscopy
ZIF:	Zeolitic imidazolate framework
ZAB:	Zinc-air battery
ZnO@PDA-DC:	Zinc oxide coated polydopamine derived carbon
$Zn(OH)_4^{2-}$:	Zincate ions

CHAPTER 1
INTRODUCTION

This chapter provides an overview of the motivation and rationale, the objectives, and the outline of the thesis.

1.1. Motivation and rationale

The increasing energy demand, driven by the growth of electric vehicles and portable electronic devices, coupled with the depletion of fossil fuels and the urgent need to address climate change, has spurred the exploration of alternative renewable energy resources for a clean energy economy. Technological innovations for reliable production, storage, and use of renewable energy are at the core of current energy research [1]. Renewable energy is projected to account for a significant portion of the overall electrical energy during the next coming years. Batteries are known as great energy-storage and conversion devices and they have several applications ranging from small devices like watches to electric vehicles (EVs) and grid-scale storage. Lithium-ion batteries dominate the energy storage application industry, however, there is a depletion of lithium metal deposits, which will continue to increase its cost due to the lowering global supply, more obvious as demand increases. Another disadvantage of the use of Lithium (Li) is its safety concerns and temperature sensitivity.

Proposed and pursued alternatives have been Li^+, Na^+, K^+, Mg^{2+}, and/or metal ion (Li; Ca; Mg; Al; Zn; Fe), and metal-air batteries (MABs). Besides its low cost and non-toxicity characteristic (depending on the specific metal employed), MABs have attracted significant interest owing to the incorporation of gaseous oxygen from the surrounding environment as an active cathode component, which is infinitely available due to the open-cell architecture. This affords the battery with exceptional energy density, consistent discharge voltage, extended shelf life, and affordability. Zinc-air batteries (ZAB) have attracted significant attention due to the abundance of zinc, high theoretical energy density (1 086 Wh/kg), and specific energy density (470 Wh/kg) which is twice that of the state-of-the-art lithium-ion batteries (200 Wh/kg) [2], constant discharge voltage, low weight, reversibility and good stability in aqueous electrolytes [3], safety and environmental friendliness of operation. The volumetric capacity of Zinc

(5 854 mAh/cm^3) is almost three times higher than that of Li (2 062 mAh/cm^3) [4]. The primary (non-rechargeable) ZAB has been applied in portable devices such as hearing aids, navigation devices, railway signal devices, and telecommunication applications.

Rechargeable Zinc-air batteries (RZABs) are considered more attractive. This is because they have less environmental impact than primary cells, in that they are reusable and cost-effective. RZABs can be used to store and deliver high energy for portable and stationary devices as well as for the operation of electric vehicles. Despite progress in developing RZABs, performance has been hampered by limitations in the air cathode. The sluggish nature of oxygen reactions (reduction and evolution) at the cathode leads to potential deviation from the standard potential during galvanostatic charging and discharging. This is because the actual voltage deviates from the ideal during operation, reducing overall energy output. To address this challenge, researchers are seeking efficient and durable catalysts for both oxygen reduction and evolution reactions. While precious metals like platinum have been used, their high cost, scarcity, and limited stability in the battery's environment necessitate the exploration of more sustainable alternatives. For RZABs to reach their full potential in terms of energy storage capacity, the air cathode needs to excel at facilitating both oxygen reactions. Ideally, the cathode material should be a powerful oxidiser, remain stable in the electrolyte, boast strong redox properties with high capacity, and exhibit exceptional cycling stability.

Unlike the air cathode, limitations in the zinc anode of RZABs stem from the complex chemical reactions involved between the solid-solute-solid (Zn-$Zn(OH)_4^{2-}$-ZnO) interface. The amount of usable energy is directly tied to the amount of zinc available in the anode. Once the zinc is depleted, the battery can no longer function. Several factors hindering the efficient utilisation of zinc include; (i) corrosion caused by the production of hydrogen gas, (ii) change in the zinc surface forming needle-like structures (dendrites), and (iii) formation of irreversible zinc oxide layer (passivation layer). These issues lead to a decrease in battery capacity (capacity fade), inefficient charging (low Columbic efficiency), and a shortened lifespan (poor cyclability and stability). Scientists are exploring various strategies to improve the anode performance. One approach involves coating the zinc anode with materials like metal oxides, polymers, or carbon, or incorporating specific elements like aluminium,

cadmium, or bismuth oxide. These coatings can help prevent physical changes in the anode by stabilising its structure, allowing for better utilisation and retention of the zinc structure. Alternative zinc structures, such as zinc foam and zinc oxide, are also being investigated. These modifications can further enhance conductivity, distribute current more evenly, and promote the formation of smoother, thinner zinc deposits during discharge.

Motivated by the arguments listed above, transition metal-based electrocatalysts have emerged as promising electrocatalysts to replace Pt group metals [5]. This work studied i) cobalt nanoparticles (Co NP@C_{BPDC}) and cobalt atomic clusters (Co AC@C_{BPDC}) metal-organic framework-derived carbon and ii) high-entropy spinel oxide (HESOx) as cathode materials in RZAB applications. Co/C has been widely regarded as an effective electrocatalyst for OER and ORR. HESOx has characteristics like excellent stability, improved corrosion resistance, a high number of active species, electrochemical and catalytic properties [6], to mention a few. These materials were explored for their potential to improve OER and ORR and to maintain excellent stability in RZAB. On the anode side, ZnO was employed as an alternative zinc anode to facilitate Zn^{2+} ion transport pathways. Polydopamine (PDA) was chosen as a corrosion inhibitor for its exceptional adhesion to various materials and its ability to hinder the movement of corrosive ions, (as demonstrated in [7]).

1.2. Aim and objectives of the study

1.2.1. Aim

This work focused on developing cathode material of i) cobalt nanoparticles (Co NP@C_{BPDC}) and cobalt atomic clusters (Co AC@C_{BPDC}) of metal-organic framework (MOF) derived carbon, and ii) high-entropy spinel oxide (HESOx) as cathode materials and iii) polydopamine coated zinc oxide (ZnO@PDA-DC) as an anode material in RZAB applications.

1.2.2. Objectives

The objectives of the study are as follows:

- To synthesise cobalt nanoparticles (Co NP@C_{BPDC}) and cobalt atomic clusters (Co AC@C_{BPDC}) by use of metal-organic framework (MOF) template through microwave, heat- and acid-treatment.

- To synthesise ZnO through conventional and microwave approaches and coat it with polydopamine.

- To study the physical characterisation of the synthesised materials.

- To investigate the electrochemical oxygen reaction properties and performance of Co NP@C_{BPDC}, Co AC@C_{BPDC}, HESOx-500 and HESOx-750.

- To investigate the corrosion-resistant properties of the coated zinc oxide nanoparticles in an alkaline saturated solution.

- To assess the RZAB response of Co NP@C_{BPDC}, Co AC@C_{BPDC}, HESOx-500 and HESOx-750 as cathode materials and zinc plate as an anode material in an alkaline electrolyte.

- To assess the response to ZnO@PDA-DC as anode material in RZAB with the use of the best performing synthesised air cathode in an alkaline electrolyte.

1.3. Outline of the thesis

Chapter 1 (Introduction): This chapter provides the motivation of the thesis and presents the objectives of the study.

Chapter 2 (Literature review): This chapter details the literature review on air cathode electrocatalysts and alternative anode materials in ZABs.

Chapter 3 (Experimental procedure): This chapter details the physical techniques and conditions used in this study.

Chapter 4 (Results and discussion): This chapter provides the results and discussion of Co NP@C_{BPDC} and Co AC@C_{BPDC} as a cathode electrocatalyst in ZAB.

Chapter 5 (Results and discussion): This chapter provides the results and discussion of HESOx as a cathode electrocatalyst in ZAB.

Chapter 6 (Results and discussion): This chapter provides the results and discussion of ZnO@PDA-DC-based anode materials in ZAB.

Chapter 7 (Conclusion and recommendations): This chapter provides the general concluding remarks and recommendations.

1.4. References

[1] P. Gu, M. Zheng, Q. Zhao, X. Xiao, H. Xue, H. Pang, Rechargeable zinc-air batteries: A promising way to green energy, J Mater Chem A Mater 5 (2017) 7651–7666. doi.org/10.1039/c7ta01693j.

[2] H. Ma, B. Wang, Y. Fan, W. Hong, Development and characterization of an electrically rechargeable zinc-air battery stack, Energies (Basel) 7 (2014) 6549–6557. doi.org/10.3390/en7106549.

[3] Y. Li, H. Dai, Recent advances in zinc-air batteries, Chem Soc Rev 43 (2014) 5257. doi.org/10.1039/c4cs00015c.

[4] Y. Wu, Y. Zhang, Y. Ma, J.D. Howe, H. Yang, P. Chen, S. Aluri, N. Liu, Ion-sieving carbon nanoshells for deeply rechargeable Zn-based aqueous batteries, Adv Energy Mater 8 (2018) 1802470. doi.org/10.1002/aenm.201802470.

[5] A.B. Haruna, K.I. Ozoemena, Manganese-based bifunctional electrocatalysts for zinc-air batteries, Curr Opin Electrochem 21 (2020) 219–224. doi.org/10.1016/j.coelec.2020.02.021.

[6] C.M. Rost, E. Sachet, T. Borman, A. Moballegh, E.C. Dickey, D. Hou, J.L. Jones, S. Curtarolo, J. Maria, Entropy-stabilized oxides, Nat Commun 6 (2015) 8485. doi.org/10.1038/ncomms9485.

[7] H.D. Zhang, A.Y. Chen, B. Gan, H. Jiang, L.J. Gu, Corrosion protection investigations of carbon dots and polydopamine composite coating on magnesium alloy, Journal of Magnesium and Alloys 10 (2022) 1358–1367. doi.org/10.1016/j.jma.2020.11.021.

CHAPTER 2
LITERATURE REVIEW

While wind and solar power are environmentally friendly and can meet some of our energy needs, their energy output can be unpredictable as they rely on specific conditions for peak performance. Electrochemical energy storage systems are the next generation of energy devices, due to their capacity to convert and store electrical energy and shift the energy demand from fossil fuels and the peak-trough fluctuation of the electrical grid. Their applications stretch from small portable electronic devices to powering electric vehicles and grid-scale energy storage.

2.1. Metal-air batteries

2.1.1. Metal-air batteries

The design of MABs is that of a traditional battery and a fuel cell battery. The traditional battery component uses a metal as the negative electrode and the fuel cell component uses a porous positive electrode. They use air or oxygen feedstock for energy storage and conversion. These batteries have received a great deal of interest as potential energy alternatives to the current lithium-ion batteries (LIBs) due to their high energy density. Rechargeable MABs are praised as promising electrochemical energy storage for the next generation of energy storage technologies, with applications ranging from large-scale energy storage systems to electric vehicles and handheld electronics. The potential produced in these batteries depends on the anodic metal species (Ca, Al, Li, Na, K, Mg, Fe, Cd, and Zn), their performance is summarised in Figure 2.1. These devices operate in different electrolytes including aqueous, non-aqueous, quasi-solid, and hybrid electrolytes. Typically, MABs are classified into aqueous electrolyte-based cell systems.

Lithium-air (Li-air) batteries operating in a non-aqueous system do not have the critical pure oxygen atmosphere issues. To achieve practical application, there are still important challenges that need to be addressed such as the large decomposition overpotential of lithium peroxide during charge and its clogging at the porous channels of the cathode during discharge [1]. While aqueous and solid systems lack the critical

problems found in the non-aqueous system, they have not demonstrated the ability to achieve high power density and prolonged deep cycling [2].

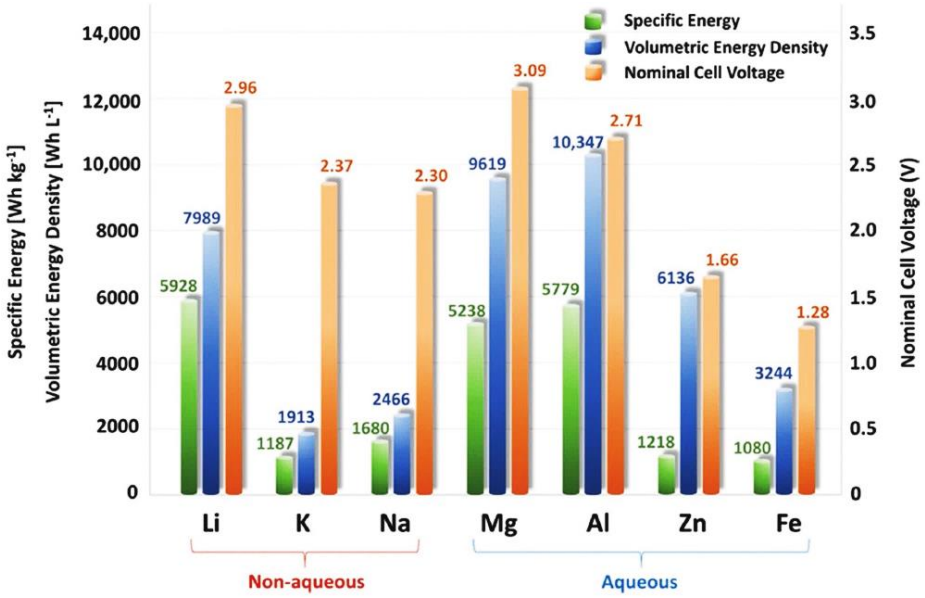

Figure 2.1: Specific energy, volumetric energy density and nominal cell voltage of RMABs [3].

The development of a potassium-air (K-air) battery is still in its early stages, though it has higher redox kinetics its round-trip efficiency is lower than lithium-ion batteries [4]. Sodium-air (Na-air) batteries have sparked widespread interest and quick development for application in electrochemical energy storage [5]. This was because of its inexpensive cost, abundance of precursor material, high theoretical specific capacity, and high energy density. However, it suffers from low catalytic activity of oxygen redox processes which cause low reversibility of charge-discharge processes as well as sodium dendrite development at the anode [5]. Aluminium air (Al-air) batteries have higher energy density than ZABs, but they easily corrode than Zn [6]. Magnesium-air (Mg-air) batteries on the other hand have discharge products ($Mg(OH)_2$, MgO, and MgO_2) that are difficult to decompose at moderate voltage ranges because of their stable thermodynamics and poor kinetic properties which make high rechargeability challenging to develop [5].

Zinc-air (Zn-air) battery is the most developed of the MABs. In light of all the environmental, economic, and electrochemical properties, Zn is the most promising contender among the other MABs. However, their commercial products are primarily

meant for low-power applications like small hearing aids, due to the limited rate capabilities of inefficient air catalyst However, their commercial products are primarily meant for low-power applications like small hearing aids, due to the limited rate capabilities of inefficient air catalysts and poor reversibility of the anode [7]. RZABs have a low energy efficiency of less than 60% because of the high overpotentials at the air cathode [7]. These batteries also suffer from poor cycle life due to a lack of reliable bifunctional electrocatalysts and cyclable metal anodes. Deep cycling batteries at high currents exacerbate this weakness even more.

There are three types of MAB storage configurations shown in Figure 2.2. The static battery configuration in Figure 2.2a is the standard stacked battery with a positive and negative electrode, a separator, and an electrolyte all housed in one compartment. This battery type can be in the form of a parallel plate cell, a coin cell, or a pouch cell configuration. The parallel plate design battery is used in this thesis with more detail in the sections below. This type of battery setup has been extensively reported, however, it is said to have limitations of realistic power/energy density and energy efficiency [8]. This is caused by the mass limitation of the cell. The coin-cell can be either a standard configuration shown in Figure 2.2a or a dual OER and ORR cathode system sandwiching the zinc anode with perforated caps. The flow system is versatile and may be easily integrated with various energy technologies for cell construction or scaled up for larger applications such as energy storage and stationary power plants. It is regarded to be safe and has a long operational life due to the flow of the anolyte/electrolyte, which reduces side reactions. The flowing electrolyte enhances OH^- transport and lowers concentration gradients, while also eliminating precipitated carbonate and other by-products through external filters. With a circulating electrolyte solution, RZABs have a substantially longer cycle life and higher operating voltage than static electrolytes. The flow battery has a similar design to the parallel configuration and an electrolyte/anolyte bank that is positioned outside the cell to drive the flow (Figure 2.2b). While the anolyte circulation battery system includes an ion transport membrane [9]. The flow battery can also be constructed as a dual pumping system with independent electrolyte tanks for the anode and cathode. The flow battery design can reduce the energy efficiency of the battery as some of the energy is lost through circulation and any loss of pressure might affect the energy output. The presence of other components that might be needed to set up the flow system may

take up some of its volume and affect its volume density. With the growing demand for flexible wearable electronic gadgets, research into flexible batteries, particularly quasi-solid electrolytes, has set higher standards. The flexible battery in Figure 2.2c has similar components to other cells but uses a gel electrolyte prepared with polyvinyl alcohol (PVA), polyacrylic acid (PAA), gelatine, or graft copolymer gelling agents.

2.1.2. Types of metal-air battery storage designs

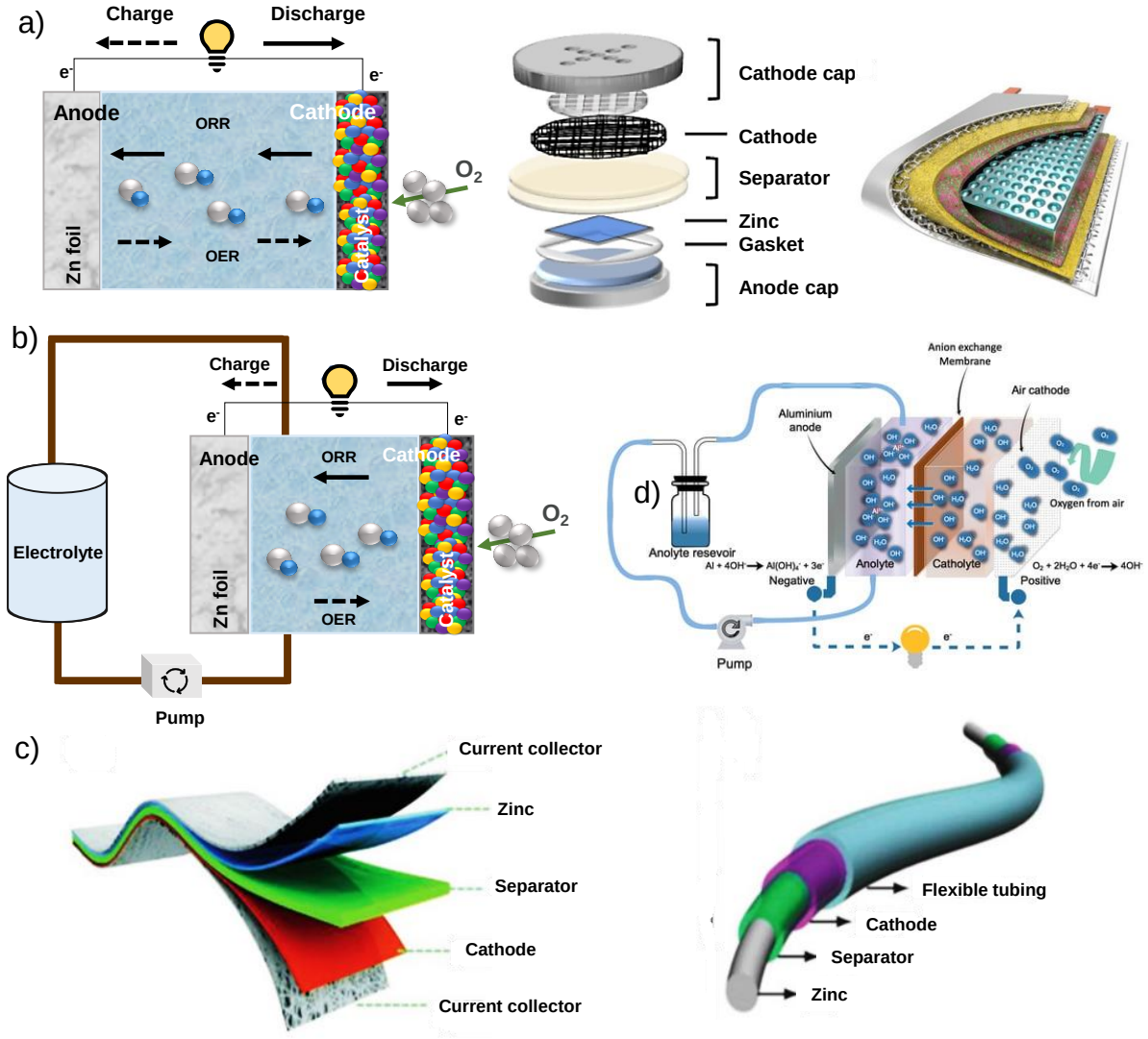

Figure 2.2: (a) Static (parallel plate, coin cell [10] and pouch cell), (b) flow circulation (electrolyte and anolyte circulation [9]) and (c) flexible [11] MAB configurations.

2.2. Zinc-air batteries

2.2.1. Working mechanism of zinc-air batteries

RZAB is made of four components, i) a porous air cathode (positive electrode: consisting of a catalyst and the gas diffusion layer), ii) a metallic zinc anode (negative electrode), iii) an electrolyte, and iv) a separator (Figure 2.3). The surface of the air electrode undergoes two oxygen reactions, oxygen reduction reaction (ORR) takes place when the battery discharges, and the oxygen evolution reaction (OER) during charging.

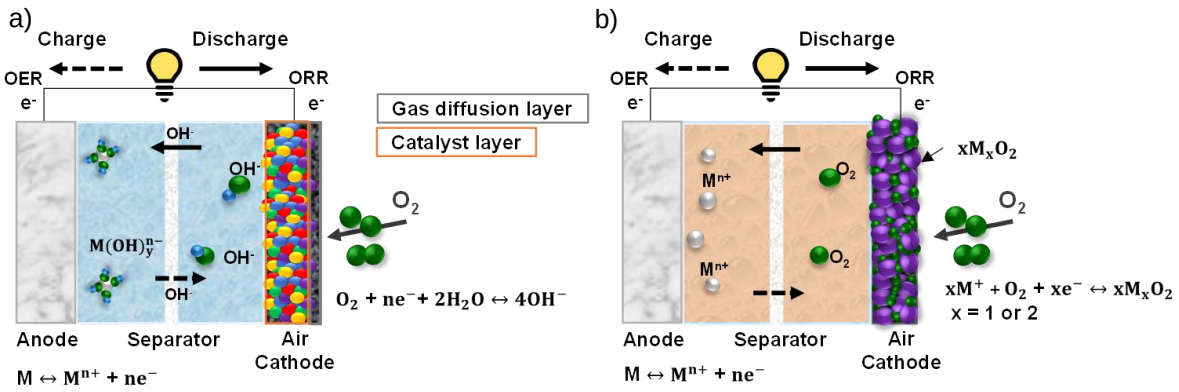

Figure 2.3: Schematic illustration of (a) aqueous and (b) non-aqueous ZABs during charge and discharge.

During discharge, the concentration gradient of oxygen gas from the environment causes it to infiltrate into the porous cathode material. The oxygen is then reduced at the triple phase boundary between the solid working electrode, liquid electrolyte, and gas phase. Hydroxide ions (OH^-) are then transported in the aqueous electrolyte from the air cathode to the metallic anode (i.e. oxygen evolution reaction). At the anode metallic zinc is oxidised and reacts with hydroxide ions to produce soluble zincate ions ($Zn(OH)_4^{2-}$) [12]. When these zincate ions are supersaturated in the electrolyte they undergo spontaneous decomposition to form insoluble zinc oxide (ZnO). Parallel to this, the parasitic hydrogen evolution reaction (HER) reaction takes place at the anode when water receives electrons and converts them to hydrogen gas (H_2) and hydroxide ions [13]. When hydrogen combines with the dissolved Zn, the self-corrosion of Zn can occur. Upon recharging the reaction processes are reversed by the reduction of zincate ions to zinc at the anode and oxygen is released at the cathode (i.e. oxygen

reduction reaction) [14]. The described reaction processes are summarised as follows [13,14]:

Discharge

Anode: $Zn + 4OH^- \rightarrow Zn(OH)_4^{2-} + 2e^-$ (E^0 = -1.25 V vs. SHE) (2.1)

$Zn(OH)_4^{2-} \rightarrow ZnO + H_2O + 2OH^-$ (2.2)

Cathode: $O_2 + 4e^- + 2H_2O \rightarrow 4OH^-$ (E^0 = +0.4 V vs. SHE) (2.3)

Overall reaction: $2Zn + O_2 \rightarrow 2ZnO$ ($E_{cell} = E^0_{cathode} - E^0_{anode}$ = +1.65 V) (2.4)

Parasitic reaction: $Zn + 2H_2O \rightarrow Zn(OH)_2 + H_2$ (2.5)

$Zn + 2OH^- + 2H_2O \rightarrow Zn(OH)_4^{2-} + H_2$

Charge

Anode: $ZnO + H_2O + 2OH^- \rightarrow Zn(OH)_4^{2-}$ (2.6)

$Zn(OH)_4^{2-} + 2e^- \rightarrow Zn + 4OH^-$ (2.7)

Cathode: $4OH^- \rightarrow O_2 + 2H_2O + 4e^-$ (2.8)

Overall reaction: $2ZnO \rightarrow 2Zn + O_2$ (2.9)

In a room-temperature ionic liquid (RTIL), a quasi-reversible oxygen reduction reaction occurs, and oxygen gains electrons and forms superoxide ($O_2^{\cdot -}$). The presence of the superoxide results in the blockage of electron transfer in aprotic RTIL [15]. On the other hand, superoxide is a strong nucleophile that can react with protons in protic RTIL to produce per-hydroxy radical ($HO_2^{\cdot}$) [15]. The radical further reacts with the superoxide to form peroxide (HO_2^-). The reaction processes are summarised in equation 2.10 to 2.15 [15,16].

ORR

$O_2 + e^- \rightarrow O_2^{\cdot -}$ (2.10)

$O_2^{\cdot -} + H^+ \rightarrow HO_2^{\cdot}$ (2.11)

$HO_2^{\cdot} + O_2^{\cdot -} \rightarrow HO_2^- + O_2$ (2.12)

$HO_2^{\cdot} + e^- \rightarrow HO_2^-$ (2.13)

$HO_2^- + H^+ \rightarrow H_2O_2$ (2.14)

OER

$$2H_2O \rightarrow O_2 + 4H^+ + 4e^- \quad (2.15)$$

2.2.2. Challenges of zinc-air batteries

The challenges associated with the RZABs have affected their commercialisation success. On the cathode, the charge (OER) and discharge (ORR) processes tend to be sluggish and have energy barriers [17]. This is because of the solid-solute-solid mechanism ($Zn\text{-}Zn(OH)_4^{2-}\text{-}ZnO$) of RZABs. ZAB's low practical working voltage (1.2 V) compared to its theoretical voltage (1.66 V) is reported to be due to the deviation of the charge and discharge potentials from the standard value as a result of the over-potential of the positive electrode causing low roundtrip efficiency [18]. This is caused by the catalysts' low tolerance for alternating reductive and oxidative conditions during discharge-charge cycles [7]. It is hard to avoid CO_2 in the air, and RZABs are sensitive to CO_2 in the feed gas stream [19]. CO_2 reacts with the electrolyte to form carbonate/bicarbonate anions (equation 2.16) which decrease the electrolyte conductivity and clog pores [19].

$$2KOH + CO_2 \rightarrow K_2CO_3 + H_2O \text{ and/or } KOH + CO_2 \rightarrow KHCO_3 \quad (2.16)$$

The presence of carbonate/bicarbonate anions causes the weakening of the ionic conductivity of the electrolyte. Another challenging issue with the use of air feedstock is moisture absorption from the environment, as well as electrolyte evaporation, which both contribute to the short life cycle of the battery. Water accumulation may cause air electrode flooding, impairing oxygen delivery to the catalyst's active sites [8]. Water loss increases the concentration of the electrolyte in the cell, which has a negative impact on the discharge response [8]. Furthermore, if the electrolyte is diluted, ionic conductivity decreases, resulting in increased internal resistance of the system [8]. The air hole also poses a problem of electrolyte leakage as well as evaporation.

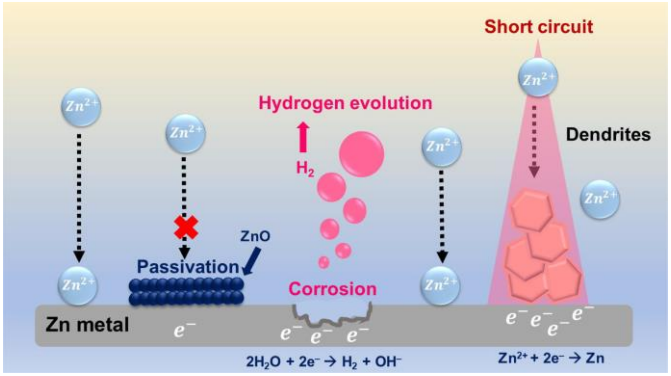

Figure 2.4: Challenges associated with zinc degradation [20].

Figure 2.4 shows the challenges associated with the zinc anode: H_2 evolution, metal corrosion, dendrite formation, and passivation. The reaction between Zn and the electrolyte has a spontaneous H_2 generation (equation 2.5), it is an undesired reaction because it brings about the self-corrosion of the Zn anode. Metal corrosion leads to capacity fade due to the loss of the active material. H_2 depletes the electrolyte, leading to drying, increased internal pressure, and blocked ionic pathways. This results in low Coulombic efficiency (60%) and zinc loss during charging and discharging [13,21]. The build-up of this gas can cause the battery to explode.

During charging, there is a tendency of some of the zincate ions to deposit onto different locations on the electrode surface causing uneven surface roughness and dendrite formations and change in morphology. This can cause the gradual degradation of the battery performance due to the loss of active sites. The gradual build-up of dendrite growth can penetrate the separator, causing decreased Coulombic efficiency and short circuits. Dendrite growth is the formation of tree-like structures. The battery also suffers from poor cyclability and stability due to the high solubility of zincate ions in the electrolyte. In a highly concentrated electrolyte, excess zincate ions are generated, leading to the high production of zinc oxide (ZnO). The build-up of excess ZnO later forms an insulating layer (or passivation layer) on the electrode surface. The passivation layer prevents further reaction of unreacted Zn, preventing efficient discharge of the battery, and results in low catalytic activity of the active content and poor rechargeability.

2.3. Electrochemical kinetics and characterisation

Electrochemical measurements are influenced by heterogeneous environments (i.e. electrode, electrolyte, and analyte). When an electrode is immersed in an electrolyte, a phase boundary forms between the solid electrode and the surrounding electrolyte. The difference in charge carriers between the two phases creates a barrier to charge transfer and charge can only pass this barrier when a molecule receives (reduced, R) or gives up (oxidised, O) an electron (e^-).

$$O + ne^- \leftrightarrows R \quad (2.17)$$

n is the number of electrons transferred.

2.3.1. Mass transport

Electrochemical systems involve charge transfer between the electrode and electrolyte interfaces. Mass transfer plays a very important role in these systems. Ionic mass transport takes place in three modes migration, convection, and diffusion. Migration is the movement of charged particles under the influence of an electric field. In the bulk electrolyte solution (away from the electrode), concentration gradients are often minor, and the total current is conveyed primarily by migration. Convection is the movement of ions due to the flux of the bulk electrolyte solution caused by external mechanical energy such as stirring or rotation. Diffusion is the movement of species from high to low concentration under the influence of a gradient of a chemical potential. Fick proposed that diffusion should take place wherever there is a concentration gradient in order to reduce the gradient [22]. After eliminating the concentration gradient, the flux ought to be zero [22]. The flux can be related to the concentration gradient using Fick's first law (equation 2.18) [22].

$$J = -D\frac{\partial C}{\partial y} \quad (2.18)$$

where J is the solution flux, C (mol/m^3) is the concentration, D (cm^2/s) is the diffusion coefficient, y (m) is the position parameter and ∂ is the partial derivative. However, because there is no time parameter, Fick's first law cannot be applied to determine the diffusion coefficient. Therefore, Fick's second law was derived from the mass conservation and Fick's first law (equation 2.19) [23].

$$\frac{\partial C}{\partial t} = D\frac{\partial^2 C}{\partial y^2} \quad (2.19)$$

2.3.2. Cyclic Voltammetry (CV)

Cyclic voltammetry (CV) is an extensively applied multipurpose electrochemical technique used to provide qualitative analysis of different electroactive materials. CV is a powerful tool for understanding the thermodynamics of redox processes, adsorption processes, coupled chemical and electrochemical reactions, and heterogeneous electron transfer reaction kinetics of electroactive materials [24]. CV is often the first experimental method used in electroanalytical studies due to its ability to quickly determine the redox potentials of electroactive species and evaluate the impact of the electrolyte on the process [25]. A cyclic voltammogram is generated by applying a linear potential sweep to the working electrode (WE) with respect to the reference electrode (RE). The electrochemical signal recorded reflects the process taking place at the interface between the WE and the electrolyte. When the electrochemical reaction taking place at the WE/electrolyte interface is at equilibrium, the Nernst equation can be used to describe the interaction. The Nernst equation is a strong tool for predicting how a system will react to a change in the concentration of species in an electrolyte or a change in the electrode potential [26]. The Nernst equation connects the potential of an electrochemical cell (E) to the standard potential of a species (E_o) and the relative activity of the oxidised (Ox) and reduced (Red) analytes in the system at equilibrium [26].

$$E = E_o + \frac{RT}{nF}\log\frac{(Ox)}{(Red)} = E + 2.3026\frac{RT}{nF}\log_{10}\frac{(Ox)}{(Red)} \quad (2.20)$$

where F is Faraday's constant, R is the universal gas constant, n is the number of electrons, and T is the temperature. When the voltage is scanned during the CV experiment, the concentration of the species in the electrolyte near the electrode varies with time, according to the Nernst equation [26]. If we take an example of the ferri-ferrocyanide reaction in Figure 2.5, when the potential is scanned cathodically observing the IUPAC conversion, the ferricyanide ($Fe(CN)_6^{3-}$) is steadily depleted near the electrode as it is reduced to ferrocyanide ($Fe(CN)_6^{4-}$). The diffusion of $Fe(CN)_6^{3-}$ from the bulk solution to the interface results in an observable peak cathodic current (j_{pc}). Throughout the scan, the volume of solution at the electrode's surface containing

$Fe(CN)_6^{4-}$, known as the diffusion layer, increases. This slows the mass transport of $Fe(CN)_6^{3-}$ to the electrode. As the scan progresses, the diffusion rate of $Fe(CN)_6^{3-}$ from the bulk solution to the electrode surface slows down, causing the current to drop. When the switching potential is achieved, the direction of the scan reverses and the potential is scanned in the anodic direction. While the concentration of $Fe(CN)_6^{3-}$ at the electrode surface decreases, the concentration of $Fe(CN)_6^{4-}$ increases, obeying the Nernst equation [26]. As the applied voltage increases, the $Fe(CN)_6^{4-}$ on the electrode surface oxidises back to $Fe(CN)_6^{3-}$. The halfway potential ($E = E_{1/2}$) between the two observed peaks gives an easy approach to estimate the E_o for a reversible electron transfer [26]. The analyte's diffusion to and from the electrode causes the two peaks to separate [26]. If the reduction process is reversible both chemically and electrochemically, the difference between the anodic and cathodic peak potentials (called peak-to-peak separation, ΔEp) is 57 mV at 25 °C (2.22 RT/F) [26]. The position and shape of the peaks can reveal important details about the nature of the electrochemical activity and the chemical species involved.

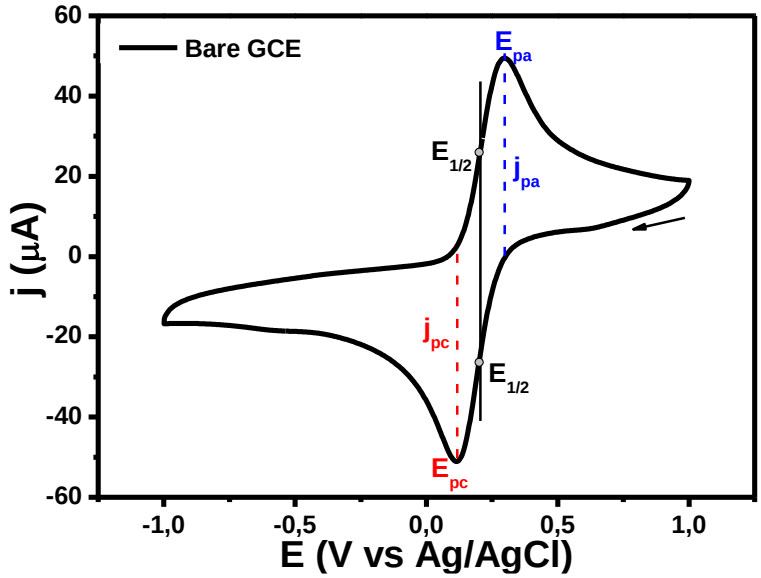

Figure 2.5: A typical cyclic voltammogram of a glassy carbon electrode (GCE) in 0.3 M ferri-ferrocyanide electrolyte.

2.3.3. Double layer capacitance

CV can be used to estimate the electric double-layer capacitance (EDLC) along the non-faradaic current region of the voltammogram. The capacitive charge can be

determined by varying the scan rate (ν) in a non-faradaic current region to evaluate the performance of a material. Adsorbed cations and anions intercalate/de-intercalate at the surface of the electrode and charge carriers (ions) build up at the electrode-electrolyte interface resulting in the formation of a capacitive current [27]. To balance the charge on the electrode and maintain charge neutrality, a capacitive double-layer forms where ions are packed as densely as possible to create a dense layer of ions close to the electrode [28]. The Gouy–Chapman-Stern-Grahame (GCSG) model can be used to model the double-layer region in Figure 2.6. The model is divided into three separate layers. The first layer is the inner Helmholtz plane (IHP) which is made up of adsorbed anions on the surface. The second layer is the outer Helmholtz plane (OHP) which is primarily made up of completely hydrated cations. The diffusion layer makes up the third layer which contains hydrated anions and cations.

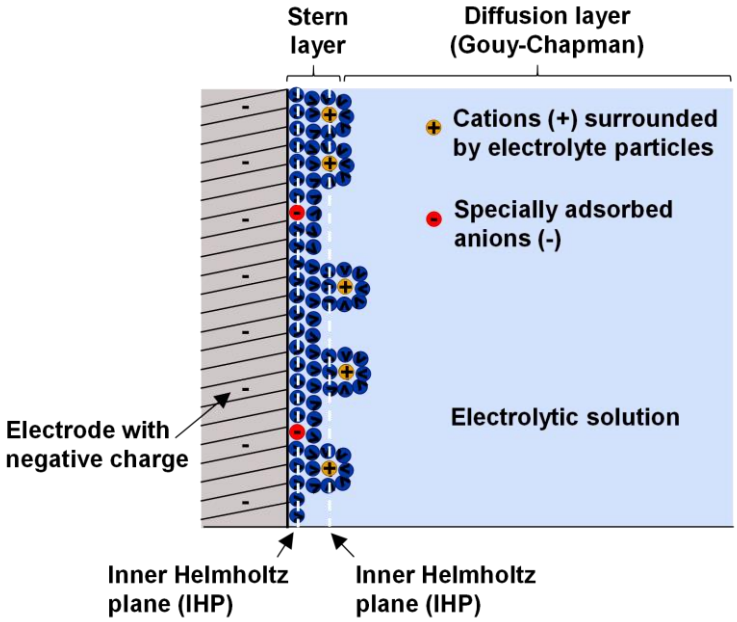

Figure 2.6: Schematic illustration of the electrical double-layer build-up at the electrode-electrolyte interface.

The anodic and cathodic capacitive current (j_c) is extracted from the middle of the potential window of a voltammogram. The j_c is plotted against the ν and the double layer capacitance (C_{DL}) extracted from the slope of the resulting curve. The CDL is then converted to electrochemically active surface area (ECSA, cm^2) using equation 2.21.

$$ECSA = C_{DL}/C_S \quad (2.21)$$

2.3.4. Linear scan voltammetry (LSV)

The rate of electron transport between the electrode and electrolyte interface can be understood and used to evaluate the kinetics and mass transfer effects by performing Linear sweep voltammetry (LSV). LSV applies the potential for an anodic (reverse, i.e., upper limit to lower limit) and a cathodic (forward, i.e., lower limit to upper limit) sweep, respectively, to investigate the redox (oxidation/reduction) behaviour of an electroactive species [24]. The potential applied changes linearly with time (Figure 2.7a), parallel to the experiment, current is recorded and the current-potential voltammogram results in a typical shape seen in Figure 2.7b. The LSV profiles are obtained using a rotating disk electrode (RDE) and a rotating ring disk electrode (RRDE). RDE is used to study oxygen reduction reactions (ORR) at different electrode rotation speeds, oxygen evolution reaction (OER), and hydrogen evolution reaction (HER) kinetics at a fixed scan rate. Bhuvanendran et al. [24] report three main influencing factors in determining ORR and OER: (i) the electron transfer rate, (ii) the reactivity of electroactive species, and (iii) the potential scan rate. LSV profile can be used to extract the limiting current density and kinetic current density and to determine the kinetics of ORR. The Koutecky-Levich equation can be used to determine the mass-transfer effect over the electrode surface.

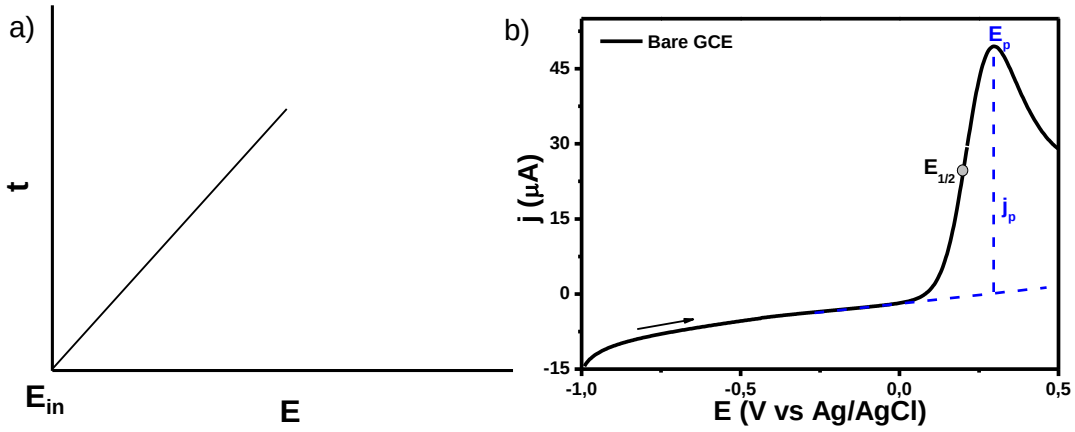

Figure 2.7: Linear sweep voltammograms showing the (a) linear change of the applied potential with time and (b) current-potential curve showing peak potential (E_p) and the peak current (j_p).

2.3.5. Rotating disk electrode (RDE)

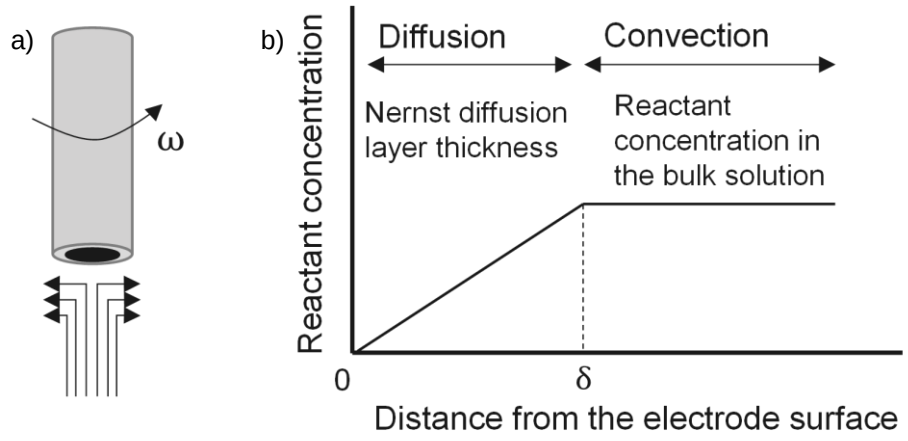

Figure 2.8: (a) Electrolyte movement caused by the rotation of RDE and (b) the Nernst diffusion layer model.

The rotating disk electrode voltammetry (RDE) is a well-established hydrodynamic-transport-based voltammetric approach that produces a perfectly defined solution movement by controlled mass transport. A RDE is an electrode (such as platinum or glassy carbon) embedded in an insulator (such as glass, Teflon, or Kel-F) and rotated perpendicular to the surface of the disc electrode centre at a known frequency (ω), Figure 2.8a. According to the Nernst diffusion layer model (Figure 2.8b), diffusion is the only transport mechanism near the electrode surface and strong convection dominates away from the electrode surface [29]. RDE employs forced convection to improve the mass transport of electroactive species toward the electrode surface, resulting in increased sensitivity and quicker rate constants [30]. The RDE is a versatile technique widely used to study various aspects of electrode processes at solid electrodes. Besides having a simple setup, the RDE has several advantages [31]: (i) it creates a diffusion layer whose thickness is constant over time; (ii) double-layer charging has little impact on the measurement; and (iii) it solves the theoretical basis of the mass transfer process, providing equations that link the experimental parameters to the mass transfer of reactants to the electrode surface. The Levich equation can be used to derive the limiting current equation for a mass-transfer controlled process at the RDE [31].

$$j_L = 0.620\, nFAC_{O_2} D^{2/3} \gamma^{-1/6} \omega^{1/2} \qquad (2.22)$$

j_L is the diffusion limiting current (A), n is the number of electrons transferred (mol^{-1}), A is the area of the electrode (cm^2), C_{O_2} is the oxygen solution concentration (1.15 x 10^{-3} mol/dm^3), D is the diffusion coefficient (1.95 x 10^{-5} cm^2/s), γ is the kinematic viscosity (8.98 x 10^{-3} cm^2/s), ω is the rotation speed (rad/s) and F is the Faraday constant (96 485 C/mol). The diffusion layer thickness can be expressed by $\delta = 1.61 D^{1/3}\nu^{1/16}\omega^{-1/2}$ [31]. The plot of j_L increases linearly with $\omega^{1/2}$. Figure 2.9 shows the half-cell reaction equations of ORR and OER and a typical steady-state polarisation curve for an individual catalyst using a RDE. OER generally obeys the Butler-Volmer model even with very high overpotentials, but the current density of ORR approaches a constant value at high overpotentials because of the limitation in the mass transfer rate [32].

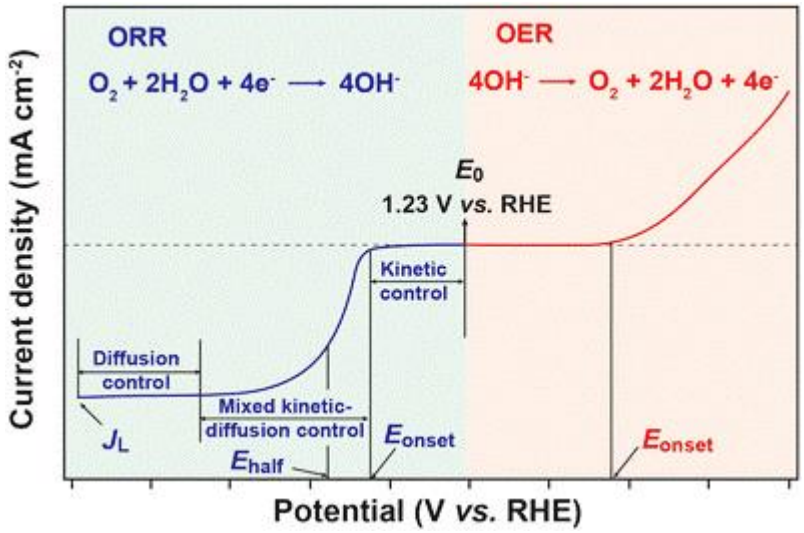

Figure 2.9: ORR and OER polarisation curves [33].

The RDE can be effectively used to measure the electrocatalytic activity of electrocatalysts during oxygen reactions. The polarisation curve can be used to determine various reaction index parameters such as the onset potential (E_{onset}), half-wave potential ($E_{1/2}$), overpotential (under a given current density (η_j)) commonly at 10 mA/cm^2, and diffusion-limiting current density (j_L/j_d). The limiting current is obtained when the potential of the RDE is set to the plateau of the matching current-potential curve for the reactant. The E_{onset} is proposed to be at a potential value of 5% of j_L/j_d or 0.1 mA/cm^2 [34]. The OER overpotential (η) is calculated as the difference between equilibrium potential (E_{eq}) and potential at a current density of 10 mA/cm^2. The change in potential (ΔE) or bifunctionality index (BI) is calculated as the difference between η_j

and $E_{1/2}$. The smaller the difference the more effective the materials are in catalysing both reactions. In general, the large overpotential of OER affects the overall efficiency of oxygen reaction processes [33]. The E_{onset} and η_j are commonly used to estimate the complexity of an oxygen process [33]. The half-wave potential ($E_{1/2}$) of ORR is the potential at which the current density equals half of the diffusion-limiting current density (j_L/j_d) [33]. A more positive $E_{1/2}$ value indicates a more effective electrocatalyst.

A deviation of the Levich plot from linearity suggests a kinetic limitation involved in the electron-transfer reaction. The Koutecky-Levich (K-L) equation is used to measure the kinetic current density (j_k) and the number of transferred electrons (n) by evaluating the mass transport kinetics at different rotation speeds (ω) and diffusion-controlled processes. The K–L equation is given below [35]:

$$\frac{1}{j} = \frac{1}{j_d} + \frac{1}{j_k} = \frac{1}{0.21nFD^{2/3}\gamma^{-1/6}Co_2\omega^{½}} + \frac{1}{nFkCo_2} \quad (2.23)$$

where

$$j_K = nFkC_{O_2} \quad (2.24)$$

$$j_K = \frac{j \times j_L}{j - j_L} \quad (2.25)$$

j is the measured current density at a given potential, j_k is the kinetic current (A) and k is the electron transfer rate constant (cm/s).

When a flat and smooth electrode is used, the total area exposed to the electrolyte is equivalent to the geometric area. However, in porous materials, such as carbon-based electrocatalysts, the area that can interact with dioxygen molecules (including inner porosity) is substantially larger than the geometric area, which is not accounted for by the K-L equations [36]. Furthermore, such microporosity can extend the retention duration of ORR by-products, resulting in a second reduction process of O_2 and H_2O_2 within the porous structure of the carbon material [37]. RRDE has been used to characterise porous carbon materials for electrochemical processes [36,37]. In the work by Gabe et al. [37] a carbon material with a surface area of less than 300 m^2/g showed a similar number of electrons in the RRDE experiment to the K-L theory. Bouleau et al. [36] discovered that the RRDE experiment is highly necessary when the

specific surface area of the porous carbon is larger in order to obtain an accurate number of electrons transferred.

2.3.6. Linear Polarisation resistance (LPR)

Linear polarisation resistance (LPR) is an electrochemical method used to measure real-time corrosion current density (i_{corr}) and corrosion rate (C_R). The corrosion current density in corrosion studies is commonly represented with i instead of j. LPR is used to monitor the relationship between potential and current generated. The technique is mostly effective in aqueous electrolytes and it has been used in water-based corrosion environments. Major advantages of LPR monitoring include; (i) Changes in corrosion rate can typically be detected within minutes, providing a near-instantaneous measurement system. (ii) It can be used to provide a qualitative measure of pitting behaviour, whether the pitting tendency is shallow and rare, or deep and profuse. (iii) LPR monitoring can also monitor a metal's behaviour under different conditions. This method can be used to evaluate the performance of the anode materials towards corrosion resistance. To evaluate the corrosion parameters, the plot of the logarithm of current density (Log i) to potential can be obtained. The intercept of the extrapolation of the anodic and cathodic contributions is used to determine i_{corr} and corrosion potential (E_{corr}). The slope of the linear component of the polarisation curve of the Butler-Volmer equation current-potential curve can be used to extract the polarisation resistance (R_p). Stern and Geary [38] were the first to present the link between R_p and corrosion i_{corr} using equation 2.26.

$$R_p = \frac{B}{i_{corr}} \tag{2.26}$$

where B is an electrochemical constant (mV) theoretically calculated using the following equation:

$$B = \frac{\beta_a \times \beta_c}{2.3 \times (\beta_a + \beta_a)} \tag{2.27}$$

β_a and β_c are the anodic and cathodic slopes of a Tafel plot, respectively. The corrosion rate can be calculate using i_{corr}, where

$$C_R = K \frac{i_{corr} \times EW}{\rho} \tag{2.28}$$

C_R is the corrosion rate (mils per year), K is the conversion constant, EW is the equivalent weight of the corroding metal (g) and ρ is the density of the corroding metal (g/cm^3). Corrosion potential (E_{corr}) is the potential at which anodic and cathodic reactions are of equal rate. The E_{corr} is not equivalent to the equilibrium potential because the potential measured is between a corroding electrode and a reference electrode in an electrolyte [39]. E_{corr} represents the mixed potential at which the anodic (oxidation of the metal) and cathodic (reduction of species in the electrolyte) reactions simultaneously occur.

2.3.7. Tafel analysis

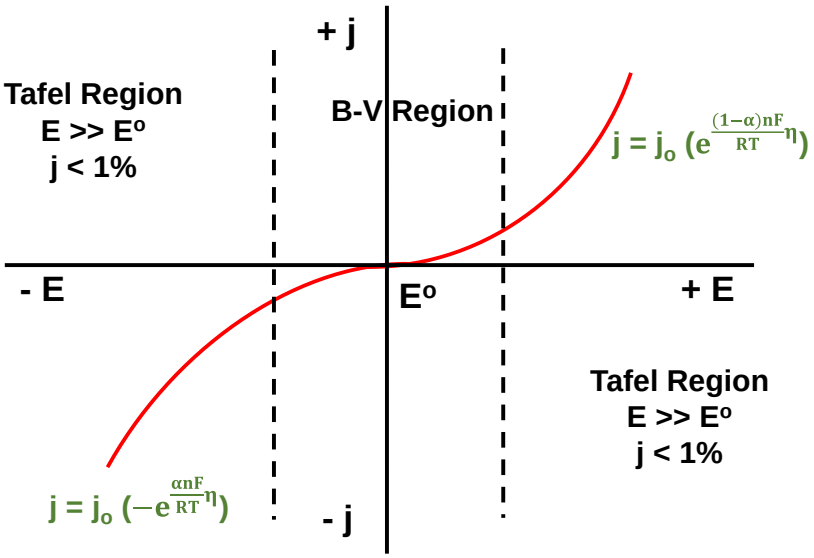

Figure 2.10: The current-potential relationship at B-V and Tafel regions.

Tafel analysis provides valuable information on the kinetics and fundamental parameters in electrochemical systems such as exchange current density, charge transfer resistances, electrode mechanism (i.e. Volmer, Heyrovsky, Tafel), or rate determining-step. The Volmer-Tafel and Volmer-Heyrovský pathways are the mechanisms that are responsible for the hydrogen oxidation and evolution reactions. The Tafel equation is a linearised form of the Butler-Volmer expression (Figure 2.10). The Butler-Volmer equation is commonly used in electrochemical theory to describe the relationship between electrode potential and current density. Equation 2.29 can be used to extract these parameters.

$$i = i_0 \left[\exp^{\frac{\alpha nF}{RT}\eta} - \exp^{\frac{-(1-\alpha)nF}{RT}\eta} \right] \quad (2.29)$$

where j is the current density, j_o is the exchange current density, α is the charge transfer coefficient ($0 < \alpha < 1$), n is the number of electrons transferred, F is the Faraday constant, R is the gas constant, T is the temperature in K and η is the difference between the electrode potential (E) and standard potential (E^0) or the overpotential. Tafel analysis involves the use of linear sweep voltammetry at comparatively lower scan rates, converting the j versus E into a plot of log(j) versus η. For large values of η

$$\eta = \frac{RT}{\alpha nF} \ln i_o - \frac{RT}{\alpha nF} \ln i \qquad (2.30)$$

The Tafel slope (b) is obtained by fitting the linear section of the curve to the Tafel equation. Tafel equation is empirically formulated to

$$\eta = a + b \log(i) \qquad (2.31)$$

where a is the Tafel slope. The empirical Tafel constants can be identified as

$$b_1 = \frac{2.3RT}{\alpha F} \log(i_o) \qquad b_2 = \frac{-2.3RT}{\alpha F} \log(i) \qquad (2.32)$$

As observed in Figure 2.11, the plot consists of an anodic [(1 - α)F/2.3RT] and cathodic slopes [(-αF/2.3RT]. An intercept of log i_o can be obtained by extrapolating the plot's linear section. As η gets closer to zero, the anodic and cathodic curves start to diverge significantly from the linear behaviour. At high overpotentials, the mass transfer limitation causes a negative deviation from linearity [40].

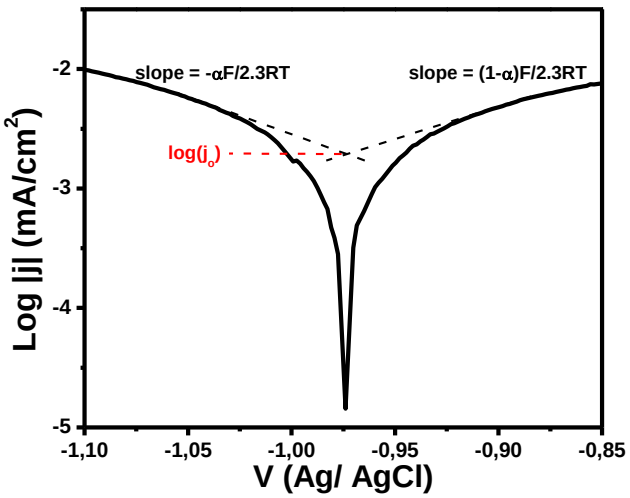

Figure 2.11: Tafel plot representing the anodic and cathodic branches of the current-overpotential curve.

Small changes in the activation energy can significantly impact how quickly the reaction occurs, reflected by the Tafel slope. Additionally, the Tafel slope can also be influenced by the α value, which describes the energy barrier for a redox reaction. When α = 0.5, the resulting Tafel slope is 120 mV for a one-electron process [41].

In corrosion studies the Butler-Volmer is generally applied in an empirical form [42]:

$$i = i_{corr}\left[\left(\exp\left(\frac{\eta}{b_a}\right) - \exp\left(\frac{-\eta}{b_c}\right)\right]\right. \quad (2.33)$$

where b_a and b_c are the anodic and cathodic Tafel slopes, i_{corr} is the corrosion current and η is the polarisation. η is defined as the difference between electrode potential and corrosion potential [42]. Equation 2.33 can be linearised in two ways; (i) If $\eta \gg b_a$ or $\eta \ll b_c$ and, consequently, one of the exponential terms is negligible compared to the other one, then the equation is transformed into the linear anodic and cathodic Tafel equations, respectively [42]:

$$\ln i = \ln i_{corr} + \frac{\eta}{b_a} \quad (2.34)$$

$$\ln i = \ln i_{corr} + \frac{-\eta}{b_c} \quad (2.35)$$

(ii) Polarisation resistance (R_p) is determined by expanding the exponential terms and omitting the second- and higher-order elements.

$$\frac{1}{R_p} = \frac{dj}{d\eta}\Big|_{\eta=0} = i_{corr}\left(\frac{1}{b_a} + \frac{1}{b_a}\right) \quad (2.36)$$

Note: The sign of b_a and b_c are equal.

2.3.8. Electrochemical impedance spectroscopy (EIS)

EIS is a commonly used analytical approach for studying electrochemical systems by applying a small alternating current (AC) voltage signal as a function of the frequency of the amplitude signal [43]. EIS is a non-destructive and powerful approach that provides information about a material's passive components (resistances, capacitors, or constant phase elements) connected in parallel or in series using a suitable equivalent circuit model. EIS is widely used in many fields such as corrosion studies, semiconductors, energy conversion and storage technologies, chemical sensing and

biosensing, non-invasive diagnostics, etc [44]. To measure the impedance response, a small excitation potential ($E_{1/2}$ or open circuit potential) is applied. The electrochemical cell response is pseudo-linear, resulting in a phase shift, but the current response to a sinusoidal potential is sinusoidal at the frequency applied (0.1 Hz - 1 MHz). Lazanas and Prodromidis [44] report the perturbation to be governed by three processes: (i) charging and discharging of the electric double layer at the electrode-electrolyte interface, (ii) the kinetics of the faradaic reaction and (iii) the diffusion of redox species from the bulk solution to the electrode surface. The impedance of an electrical circuit significantly depends on the type and configuration of passive elements present. The generated excitation signal is presented as a function of time (equation 2.37).

$$E(t) = E_o \sin(\omega t) \tag{2.37}$$

where E_t is the potential at time t, E_o is the amplitude of the signal, ω is the radial frequency (radians/second). If two periodic waves with the same magnitude exist ($E_o = J_o$) the instantaneous values will be different because of the constant time shift between the two waves at a certain angle (also known as the phase-angle shift (φ)) as seen in Figure 2.12a. Assuming one of the signals as a reference results in equation 2.38.

$$j(t) = J_o \sin(\omega t - \varphi) \tag{2.38}$$

The impedance of the circuit at this frequency $Z(\omega)$ is defined as

$$Z(\omega) = |Z|e^{j\varphi} = |Z|(\cos\varphi + j\sin\varphi) = Z' + JZ'' \tag{2.39}$$

Z' is the real part representing resistance on the x-axis, Z'' is the imaginary part representing reactance on the y-axis, |Z| is the module of impedance, and $\varphi = \omega t$ which is the phase shift. EIS measurements are often analysed using a correlation between impedance data and an equivalent circuit reflecting the physical processes occurring in the system under study. The graphical representation of $Z(\omega) = Z' + JZ''$ known as the Nyquist diagram and its corresponding circuit are represented in Figure 2.12b and 2.12c. For a given electrochemical process, several Nyquist curves could be produced, such as single-, two-, or half-semicircles [43]. The key components of the Nyquist diagram are solution resistance (R_s), charge transfer resistance (R_{ct}) which is responsible for the electron transfer and kinetics of the heterogeneous electrochemical

process, double layer capacitance (C_{dl}) and Warburg impedance (W) expresses the mass transport limitation of the redox species imposed by diffusion. The perfect capacitor does not regularly exist in experiments, hence an additional element known as a constant phase element (CPE) is used to mimic this non-ideal capacitance behaviour.

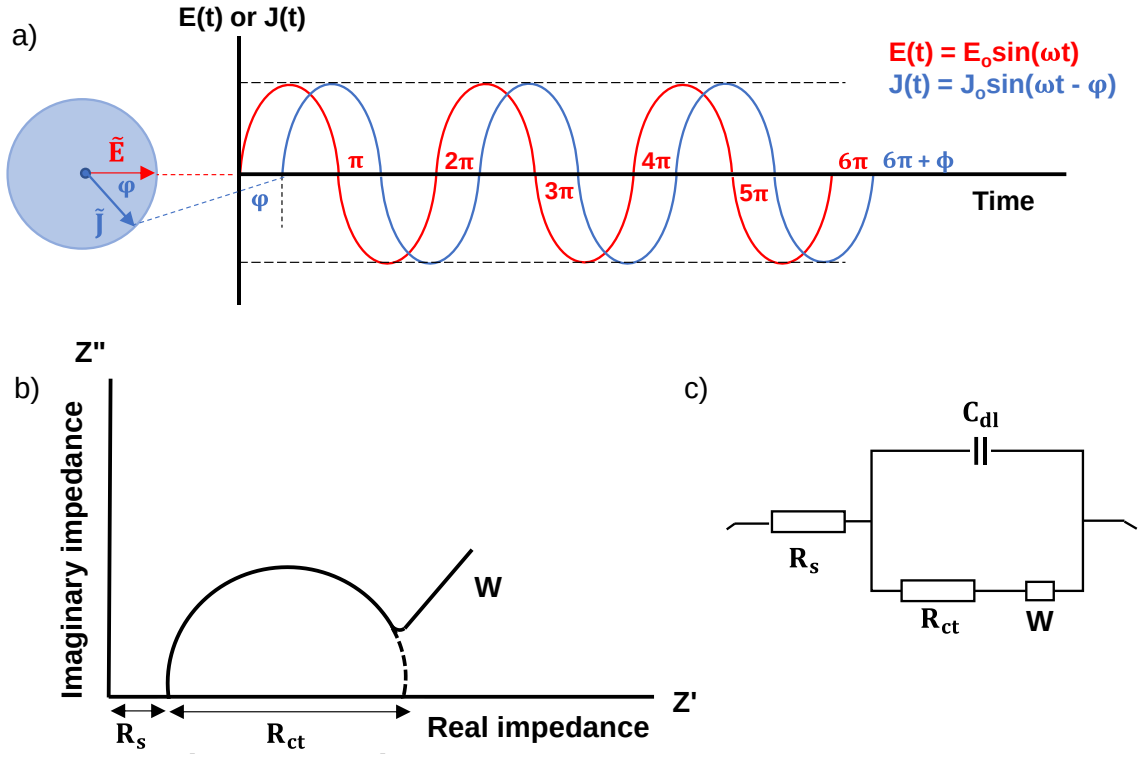

Figure 2.12: (a) Sinusoidal waveform response in a linear system showing phase shift, (b) Nyquist diagram and (c) its equivalent circuit.

2.3.9. Depth of discharge (DOD) of zinc-air battery

Depth-of-discharge is a percentage of how much a battery's capacity has been utilised in a single discharge cycle relative to its total capacity. The theoretical specific capacity (C_T) of a zinc electrode is 819.73 mAh/g_{Zn}, calculated from equation 2.40 [45].

$$C_T = \frac{nF}{3.6 \times M.W} \tag{2.40}$$

where n is the number of electrons (n = 2 for Zn in relation to equation 2.1), F is the Faraday's constant (96,485 C/mol), and M.W. is the molecular weight in g/mol. The factor of 3.6 is used to convert the theoretical specific capacity from C/g to mAh/g. The DOD for RZAB is calculated using performance metrics defined by Parker et al. [45].

The DOD calculation considers the total capacity per discharge of the air cathode and the theoretical capacity of the anode;

$$c_{Zn\text{-}air} = i \times t = A \times j \times t \quad (2.41)$$

$$c_{Zn} = m_{Zn} \times 819.73 = V_{Zn} \times \rho_{Zn} \times 819.73 \quad (2.42)$$

$$DOD_{Zn} = \frac{c_{Zn-air}}{c_{Zn}} = \frac{A \times j \times t}{V_{zn} \times \rho_{Zn} \times 819.73} = \frac{A \times j \times t}{V_{zn} \times \rho_{Zn} \times h_Z \times 819.73} \quad (2.43)$$

where A (cm^2) is the area of the air cathode, j (mA/cm^2) is the current density, t (h) is the individual discharge time, V_{Zn} (cm^3) is the volume of the Zn electrode, ρ_{Zn} is the bulk Zn density (7.14 g/cm^3) and h_{Zn} (cm) is the height of the Zn. Since the active cathode material (O_2 from the air) is not stored in the battery, the mass of the Zn anode determines the battery's total discharge capacity [45]. To optimise the specific energy and energy density of a compact two-electrode device, the Zn electrode (A_{Zn}) should have the same geometric area as the air cathode ($A_{cathode}$) [45]. To satisfy the technologically relevant barrier of 100 Wh/kg, a RZAB must have a DOD_{Zn} of at least 0.20 [45]. To compete in a Zn-air cell, the air cathode must meet this basic technical requirement.

2.4. Cathode

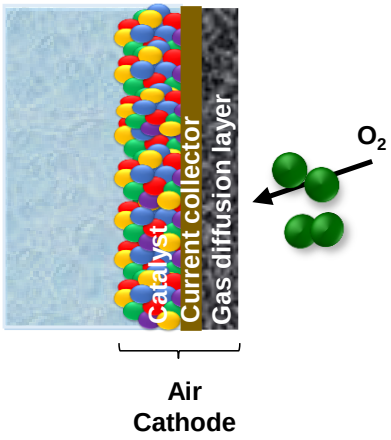

Figure 2.13: Air cathode components.

The air cathode shown in Figure 2.13 is made up of a gas diffusion layer (GDL), a catalyst, and a current collector. The gas diffusion layer allows oxygen to pass through from the atmosphere to the catalyst layer. Ideally, the GDL should be hydrophobic, porous, and lightweight [8]. These characteristics assist in preventing electrolyte

leakage and evaporation and preventing the adsorption of moisture. The current collector is used to connect the external electrical circuits and transfer electrons from the cathode to the anode. The current collectors that are used are either metallic (nickel (Ni) mesh, copper (Cu), and stainless steel) or non-metallic (carbon cloth, conductive carbon paper, and graphitic fibre) [8]. The catalyst is used to improve the oxygen reactions and kinetically reduce their overpotentials. The air cathode's design should be in a way that prevents electrolyte leakage from the air hole, has enhanced OER and ORR activities, prevents the migration of CO_2, and prevents electrode flooding and electrolyte evaporation.

2.4.1. OER and ORR mechanisms

When a RZAB is discharged, oxygen diffuses from the air to the catalyst while on the anode the metal is oxidised. Electrons are then transported from the anode through the external circuit to the cathode to break the O-O bonds and metal hydroxide is formed on the catalyst's surface. During discharge, O-H bonds are broken, and new O-O bonds are formed. However, due to the strong binding energy between O and H, the reaction kinetics of OER is quite sluggish, causing a high onset potential. The OER mechanism in alkaline media presents a four-electron pathway ($4OH^- \rightarrow O_2 + 2H_2O + 4e^-$).

$$* + H_2O \rightarrow *OH + H^+ + e^- \quad (2.44)$$

$$*OH \rightarrow *O + H^+ + e^- \quad (2.45)$$

$$*O + H_2O \rightarrow OOH* + H^+ + e^- \quad (2.46)$$

$$*OOH \rightarrow *O_2 + H^+ + e^- \quad (2.47)$$

$$*O_2 \rightarrow * + O_2 \quad (2.48)$$

where * represents the active site of the electrocatalyst, and *OOH, *OH, and *O indicate adsorbed intermediate species [32]. The ORR in alkaline media could occur by a two-electron ($O_2 + 2H_2O + 2e^- \rightarrow HO_2^- + 4OH^-$) or four-electron ($O_2 + 2H_2O + 4e^- \rightarrow 4OH^-$) pathway. The four-electron pathway is a highly favoured reaction because it is more efficient, while the two-electron pathway produces hydrogen peroxide (H_2O_2). The four-electron pathway has possible mechanisms being associative and dissociative [32].

Dissociative mechanism:

$O_2 + 2* \rightarrow 2O*$ (2.49)

$2O* + 2e^- + 2H_2O \rightarrow 2OH* + 2OH^-$ (2.50)

$2OH* + 2e \rightarrow 2OH^- + 2*$ (2.51)

This mechanism is the initial O_2 adsorption, followed by O-O bond breakage and formation of two adsorbed atomic O* species [32]. These species further gain two electrons and two protons to directly form OH^- without OOH^- generation [32]. This method can be classified as a direct $4e^-$ pathway [32]. Alternatively, ORR can also proceed according to the following associative mechanism [32]:

Four-electron pathway:

$O_2 + * \rightarrow O_2*$ (2.52)

$O_2* + H_2O + e^- \rightarrow OOH* + OH^-$ (2.53)

$OOH* + e^- \rightarrow O* + OH^-$ (2.54)

$O* + H_2O + e^- \rightarrow OH* + OH^-$ (2.55)

$OH* + e^- \rightarrow OH^- + *$ (2.56)

or the two-electron pathway:

$O_2 + * \rightarrow O_2*$ (2.57)

$O_2* + H_2O + e^- \rightarrow OOH* + OH^-$ (2.58)

$OOH* + e^- \rightarrow OOH^- + *$ (2.59)

The stability of the O* and OOH* intermediates obtained after the adsorption of O_2 on the surface of the electrocatalysts defines the dominant pathway [46]. The electron pathway on most carbon-based materials is less than four, while metal surfaces often follow a dissociative pathway due to the high adsorption of O_2 [32].

2.4.2. Catalysts for OER and ORR

Volcano plot offers insight into the best catalyst materials for specific applications [47]. It gives information about the rate of the cathode reaction and the oxygen adsorption energy. For ORR, the free energies of all the intermediates are calculated on a variety of close-packed metal surfaces, and a volcano plot (see Figure 2.14a) was constructed

relating their theoretical activity and ΔE_o, with platinum (Pt) near the top [47]. Metals that tightly bind oxygen experience reduced activity due to proton-electron transfer to O* or OH* [48]. Metals that bind oxygen poorly may have limited activity due to proton-electron transfer to O_2* (associative mechanism) or breaking of the O-O bond in O_2 (dissociative mechanism), depending on the applied potential [48]. Pt is known to be the best metal to effectively catalyse the ORR reaction. However, the rarity and expensive cost of Pt limits its broad technological utilisation. Three approaches have been investigated to reduce Pt costs for the ORR [49]: (i) reduction of Pt-loading, (ii) synthesis of non-noble metal catalysts, and (iii) synthesis of metal-free catalysts. To commercialise RZABs, a long-term strategy is to employ the second and third methods for developing ORR electrocatalysts. On the other hand, the OER volcano plot (Figure 2.14b) was created using ΔG_O - ΔG_{OH} descriptor for different metal oxides (rutile, perovskite, spinel, rock salt, and bixbyite) [47]. IrO_x was determined to be a great material for OER.

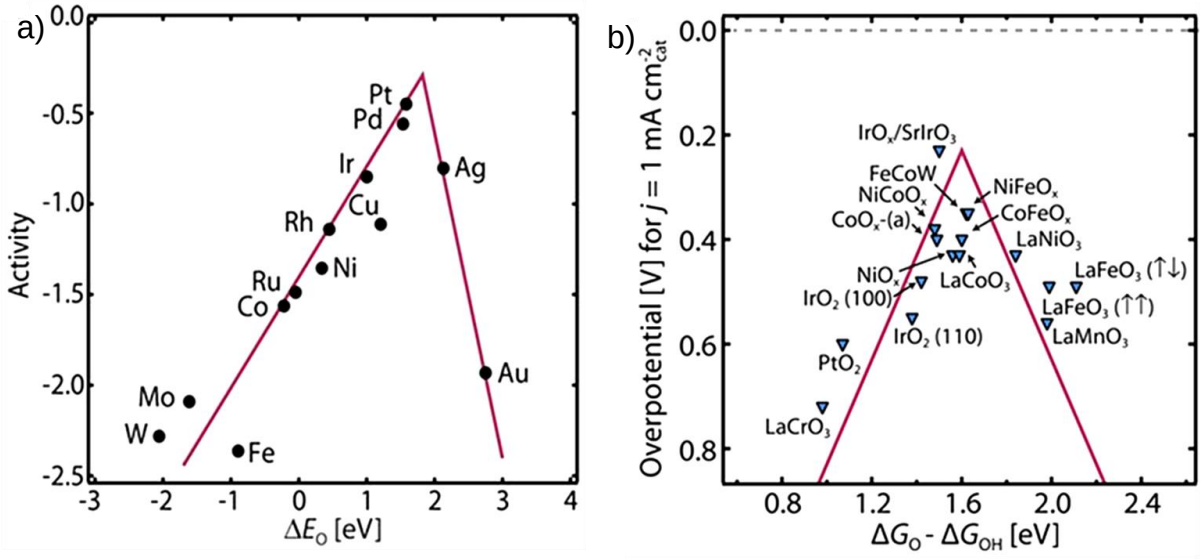

Figure 2.14: (a) ORR volcano plots for metals catalysts and (b) OER volcano plots for metal oxides [47]

Taking into consideration the cost of raw materials, the synthesis approaches suggested and the reactivity of metals and metal oxides for ORR and ORR, a relevant catalyst would be a non-noble bifunctional catalyst. The catalyst needs to be porous to allow for easy access of oxygen species to its active site to efficiently reduce oxygen to OH^- during discharge and back to oxygen during charging. The catalyst should also

possess the following characteristics: effective oxidising agent, stability in alkaline electrolytes, high capacity, and excellent cyclability. Having an electrocatalyst that facilitates both OER and ORR can promote faster reaction kinetics and fast charge and discharge capacity, resulting in higher power output and energy density, and extended battery lifespan by providing sustainable energy storage [50].

2.4.3. Cobalt as a bifunctional electrocatalyst

A wide range of transitional metals including cobalt, manganese, nickel, copper, and iron, have been extensively studied as bifunctional catalysts in OER and ORR. Amongst the investigated non-precious metal catalysts, cobalt has gained a lot of attention in RZAB applications. It has been demonstrated that defects can serve as electrocatalytic active sites, and in theory, more defects would result in more catalytic activity. The defects can be introduced through thermal treatment, cation/anion doping, plasma treatment, reduction processing, and acid/base treatment. A heterostructure of $Co_3O_4/Co(OH)_2$ on quantum dots was developed by Leng et al. [51]. In a three-electrode configuration, the electrocatalyst showed enhanced OER activity with an overpotential of 300 mV and $E_{1/2}$ of 844 mV. The catalyst had a high electroactive surface area compared to the other studied materials due to the presence of high oxygen defect regions (high Co^{2+} species). The bifunctionality of the catalyst was further tested in a RZAB. At 5 mA/cm^2 the cell showed good operating stability of 70 h with a potential gap of ca. 0.9 V and discharge voltage of ca. 1.1 V. Its solid-state battery demonstrated a good degree of flexibility with very little loss in the battery performance.

High active sites in a carbon-based electrocatalyst are not enough to guarantee the optimal performance of the catalyst. The porosity of the carbon support directly affects how easily reactant molecules can reach the active sites within the catalyst. Porosity offers more pathways for reactant molecules to travel through, reaching the active sites faster and in greater quantities. This improves the overall efficiency of the catalyst. This concept was proven through the preparation of N-doped cobalt-based bifunctional single atom catalyst (SAC) on porous carbon networks as alternative air cathodes due to the efficient use of cobalt atoms [52]. Co SACs anchored on a porous nitrogen-doped carbon framework (Co-N-C SACs) was prepared by sol-gel method

using glucose/SiO_2 xerogels and after pyrolysis the material was etched with hydrofluoric acid solution to remove silica and Co particles. The catalyst (Co-N-C SACs) was reported to possess micro and mesopores, which were responsible for hosting active sites and providing pathways for reactant and product molecules. Co-N-C SAC had an $E_{1/2}$ value of 0.851 V demonstrating that it was a promising catalyst for ORR application. The Co-N-C SACs exhibited promising OER activity with a moderate overpotential and favourable kinetics, suggesting its potential for bifunctional applications in RZAB with a discharge-charge gap of 0.78 V maintained over 54 cycles.

Cobalt-based metal-organic frameworks (Co-MOFs) are also being researched for their potential as electrode materials, but they often face challenges in achieving satisfactory electrochemical performances, particularly for long-term applications. Metal-organic frameworks (MOFs) are a novel type of porous material made by combining organic linkers and metal ions/clusters to create inorganic-organic hybrid porous materials. MOF-derived materials are effective bifunctional catalysts due to their tuneable surface area and abundant metal ions or clusters. However, during carbonisation, the carbon framework can self-aggregate and clog the pore structures, affecting the electrolyte-pore interaction [50], and the carbon-based materials derived from MOFs generally have poor conductivity. In the work by Xi et al. [53] carbon black was used to improve the dispersity and conductivity of MOF-Co (Co-CoO-Co_3O_4/NC) and achieved increased surface Co^{III}/Co^{II} ratios for OER and ORR. The resulting composite showed a highly improved oxygen response compared to the other materials under study. In the case of RZAB, the material showed a good discharge plateau (1.22 V) and only showed an irregular shape of the pulse cycling curve at around 420 cycles (140 h). This response was assumed to be due to severe carbon corrosion or electrocatalyst deterioration.

Zhou et al. [54] studied a 3D star-like MOF prepared by combining carbon-doped ZIF-L and ZIF-8 which was used as a precursor to produce the cobalt single-atom catalysts (Co SACs) supported on nitrogen-doped carbon frameworks (N-C). The carbon framework had micropores that hosted the Co-Nx active sites and mesopores which functioned as efficient channels that facilitated the mass transport of reactants. Cyclic voltammograms showed that a catalyst without cobalt (Co_0-N-C) had a significantly

lower peak for oxygen reduction compared to those with cobalt (Co_{SA}-N-C and Co_{NP}-N-C). This confirmed the crucial role of cobalt in boosting the ORR activity. LSV curves revealed that Co_{SA}-N-C (moderate cobalt content) performed best among all the catalysts. It had a higher $E_{1/2}$ = 0.891 V compared to other electrocatalysts (Co_0-N-C $E_{1/2}$ = 0.775 V; CoNP-N-C $E_{1/2}$ = 0.870 V; commercial Pt/C $E_{1/2}$ = 0.852 V).

Ao K. and colleague [55] developed a strip-like Co-MOF CoNi alloy and CoO coupled nitrogen-doped carbon (NC) hybrids on carbon paper (CP) via a one-step pyrolysis with hierarchical pores and high specific surface area. OER response of CoNi-CoO@NC/CP showed a lower Tafel slope of 80.5 mV/dec and lowest R_{ct} value from EIS suggesting faster kinetics and efficient charge transfer capability in 0.1 M KOH. A similar response was also validated in 1 M KOH. The catalyst also proved to be highly stable from the 18 h and 64 h chronopotential tests. The catalyst was further tested in ZAB as an air cathode compared to RuO_2 + Pt/C. To further understand the rechargeability and stability of the catalyst, a galvanostatic discharge charge was conducted at 5 mA/cm^2, where RuO_2 + Pt/C cycled for 23 h while CoNi-CoO@NC/CP could go for 50 h. The excellent performance of CoNi-CoO@NC/CP was attributed to the high density of accessible catalytic sites and great ion diffusion into the inner and outer pores of the MOF awarding its superior performance.

2.4.4. High-entropy materials as bifunctional electrocatalysts

The appropriate pairing of several functional components can also result in the bifunctionality of the air cathode. This strategy provides greater flexibility in air cathode design by allowing researchers to optimise ORR and OER catalysts. High-entropy oxides (HEOs) allow tremendous flexibility in altering the electronic characteristics and catalytic response because of the interaction of five distinct metal species. These materials have unique properties which include [56]: (i) high-entropy effect caused by increased configurational entropy, which enables the formation of a stable single-phase solid solution structure as opposed to a brittle intermetallic compound; (ii) lattice distortion which results from the atomic size variation of the metallic atoms occupying a crystalline lattice, an effect that causes high-entropy materials (HEMs) to be hard and have poor electrical and thermal conductivity; (iii) sluggish diffusion caused by severe lattice distortion, which raises the energy barrier of atomic diffusion; and (iv)

cocktail effect is a term used to describe the HEMs' synergistic response as a result of their individual metallic components having different properties.

These materials are often synthesised at very high temperatures. Recent approaches have looked into low-temperature HEMs. He et al. [57] managed to prepare a HEA at 260 ^{o}C with excellent electrochemical response. The assembled cell provided an OCV of 1.489 V, a peak power density of 116.5 mW/cm^2, with 720 cycles at 8 mA/cm^2 and its flexible cell maintained 50 h of cycling at 5 mA/cm^2. Multicomponent high-entropy nanocomposites such as high-entropy alloy@high-entropy oxides (HEA@HEO) have also shown promising oxygen redox activity. Jin et al. [58] reported a BI of 0.61 V using this approach. Introducing carbon support has also been a synthesis approach in the preparation of HEMs. FeCoNiMnV HEA/N-CNTs, a high-entropy alloy supported by nitrogen-doped carbon nanotubes, demonstrated improved ORR activity with a battery performance of 566 h [59].

A study by Yu et al. [60] investigated the relevance of element ratios in HEO, as their electrochemical interaction was related to their ratios. In their work, they developed metal oxides with 3 to 8 elements and varying ratios and found that increasing some ratios does not necessarily change OER or ORR activity. A seven multicomponent HEO was made highly ORR active by incorporating Co atom and N co-doped carbon (CoNC) and achieved ΔE of 0.64 V. Its battery performance had an OCV of 1.50 V and a high peak power density of ~ 162 mW/cm^2. Furthermore, the battery achieved a high stable galvanostatic charge-discharge of 700 h at 2 mA/cm^2 with a maintained potential gap of 0.68 V. Excellent performance was also obtained even at higher current density (5 and 10 mA/cm^2). It is also evident that introducing defects to the HEMs can boost its catalytic response. This can be seen in the work by Ozgur et al. [61] who synthesised oxygen vacancy-rich spinel $(FeCrCoMnZn)_3O_{4-\delta}$ HEO through vacuum sintering (HEO-vac). HEO-vac showed superior OER/ORR activity with a bifunctional (BI) index of 0.89 V. During 300 h of cycling, the HEO-vac ZAB displayed a constant 2.0 V charge and 1.1 V discharge voltage with a 0.9 V voltage gap.

2.5. Zinc anode materials in RZABs

It is necessary to properly engineer the metallic anode to prevent corrosion and uneven dissolution and deposition of zinc. Lao-atiman and co-workers [13] suggests the use of a mechanical recharging approach to overcome dendrite growth, and morphology change and improve the battery cyclability. The mechanical recharge batteries present no major challenge because of the simple refuelling process done by physically substituting the Zn electrode and/or the Zn electrolyte. The design approach of a zinc anode should be a stable structure that enables long-stripping cycles of zinc ions without collapsing or changing its shape and support a uniform zinc deposition [62]. The design approaches should consider the surface of zinc, a zinc anode with a high surface area can cause self-corrosion and hydrogen evolution because of the enhanced contact between the anode and electrolyte. Hydrogen gas evolution, corrosion, and morphology change can be inhibited by coating zinc particles with other materials. Coatings function primarily to protect the active material from dissolving into the electrolyte during [63]. A large number of coating materials, such as metal oxides, polymers, or carbon, have been tested to avoid electrode shape change phenomena and increase the use and retention of the active material [63,64].

Wrapping Zn or ZnO with thin protective layers (e.g., GO, TiN_xO_y, and TiO_2) to form core/shell structures has been pursued. Wu et al. investigated ion-sieving carbon nanoshell-coated ZnO nanoparticles, to suppress the dissolution of zincate ions while allowing smaller hydroxide ions to pass through [21]. The nanosized ZnO was reported to prevent passivation, while the microporous layer of carbon slowed down the degradation of the Zn species. ZnO@C maintained its morphology confirming the ability of the carbon shell to reduce Zn dissolution and passivation. Their comparison study in a sealed coin cell set-up showed Zn foil to degrade after 7 cycles due to the passivation of ZnO, while bare ZnO lasted for 20 cycles with ZnO@C having ~1.6 times longer cycle life. The authors also went to test the ZnO@C on a pouch cell with an electrolyte saturated with ZnO, the battery reached 100 cycles with > 90% efficiency under 100% depth-of-discharge (DOD) at 1C [21]. Another ZnO@C pouch cell cycled at 500 cycles showed ~95% efficiency and 100% retention at 12C. Another study by Vatsalarani and colleagues found that a fibrous polyaniline coating network on a porous zinc electrode allowed the movement of hydroxide ions but limited the

diffusion of zincate ions [65]. The coated electrode exhibited a uniform surface morphology after 100 cycles, smoother than the untreated zinc electrode. A similar approach was conducted with a TiO_2 shell [66], where the material obtained 40% DOD under deep cycling performance for 170 cycles. A 3.2 wt% Bismuth, calcium, and zinc oxide glass composite coating was investigated to modify the zinc anode [67]. The improved performance was accounted for by the Bi pathways and trapping of zincate ions inside the coating layer, thus resulting in improved zinc utilisation and rechargeability.

The incorporation of additives (such as Al_2O_3, Bi_2O_3, and In_2O_3) and alloying zinc with other metals (such as cadmium, bismuth, nickel, palladium, aluminium, magnesium, tin, and indium) can help to stabilise the zinc electrode [68–70]. They also increase conductivity, improve current distribution, and promote the formation of compact, thin Zn deposits [12]. The study by Lee et al. [70] explored the use of zinc alloyed with nickel and indium. They discovered that a specific combination of 90% zinc, 7.5% nickel, and 2.5% indium exhibited a more negative overpotential shift (-1.725 V) compared to pure zinc (-1.609 V). This alloy also maintained good reversibility even after 100 cycles and showed a lower corrosion current. A study by Lee et al. demonstrated that the application of an Al_2O_3 layer onto zinc particles mitigates both corrosion and hydrogen gas evolution. Their findings indicate that a zinc electrode containing 0.25 wt% Al_2O_3 coating exhibits a 50% improvement in discharge duration compared to a bare zinc electrode when tested in a 9 M KOH electrolyte [71]. The coated zinc anode provided a discharge time of more than 10 h, with the pristine zinc anode delivering only 7 h at 25 mA/cm^2. The battery material held its morphology even after repeated charging and discharging cycles. In addition, attempts were also made to coat Zn anodes with surface trapping layers for better preservation of the soluble zincate ions to improve the electrode reversibility [12].

Other ways to modify the zinc anode have been investigated, including the use of 3D sponges, fibres, and foams. The structures are made up of an interconnected zinc domain to promote an even current diffusion as well as increased electron and ionic transport. Parker et al. [72] report a 3D Zn sponge structure, which was tested in a symmetric Zn||Zn@ZnO cell. The cell managed to achieve a 23% DOD from its discharge capacity at 24 mA/cm^2. This design acts like a sponge for zinc oxide (ZnO),

capturing it within its empty spaces. This trapping mechanism helps prevent the formation of dendrites. As a result, the battery performs better when discharging and utilises more of the zinc material. Researchers have also explored another 3D material for battery applications. This one consisted of nanoscale zinc oxide particles embedded in a hierarchically structured porous carbon matrix derived from MOF-5 [73]. Similarly, improvement in zinc utilisation was reported, with a realised 32.6% DOD of its specific capacity and discharge capacity retention over 60 cycles. Furthermore, zinc was electrodeposited on a copper foam coated with a thin layer of silver to increase its hydrogen overpotential, lowering the self-corrosion of zinc. The researchers went on to fabricate a RZAB which cycled at 2h per cycle and achieved 94% Coulombic efficiency after 80 h.

2.6. Electrolytes in zinc-air battery

Electrolytes play a very important role in driving reactions because they effectively connect the air electrode with the overall system. Several electrolytes have been used in zinc-air battery testing such as ionic liquids, LiOH, KOH, NaOH, and neutral NH_4Cl. KOH is mostly preferred because of its higher oxygen diffusion coefficient, good electrochemical kinetics, moderate Zn solubility, lower viscosity, and high ionic conductivity [74,75]. The optimal concentration of KOH was found to be around 6-7 M [13]. However, higher electrolyte concentration can cause ZnO build-up and dendrite growth [76]. Suitable electrolyte additives can improve the shape change of the zinc electrode as well as the ZAB performance. Changes in the anode morphology and redistribution of zinc can be mitigated by adding certain compounds to reduce or prevent zinc dissolution in alkaline electrolytes [77]. These compounds form insoluble complexes with zinc and/or change the pH of the electrolyte. Compounds containing fluoride (KF), borate (K_3BO_3), phosphate (K_3PO_4), arsenate (K_3AsO_4), and carbonate (K_2CO_3) can be used because they have shown reduced solubility of zinc compound. Alder et al. investigated an advanced electrolyte composition consisting of 4 M KOH, 2 M KF, 2 M K_2CO_3, and saturated ZnO, to ensure a uniform zinc deposition layer during charging [78]. K_2CO_3 has also been incorporated into the alkaline electrolyte to reduce the kinetics of the formation of carbonate species [79]. The work concluded that adding about 30 mol% of potassium carbonate to a high molar KOH electrolyte is

acceptable in extending the lifetime of the RZAB, although with a penalty for marginal battery performance loss.

Ionic liquids (ILs) have been considered to be potential electrolytes in RZABs because of their large electrochemical window, high stability, and non-volatility [62]. Most importantly they have been reported to solve electrolyte evaporation, degradation of CO_2, prevention of HER-induced corrosion, and no water leakage during charge/discharge [62,80]. Clark et al. investigated four different electrolyte systems (designated E4, E6, E7, and E8) prepared from $ZnCl_2$ and NH_4Cl and the pH was adjusted with NH_4OH [74]. Amongst the electrolytes, E7 showed a higher conductivity of 382 mS/cm, this was assumed to be due to a higher ionic concentration of NH_4Cl but was lower than that of KOH (638 mS/cm). However, the oxygen levels were two times higher than those of KOH, while the viscosity was around half of KOH. In the work by Sakthivel et al. [81] an aqueous choline acetate (ChAcO) containing 30 wt% water was used as the electrolyte. Its conductivity and pH were measured to be 5.9 mS/cm and 10.8, respectively. After a 100 h of charge/discharge at 100 $\mu A/cm^2$, the ZAB achieved a reversible capacity of 25.4 mAh (28% DOD) with energy efficiency ranging between 29 to 54% for the first and seventh cycles in a 1500 h polarisation period. Unlike in KOH at a pH of ca. 11, neither carbonate nor zinc dendrite formation was observed in the choline acetate electrolyte.

More stable Zn corrosion products are produced under neutral or slightly alkaline conditions such as $Zn(OH)_2$ [77]. Aqueous electrolytes with near-neutral pH values are carbonation resilient and may increase the lifetime of RZAB [82]. However, in the near-neutral pH system, ZnO and $Zn(OH)_2$ are usually insoluble [74]. The most popular near-neutral electrolyte (NNE) is $ZnCl_2$-NH_4Cl, which has been used in zinc-based LeClanché batteries (also called L-ZAB) for more than 100 years. Clark et al. performed a theoretical test to investigate L-ZAB, the test predicted that the electrolyte was acidic during charging and a mixture of Zn salts excluding ZnO dominated the discharge process [74]. This resulted in material degradation, electrolyte consumption, and lower practical energy density [74]. Changing the electrolyte to non-aqueous affected the reaction pathways of OER and ORR and reduced the reaction kinetics [12]. Despite slowing down the corrosion of Zn, dendrite growth, and electrolyte evaporation, the performance of Zn is reduced as a result of surface passivation.

The open system of the zinc-air battery has water loss from the aqueous electrolyte [19]. Gelled electrolytes have been used to minimise water loss and improve the battery's performance as well as its cycle life. Mohamad demonstrated that a 6 M KOH/hydroponics gel battery with an enhanced specific capacity of 657.5 mAh/g (789 W/kg) compared to the theoretical value of a ZAB (820 mAh/g) [83]. The lower capacitive response was reported to be due to the compactness of the Zn plate. The shape of the zinc plate was preserved after battery discharge. However, a passivation layer was observed, which blocked the use of the Zn anode, resulting in cell failure. Yang and co-worker investigated a polymer gel electrolyte composed of KOH dissolved in polyethylene oxide (PEO) and polyvinyl alcohol (PVA) polymer matrix [84]. The polymer electrolyte exhibited great mechanical strength, electrochemical stability, and a high capacity of 1305 mAh (theoretical capacity: 1560 mAh, utilisation of zinc = 83.65%). Chen's group developed a nanoporous alkaline exchange electrolyte membrane from natural cellulose nanofibers with a high ionic conductivity of 21.2 mS/cm with 95.6% water retention and excellent flexibility in bending [85]. However, this type of electrolyte generated oxygen bubbles from the ORR and reduced the conductivity. Higher dissolved oxygen concentration is advantageous for the ORR kinetics, and low viscosity allows to achieve successful air electrode transportation and wetting behaviour [74]. In contrast, lower electrolyte viscosity could increase the risk of air electrode flooding [74].

2.7. Reference

[1] P. Chen, F. Bai, J. wen Deng, B. Liu, T. Zhang, Recent progresses and challenges in aqueous lithium–air batteries relating to the solid electrolyte separator: A mini-review, Front Chem 10 (2022) 1035691. doi.org/10.3389/fchem.2022.1035691.

[2] N. Imanishi, O. Yamamoto, Perspectives and challenges of rechargeable lithium–air batteries, Mater Today Adv 4 (2019) 100031. doi.org/10.1016/j.mtadv.2019.100031.

[3] Q. Liu, Z. Chang, Z. Li, X. Zhang, Flexible metal–air batteries: Progress, challenges, and perspectives, Small Methods 2 (2018) 1700231. doi.org/10.1002/smtd.201700231.

[4] W. Wang, Y.-C. Lu, The potassium–air battery: Far from a practical reality?, Acc Mater Res 2 (2021) 515–525. doi.org/10.1021/accountsmr.1c00061.

[5] Y. Wang, Y. Sun, W. Ren, D. Zhang, Y. Yang, J. Yang, J. Wang, X. Zeng, Y. NuLi, Challenges and prospects of Mg-air batteries: a review, Energy Materials 2 (2022) 200024. doi.org/10.20517/energymater.2022.20.

[6] J. Lee, S. Tai Kim, R. Cao, N. Choi, M. Liu, K.T. Lee, J. Cho, Metal–air batteries with high energy density: Li–air versus Zn–air, Adv Energy Mater 1 (2011) 34–50. doi.org/10.1002/aenm.201000010.

[7] Y. Li, J. Lu, Metal–air batteries: Will they be the future electrochemical energy storage device of choice?, ACS Energy Lett 2 (2017) 1370–1377. doi.org/10.1021/acsenergylett.7b00119.

[8] A.G. Olabi, E.T. Sayed, T. Wilberforce, A. Jamal, A.H. Alami, K. Elsaid, S.M.A. Rahman, S.K. Shah, M.A. Abdelkareem, Metal-air batteries - A Review, Energies (Basel) 14 (2021) 7373. doi.org/10.3390/en14217373.

[9] P. Teabnamang, W. Kao-ian, M.T. Nguyen, T. Yonezawa, R. Cheacharoen, S. Kheawhom, High-capacity dual-electrolyte aluminum–air battery with circulating methanol anolyte, Energies (Basel) 13 (2020) 2275. doi.org/10.3390/en13092275.

[10] S.S. Shinde, J.Y. Jung, N.K. Wagh, C.H. Lee, D.-H. Kim, S.-H. Kim, S.U. Lee, J.-H. Lee, Ampere-hour-scale zinc–air pouch cells, Nat Energy 6 (2021) 592–604. doi.org/10.1038/s41560-021-00807-8.

[11] P. Yu, Y. Zeng, H. Zhang, M. Yu, Y. Tong, X. Lu, Flexible Zn-ion batteries: Recent progresses and challenges, Small 15 (2019) 1804760. doi.org/10.1002/smll.201804760.

[12] J. Zhang, Q. Zhou, Y. Tang, L. Zhang, Y. Li, Zinc-air batteries: Are they ready for prime time?, Chem Sci 10 (2019) 8924. doi.org/10.1039/c9sc04221k.

[13] W. Lao-atiman, K. Bumroongsil, A. Arpornwichanop, P. Bumroongsakulsawat, S. Olaru, S. Kheawhom, Model-based analysis of an integrated zinc-air flow battery/zinc electrolyzer system, Front Energy Res 7 (2019) 15. doi.org/10.3389/fenrg.2019.00015.

[14] P. Gu, M. Zheng, Q. Zhao, X. Xiao, H. Xue, H. Pang, Rechargeable zinc-air batteries: A promising way to green energy, J Mater Chem A Mater 5 (2017) 7651–7666. doi.org/10.1039/c7ta01693j.

[15] P. Chen, K. Zhang, D. Tang, W. Liu, F. Meng, Q. Huang, J. Liu, Recent progress in electrolytes for Zn–air batteries, Front Chem 8 (2020) 372. doi.org/10.3389/fchem.2020.00372.

[16] M. Kar, T.J. Simons, M. Forsyth, D.R. MacFarlane, Ionic liquid electrolytes as a platform for rechargeable metal–air batteries: A perspective, Phys. Chem. Chem. Phys. 16 (2014) 18658–18674. doi.org/10.1039/C4CP02533D.

[17] Z. Wu, H. Wang, P. Xiong, G. Li, T. Qiu, W. Bin Gong, F. Zhao, C. Li, Q. Li, G. Wang, F. Geng, Molecularly thin nitride sheets stabilized by titanium carbide as efficient bifunctional electrocatalysts for fiber-shaped rechargeable zinc-air batteries, Nano Lett 20 (2020) 2892–2898. doi.org/10.1021/acs.nanolett.0c00717.

[18] P. Ganesan, P. Ramakrishnan, M. Prabu, S. Shanmugam, Nitrogen and sulfur Co-doped graphene supported cobalt sulfide nanoparticles as an efficient air cathode for zinc-air battery, Electrochim Acta 183 (2015) 63–69. doi.org/10.1016/j.electacta.2015.05.182.

[19] Y. Li, H. Dai, Recent advances in Zinc-air batteries, Chem Soc Rev 43 (2014) 5257. doi.org/10.1039/c4cs00015c.

[20] S. Gull, C.-C. Weng, H.-Y. Chen, Carbon armor for zinc anodes: Mitigating dendrite formations and unwanted side reactions in zinc-ion batteries, J Taiwan Inst Chem Eng 154 (2024) 104977. doi.org/10.1016/j.jtice.2023.104977.

[21] Y. Wu, Y. Zhang, Y. Ma, J.D. Howe, H. Yang, P. Chen, S. Aluri, N. Liu, Ion-sieving carbon nanoshells for deeply rechargeable Zn-based aqueous batteries, Adv Energy Mater 8 (2018) 1802470. doi.org/10.1002/aenm.201802470.

[22] David S. Wilkinson, Mass transport in solids and fluids, Cambridge University Press, 2000.

[23] A. Paul, T. Laurila, V. Vuorinen, S. V. Divinski, Thermodynamics, diffusion and the Kirkendall effect in solids, 2014. doi.org/10.1007/978-3-319-07461-0.

[24] N. Bhuvanendran, S. Ravichandran, Q. Xu, T. Maiyalagan, H. Su, A quick guide to the assessment of key electrochemical performance indicators for the oxygen reduction reaction: A comprehensive review, Int J Hydrogen Energy 47 (2022) 7113–7138. doi.org/10.1016/j.ijhydene.2021.12.072.

[25] S.S. Beshahwored, Cyclic voltammetric (CV) evaluation of electro chemical behaviors of $K_3[Fe(CN)_6]$ and uric acid, Journal of Nutrition and Food Science 11 (2021) 806.

[26] N. Elgrishi, K.J. Rountree, B.D. McCarthy, E.S. Rountree, T.T. Eisenhart, J.L. Dempsey, A practical beginner's guide to cyclic voltammetry, J Chem Educ 95 (2018) 197-206. doi.org/10.1021/acs.jchemed.7b00361.

[27] S.B. Aziz, M.A. Brza, I. Brevik, M.H. Hamsan, R.T. Abdulwahid, S.R. Majid, M.F.Z. Kadir, S.A. Hussen, R. M. Abdullah, Characteristics of glycerolized chitosan: NH_4NO_3-based polymer electrolyte for energy storage devices with extremely high specific capacitance and energy density over 1000 cycles, Polymers (Basel) 12 (2020) 2718. doi.org/10.3390/polym12112718.

[28] R.K. Franklin, S.M. Martin, T.D. Strong, R.B. Brown, Chemical and Biological Systems: Chemical Sensing Systems for Liquids, Elsevier, 2016. doi.org/10.1016/B978-0-12-803581-8.00549-X.

[29] J. Nikolic, E. Expósito, J. Iniesta, J. González-Garcia, V. Montiel, Theoretical concepts and applications of a rotating disk electrode, J Chem Educ 77 (2000) 1191. doi.org/10.1021/ed077p1191.

[30] R.G. Compton, E. Kätelhön, K.R. Ward, E. Laborda, Understanding Voltammetry: simulation of electrode processes, 2nd edition, World scientific (Europe), 2020. doi.org/10.1142/q0246.

[31] J.L. Town, F. MacLaren, H.D. Dewald, Rotating disk voltammetry experiment, J Chem Educ 68 (1991) 352. doi.org/10.1021/ed068p352.

[32] Y. Jiao, Y. Zheng, M. Jaroniec, S.Z. Qiao, Design of electrocatalysts for oxygen- and hydrogen-involving energy conversion reactions, Chem Soc Rev 44 (2015) 2060–2086. doi.org/10.1039/C4CS00470A.

[33] M. Kuang, P. Han, L. Huang, N. Cao, L. Qian, G. Zheng, Electronic tuning of Co, Ni-based nanostructured (hydr)oxides for aqueous electrocatalysis, Adv Funct Mater 28 (2018) 1804886. doi.org/10.1002/adfm.201804886.

[34] R. Wang, Z. Chen, N. Hu, C. Xu, Z. Shen, J. Liu, Nanocarbon-based electrocatalysts for rechargeable aqueous Li/Zn-air batteries, ChemElectroChem 5 (2018) 1745–1763. doi.org/10.1002/celc.201800141.

[35] O.O. Fashedemi, K.I. Ozoemena, Enhanced methanol oxidation and oxygen reduction reactions on palladium-decorated FeCo@Fe/C core–shell nanocatalysts in alkaline medium, Physical Chemistry Chemical Physics 15 (2013) 20982–20991. doi.org/10.1039/c3cp52601a.

[36] L. Bouleau, S. Pérez-Rodríguez, J. Quílez-Bermejo, M.T. Izquierdo, F. Xu, V. Fierro, A. Celzard, Best practices for ORR performance evaluation of metal-free porous carbon electrocatalysts, Carbon N Y 189 (2022) 349–361. doi.org/10.1016/j.carbon.2021.12.078.

[37] A. Gabe, R. Ruiz-Rosas, C. González-Gaitán, E. Morallón, D. Cazorla-Amorós, Modeling of oxygen reduction reaction in porous carbon materials in alkaline medium. Effect of microporosity, J Power Sources 412 (2019) 451–464. doi.org/10.1016/j.jpowsour.2018.11.075.

[38] M. Stern, A.L. Geary, Electrochemical polarization, J Electrochem Soc 104 (1957) 56. doi.org/10.1149/1.2428496.

[39] S. Hiromoto, Corrosion of metallic biomaterials, Elsevier, 2010: pp. 99–121. doi.org/10.1533/9781845699246.2.99.

[40] A.J. Bard, L.R. Faulkner, Electrochemical methods: Fundamentals and applications, 2nd edition, 2000, John Wiley & Sons.

[41] N. Raeisi-Kheirabadi, A. Nezamzadeh-Ejhieh, H. Aghaei, Cyclic and linear sweep voltammetric studies of a modified carbon paste electrode with nickel oxide nanoparticles toward tamoxifen: effects of surface modification on electrode response kinetics, ACS Omega 7 (2022) 31413–31423. doi.org/10.1021/acsomega.2c03441.

[42] Z. Lukács, T. Kristóf, Determination of kinetic parameters from a new quadratic approximation of the Butler-Volmer equation, Journal of Electroanalytical Chemistry 918 (2022) 116443. doi.org/10.1016/j.jelechem.2022.116443.

[43] M. El-Azazy, M. Min, P. Annus, eds., Electrochemical Impedance Spectroscopy, IntechOpen, 2021. doi.org/10.5772/intechopen.87884.

[44] A.Ch. Lazanas, M.I. Prodromidis, Electrochemical Impedance Spectroscopy - A Tutorial, ACS Measurement Science Au 3 (2023) 162–193. doi.org/10.1021/acsmeasuresciau.2c00070.

[45] J.F. Parker, J.S. Ko, D.R. Rolison, J.W. Long, Translating materials-level performance into device-relevant metrics for zinc-based batteries, Joule 2 (2018) 2519–2527. doi.org/10.1016/j.joule.2018.11.007.

[46] J. Milikić, A. Nastasić, M. Martins, C.A.C. Sequeira, B. Šljukić, Air cathodes and bifunctional oxygen electrocatalysts for aqueous metal–air batteries, Batteries 9 (2023) 394. doi.org/10.3390/batteries9080394.

[47] Z.W. Seh, J. Kibsgaard, C.F. Dickens, I. Chorkendorff, J.K. Nørskov, T.F. Jaramillo, Combining theory and experiment in electrocatalysis: Insights into materials design, Science (1979) 355 (2017). doi.org/10.1126/science.aad4998.

[48] J.K. Nørskov, J. Rossmeisl, A. Logadottir, L. Lindqvist, J.R. Kitchin, T. Bligaard, H. Jónsson, Origin of the overpotential for oxygen reduction at a fuel-cell cathode, J Phys Chem B 108 (2004) 17886–17892. doi.org/10.1021/jp047349j.

[49] N. Daems, X. Sheng, I.F.J. Vankelecom, P.P. Pescarmona, Metal-free doped carbon materials as electrocatalysts for the oxygen reduction reaction, J. Mater. Chem. A 2 (2014) 4085–4110. doi.org/10.1039/C3TA14043A.

[50] P. Saha, S. Shaheen Shah, M. Ali, M. Nasiruzzaman Shaikh, Md.A. Aziz, A.J. Saleh Ahammad, Cobalt oxide-based electrocatalysts with bifunctionality for high-performing rechargeable zinc-air batteries, The Chemical Record 24 (2024) e202300216. doi.org/10.1002/tcr.202300216.

[51] P. Leng, F. Luo, M. Li, S. Ma, X. Long, Z. Yang, Construction of abundant $Co_3O_4/Co(OH)_2$ heterointerfaces as air electrocatalyst for flexible all-solid-state zinc-

air batteries, Electrochim Acta 413 (2022) 140158. doi.org/10.1016/j.electacta.2022.140158.

[52] L. Wang, Z. Xu, T. Peng, M. Liu, L. Zhang, J. Zhang, Bifunctional single-atom cobalt electrocatalysts with dense active sites prepared via a silica xerogel strategy for rechargeable zinc–air batteries, Nanomaterials 12 (2022) 381. doi.org/10.3390/nano12030381.

[53] X. Yi, X. He, F. Yin, B. Chen, G. Li, H. Yin, Co-CoO-Co_3O_4/N-doped carbon derived from metal-organic framework: The addition of carbon black for boosting oxygen electrocatalysis and Zn-air battery, Electrochim Acta 295 (2019) 966–977. doi.org/10.1016/j.electacta.2018.11.142.

[54] L. Zhou, P. Zhou, Y. Zhang, B. Liu, P. Gao, S. Guo, 3D star-like atypical hybrid MOF derived single-atom catalyst boosts oxygen reduction catalysis, Journal of Energy Chemistry 55 (2021) 355–360. doi.org/10.1016/j.jechem.2020.06.059.

[55] K. Ao, W.A. Daoud, Facile controlled formation of CoNi alloy and CoO embedded in N-doped carbon as advanced electrocatalysts for oxygen evolution and zinc-air battery, Electrochim Acta 395 (2021) 139204. doi.org/10.1016/j.electacta.2021.139204.

[56] A.B. Haruna, E.U. Onoh, K.I. Ozoemena, Emerging high-entropy materials as electrocatalysts for rechargeable zinc–air batteries, Curr Opin Electrochem 39 (2023) 101264. doi.org/10.1016/j.coelec.2023.101264.

[57] R. He, L. Yang, Y. Zhang, X. Wang, S. Lee, T. Zhang, L. Li, Z. Liang, J. Chen, J. Li, A. Ostovari Moghaddam, J. Llorca, M. Ibáñez, J. Arbiol, Y. Xu, A. Cabot, A CrMnFeCoNi high-entropy alloy boosting oxygen evolution/reduction reactions and zinc-air battery performance, Energy Storage Mater 58 (2023) 287–298. doi.org/10.1016/j.ensm.2023.03.022.

[58] Z. Jin, X. Zhou, Y. Hu, X. Tang, K. Hu, K.M. Reddy, X. Lin, H.-J. Qiu, A fourteen-component high-entropy alloy@oxide bifunctional electrocatalyst with a record-low Δ E of 0.61 V for highly reversible Zn–air batteries, Chem Sci 13 (2022) 12056–12064. doi.org/10.1039/D2SC04461G.

[59] D.-H. Wu, M. Ul Haq, L. Zhang, J.-J. Feng, F. Yang, A.-J. Wang, Noble metal-free FeCoNiMnV high-entropy alloy anchored on N-doped carbon nanotubes with prominent activity and durability for oxygen reduction and zinc–air batteries, J Colloid Interface Sci 662 (2024) 149–159. doi.org/10.1016/j.jcis.2024.02.044.

[60] T. Yu, H. Xu, Z. Jin, Y. Zhang, H.-J. Qiu, Noble metal-free high-entropy oxide/Co-N-C bifunctional electrocatalyst enables highly reversible and durable Zn-air batteries, Appl Surf Sci 610 (2023) 155624. doi.org/10.1016/j.apsusc.2022.155624.

[61] C. Ozgur, T. Erdil, U. Geyikci, C. Okuyucu, E. Lokcu, Y.E. Kalay, C. Toparli, Engineering oxygen vacancies in $(FeCrCoMnZn)_3O_{4-\delta}$ high-entropy spinel oxides through altering fabrication atmosphere for high-performance rechargeable zinc-air batteries, Global Challenges 8 (2024). doi.org/10.1002/gch2.202300199.

[62] S.K. Yadav, D. Deckenbach, J.J. Schneider, Secondary zinc–air batteries: A view on rechargeability aspects, Batteries 8 (2022) 244. hdoi.org/10.3390/batteries8110244.

[63] J. Fu, Z.P. Cano, M.G. Park, A. Yu, M. Fowler, Z. Chen, Electrically rechargeable zinc–air batteries: Progress, challenges, and perspectives, Advanced Materials 29 (2017) 1604685. doi.org/10.1002/adma.201604685.

[64] D. Stock, S. Dongmo, F. Walther, J. Sann, J. Janek, D. Schröder, Homogeneous coating with an anion-exchange ionomer improves the cycling stability of secondary batteries with zinc anodes, ACS Appl Mater Interfaces 10 (2018) 8640–8648. doi.org/10.1021/acsami.7b18623.

[65] J. Vatsalarani, D.C. Trivedi, K. Ragavendran, P.C. Warrier, Effect of polyaniline coating on “shape change” phenomenon of porous zinc electrode, J Electrochem Soc 152 (2005) A1974–A1978. doi.org/10.1149/1.2008992.

[66] Y. Zhang, Y. Wu, W. You, M. Tian, P.-W. Huang, Y. Zhang, Z. Sun, Y. Ma, T. Hao, N. Liu, Deeply rechargeable and hydrogen-evolution-suppressing zinc anode in alkaline aqueous electrolyte, Nano Lett 20 (2020) 4700–4707. doi.org/10.1021/acs.nanolett.0c01776.

[67] M. Schmid, M. Willert-Porada, Zinc particles coated with bismuth oxide-based glasses as anode material for zinc air batteries with improved electrical rechargeability, Electrochim Acta 260 (2018) 246–253. doi.org/10.1016/j.electacta.2017.12.041.

[68] Y. Sato, M. Takahashi, H. Asakura, T. Yoshida, K. Tada, K. Kobayakawa, N. Chiba, K. Yoshida, Gas evolution behavior of Zn alloy powder in KOH solution, J Power Sources 38 (1992) 317–325. doi.org/10.1016/0378-7753(92)80121-Q.

[69] D.P. Bhatt, R. Udhayan, Electrochemical studies on a zinc-lead-cadmium alloy in aqueous ammonium chloride solution, J Power Sources 47 (1994) 177–184. doi.org/10.1016/0378-7753(94)80059-6.

[70] C.W. Lee, K. Sathiyanarayanan, S.W. Eom, M.S. Yun, Novel alloys to improve the electrochemical behavior of zinc anodes for zinc/air battery, J Power Sources 160 (2006) 1436–1441. doi.org/10.1016/j.jpowsour.2006.02.019.

[71] S.M. Lee, Y.J. Kim, S.W. Eom, N.S. Choi, K.W. Kim, S.B. Cho, Improvement in self-discharge of Zn anode by applying surface modification for Zn-air batteries with high energy density, J Power Sources 227 (2013) 177–184. doi.org/10.1016/j.jpowsour.2012.11.046.

[72] J.F. Parker, C.N. Chervin, E.S. Nelson, D.R. Rolison, J.W. Long, Wiring zinc in three dimensions re-writes battery performance-dendrite-free cycling, Energy Environ. Sci. 7 (2014) 1117–1124. doi.org/10.1039/C3EE43754J.

[73] D. Deckenbach, J.J. Schneider, A 3D hierarchically porous nanoscale ZnO anode for high-energy rechargeable zinc-air batteries, J Power Sources 488 (2021) 229393. doi.org/10.1016/j.jpowsour.2020.229393.

[74] S. Clark, A.R. Mainar, E. Iruin, L.C. Colmenares, J.A. Blázquez, J.R. Tolchard, A. Latz, B. Horstmann, Towards Rechargeable Zinc-Air Batteries with Aqueous Chloride Electrolytes, J. Mater. Chem. A 7 (2019) 11387–11399. https://doi.org/10.1039/C9TA01190K.

[75] D.M. See, R.E. White, Temperature and concentration dependence of the specific conductivity of concentrated solutions of potassium hydroxide, J Chem Eng Data 42 (1997) 1266–1268. doi.org/10.1021/je970140x.

[76] F.R. McLarnon, E.J. Cairns, The secondary alkaline zinc electrode, J Electrochem Soc 138 (2019) 645–656. doi.org/10.1149/1.2085653.

[77] A.R. Mainar, E. Iruin, L.C. Colmenares, A. Kvasha, I. de Meatza, M. Bengoechea, O. Leonet, I. Boyano, Z. Zhang, J.A. Blazquez, An overview of progress in electrolytes for secondary zinc-air batteries and other storage systems based on zinc, J Energy Storage 15 (2018) 304–328. doi.org/10.1016/j.est.2017.12.004.

[78] T.C. Adler, F.R. Mclarnon, E.J. Cairns, Low-zinc-solubility electrolytes for use in zinc/nickel oxide cells, 140 (1993) 289. doi.org/10.1149/1.2221039.

[79] D. Schröder, N.N. Sinai Borker, M. König, U. Krewer, Performance of zinc air batteries with added K_2CO_3 in the alkaline electrolyte, J Appl Electrochem 45 (2015) 427–437. doi.org/10.1007/s10800-015-0817-0.

[80] M. Yoshizawa, W. Xu, C.A. Angell, Ionic liquids by proton transfer: Vapor pressure, conductivity, and the relevance of ΔpKa from aqueous solutions, J Am Chem Soc 125 (2003) 15411–15419. doi.org/10.1021/ja035783d.

[81] M. Sakthivel, S.P. Batchu, A.A. Shah, K. Kim, W. Peters, J.-F. Drillet, An electrically rechargeable zinc/air cell with an aqueous choline acetate electrolyte, Materials 13 (2020) 2975. doi.org/10.3390/ma13132975.

[82] L. An, Z. Zhang, J. Feng, F. Lv, Y. Li, R. Wang, M. Lu, R.B. Gupta, P. Xi, S. Zhang, Heterostructure-promoted oxygen electrocatalysis enables rechargeable zinc-air battery with neutral aqueous electrolyte, J Am Chem Soc 140 (2018) 17624–17631. doi.org/10.1021/jacs.8b09805.

[83] A.A. Mohamad, Zn/gelled 6 M KOH/O_2 zinc-air battery, J Power Sources 159 (2006) 752–757. doi.org/10.1016/j.jpowsour.2005.10.110.

[84] C.C. Yang, S.J. Lin, Alkaline composite PEO-PVA-glass-fibre-mat polymer electrolyte for Zn-air battery, J Power Sources 112 (2002) 497–503. doi.org/10.1016/S0378-7753(02)00438-X.

[85] J. Fu, J. Zhang, X. Song, H. Zarrin, X. Tian, J. Qiao, L. Rasen, K. Li, Z. Chen, A flexible solid-state electrolyte for wide-scale integration of rechargeable zinc-air batteries, Energy Environ Sci 9 (2016) 663–670. doi.org/10.1039/c5ee03404c.

CHAPTER 3
EXPERIMENTAL PROCEDURE

This Chapter lists the chemicals and reagents used for the synthesis of the cathode and anode materials used in this work. The experimental procedures, and physical and electrochemical characterisation techniques used to study the properties of the synthesised materials are also discussed**.**

3.1. Materials and reagents

All the reagents used were of analytical grade and used without further purification. The reagents included ethanol (C_2H_6O, 99.9%), isopropyl alcohol (C_3H_8O, 99.9%), Millipore water (resistivity value of 18.2 MΩ.cm, collected from the Milli-Q water system), Nafion perfluorinated resin solution (5 wt% containing a mixture of lower aliphatic alcohols and water, contains 45% water) ethylene glycol (EG, $C_2H_6O_2$, 99.8 %), acetone (C_3H_6O, 99.9%), zinc acetate ($Zn(CH_2COO)_2{\cdot}2H_2O$, 98%), potassium hydroxide pellets (KOH, ≥85%), carbon black (CB, Timical Super C45), citric acid (CA, 99.5%), copper nitrate trihydrate ($Cu(NO_3)_2{\cdot}3H_2O$, 98%), nickel nitrate hexahydrate ($Ni(NO_3)_2{\cdot}6H_2O$, 98.5%), manganese nitrate hexahydrate ($Mn(NO_3)_2{\cdot}6H_2O$, 98%), iron nitrate nonahydrate ($Fe(NO_3)_2{\cdot}9H_2O$, 98%), potassium ferricyanide ($K_3Fe(CN)_6$, 99%), potassium ferrocyanide ($K_4Fe(CN)_6$, 98.5%), potassium chloride (KCl, 99%), sodium hydroxide (NaOH, 98%), Tris-buffer (pH 8.5), dopamine hydrochloride ($C_8H_{11}NO_2{\cdot}HCl$), cobalt nitrate hexahydrate ($Co(NO_3)_6.6H_2O$, 98%), hydrochloric acid (HCl), ZnO (<100 nm particle size, 99.9%) 4,4'-biphenyl dicarboxylic acid (BPDC, $HO_2CC_6H_4C_6H_4CO_2H$, 97%), platinum on carbon (Pt/C, 20wt%), iridium oxide (IrO_2, 99.9%), dimethylformamide (DMF, $HCON(CH_3)_2$, 99.8%), polytetrafluoroethylene (PTFE, 60 wt % dispersion in water), Alumina powder (50 nm), poly(vinyl alcohol) (PVA, 99%), carbon paper, copper strip, nickel foam (1.6 mm thickness, 95%) and zinc foil (0.25 mm thickness, 99%).

3.2. Methodology

3.2.1. Synthesis of material used in this work

- Co-MOF was synthesised through a microwave-assisted solvothermal process and used as a sacrificial template for the preparation of Co-MOF-derived carbons of cobalt nanoparticles (Co NP@C_{BPDC}) and cobalt atomic clusters (Co AC@C_{BPDC}). The parent material was carbonised to produce Co NP which was acid-treated to produce Co AC.
- HESOx was synthesised by using equimolar ratios of $Cu(NO_3)_2$, $Co(NO_3)_2$, $Ni(NO_3)_2$, $Mn(NO_3)_2$, and $Fe(NO_3)_2$ nitrate salt solution and reacted through the Pechini method. The resulting powder was annealed to 500 ^oC and 750 ^oC resulting in HESOx-500 and HESOx-750.
- ZnO was prepared using a well-established method and incorporation of microwave irradiation. For comparison, commercial ZnO (<100 nm particle size) was also used. The materials were coated with dopamine in a Tris-buffer (pH 8.5) solution at a mass ratio of 2:1, followed by annealing to give zinc oxide core-shell coated with polydopamine (PDA) derived carbon (ZnO@PDA-DC). ZnO_c, ZnO_l, and ZnO_{mw} were used to represent commercial, conventional, and microwave synthesis approaches.

3.2.2. Preparation of ferrous ferricyanide solution

A ferrous ferricyanide solution was made by weighing equimolar concentrations of 3 mM ferricyanide and ferrocyanide in 0.1 M KCl. The compounds were dissolved to 100 mL with Millipore water.

3.3. Physical characterisation techniques

3.3.1. Powder X-ray diffraction (P-XRD)

The P-XRD of the samples was obtained using a D2 Phaser in Bragg-Brentano configuration equipped with CuKα (λ = 1.54056 Å) radiation tube. The P-XRD diffractograms were obtained in the 2θ degree range of 5 - 90. The particle sizes were calculated from the Scherrer equation (equation 3.1) using Miller indexes of dominant peaks.

$$D = \frac{K\lambda}{\beta \mathrm{Cos}\theta} \quad (3.1)$$

where D is the average crystallite size in nm, K is the dimensionless shape factor or Scherrer constant (value 0.9), λ is the wavelength of the X-ray source (CuKα = 0.15406 nm), β is the full-width half maximum (FWHM) in radians and θ is the Bragg's angle in radians.

3.3.2. Scanning electron microscopy (SEM) and Energy Dispersive X-ray spectroscopy (EDS)

SEM images were taken using Zeiss Crossbeam 540 operated at 2 kV for imaging and 20 kV for EDS. The EDS was obtained using an Oxford Xmax detector with Aztec software that was optimised with a copper reference.

3.3.3. Transmission electron microscopy (TEM)

TEM imaging was done using JEOL JEM 2100 at 200Kv. A very small quantity of the samples were dissolved in ethanol and sonicated for 30 minutes followed by a light dispersed on a carbon-coated copper grid and allowed to completely dry before use. ImageJ was used for image processing and analysis through a manual particle selection to determine the average particle size and coating thickness.

3.3.4. Fourier-transform infra-red spectroscopy (FT-IR)

FT-IR was analysed using a Bruker Tensor 27 operating with Opus 5.5 FT-IR. A background spectrum was first taken before taking the sample scans. The transmittance of the samples was measured at 400- 4000 cm^{-1}.

3.3.5. X-ray photoelectron spectroscopy (XPS)

XPS was analysed using Axis Supra^{+}, fitted with a 500 mm Rowland circle monochromated Al Kα X-ray source.

3.3.6. Brunauer Emett-Teller (BET)

The surface properties (pore size, pore volume, and surface area) of the material were determined by ASAP 2000 Micrometrics TriStar Surface Area and Porosity Analyser.

3.3.7. Thermogravimetric analysis (TGA)

TGA was conducted using a Perkin Elmer 6000. The sample weight was monitored from 35-900 ^{o}C at a heating rate of 10 ^{o}C/min under air gas at a flow rate of 20 ml/min.

3.4. Electrochemical analysis

3.4.1. Three electrode fabrication and configurations

All electrochemical measurements were conducted in an alkaline medium at ambient conditions, using VMP-300 Biologic with EC-Lab software. A standard 3-electrode configuration comprising of a platinum rod as a counter electrode, a rotating disk electrode (RDE, 5.0 mm) with a glassy carbon electrode substrate as a working electrode, and Ag/AgCl (saturated 3.0 M KCl) as a reference electrode. The RDE was polished with alumina (Al_2O_3) slurry and cleaned with acetone and ultra-pure water before further use. All the potentials were referred to a reversible hydrogen electrode (RHE) following the conversion formula equation 3.2.

$$\mathrm{E_{RHE}} = \mathrm{E_{Ag/AgCl}} + 0.197 + 0.059 \times \mathrm{pH} \quad (3.2)$$

where E_{RHE} and $E_{Ag/AgCl}$ are the converted potentials versus RHE and the experimental potential measured against the Ag/AgCl reference electrode, respectively, at pH = 13.42. All measurements made were conducted in a freshly prepared 1 M KOH solution.

A glassy carbon electrode (0.071 cm^2) was used for studies conducted in a ferrous-ferricyanide solution.

To prepare the ink for ORR and OER, the sample was dispersed in a 1:9 solution of water and isopropanol with Nafion and sonicated for 30 minutes. 20 µL of the ink was drop-casted on the polished RDE and dried in the air, yielding a loading of 0.4 ± 0.02 mg/cm^2. Cyclic voltammetry (CV) measurements were performed in N_2 or O_2 saturated 1.0 M KOH solution at a scan rate of 50 mV/s. To get the double-layer capacitance

(C_{dl}) value, CV curves with non-faradaic potential ranges were used. To measure ORR activity, linear sweep voltammograms (LSV) were collected at 10 mV/s in oxygen saturated 1.0 M KOH at rotation speeds of 400 to 2500 rpm and a scan, while OER was collected at 1600 rpm in 1.0 M KOH solution.

The number of transferred electrons during the ORR was determined by the Koutecky–Levich (K–L) in equations 2.23 recapped below:

$$\frac{1}{j} = \frac{1}{j_d} + \frac{1}{j_K} = \frac{1}{0.21nFD^{2/3}\gamma^{-1/6}Co_2\omega^{½}} + \frac{1}{nFkCo_2}$$

were j is the measured current, j_d is the diffusion-limiting current, j_k is the kinetic current, n is the number of electrons transferred, F is the Faraday constant, D is the diffusion coefficient (1.95 x 10^{-5} cm^2/s), γ is the kinematic viscosity (8.98 x 10^{-3} cm^2/s), C_{O_2} is the oxygen concentration (1.15 x 10^{-3} mol/dm^3), ω is the rotation speed in rpm, and k is the kinetic rate constant.

The kinetic current was calculated by the formula $j_k = (j_d * j)/(j_d - j)$, where j is the measured current at 0.75 V for ORR.

3.4.2. Two electrode fabrication and configurations

The aqueous and flexible batteries were measured using BioLogic BCS-8xx series operating on a BT-Lab program. The system was used to run CV, galvanostatic charge-discharge (GCD), and electrochemical impedance spectroscopy (EIS).

In an aqueous or parallel plate cell assembly, a mixture of CB and the active material at a ratio of 2.5:7.5 was used for the preparation of a cathode material. The RZAB was fabricated with a micro-3D printed cell that comprises of a polished zinc plate as an anode, a catalyst slurry on carbon paper, and a copper strip as a current collector. The slurry of the bifunctional air electrocatalysts was prepared by dispersing the electrocatalyst in a mixture of 9:1 isopropanol and water solution and sonicated for 30 minutes. PTFE (10:1 v/v%) solution was then added to the solution and further sonication for 30 minutes and moved to a stirring plate. After proper mixing, the slurry was then evenly spread on carbon paper to make the air cathode, followed by drying at 80 ^oC before cell assembly. The air electrode had a 2.0 mm perforated hole, where

O_2 from the air diffuses into the set-up. A solution of 6.0 M KOH and 0.2 M zinc acetate was used as the electrolyte.

The flexible zinc-air battery was fabricated by first preparing a solid-state electrolyte. The solid-state electrolyte was prepared by a previously prepared method [1]. Briefly, 2g of PVA was added to 20 mL of ultra-pure water and stirred from room temperature to 90 ^oC and reacted for 1 h. The transparent gel was then cooled to room temperature before adding a 2 mL solution of 6.0 M KOH and 0.2 M zinc acetate under stirring. The mixture was then poured into a flat petri dish and allowed to stand in a freezer for 4 h. The gel was then allowed to thaw at room temperature overnight. The solid-state electrolyte was cut to 0.5 cm^2 before assembly. The flexible cell assembly was set up by placing the cleaned nickel foam as a current collector, followed by carbon paper and electrocatalyst, then the PVA film was placed in the middle of a polished zinc plate and catalyst-loaded carbon paper (loading: 5 mg/cm^2) to form an all-solid zinc-air battery.

3.5. Reference

[1] J. Zhu, W. Tu, Z. Bai, H. Pan, P. Ji, H. Zhang, Z. Deng, H. Zhang, Zeolitic-imidazolate-framework-derived Co@Co_3O_4 embedded into iron, nitrogen, sulfur Co-doped reduced graphene oxide as efficient electrocatalysts for overall water splitting and zinc-air batteries, Electrochim Acta 323 (2019) 134821. doi.org/10.1016/j.electacta.2019.134821.

CHAPTER 4
CO ATOMIC CLUSTERS MOF-DERIVED CARBON FOR HIGH PERFORMANCE OXYGEN ELECTROCHEMISTRY AND RECHARGEABLE ZINC-AIR BATTERY

4.1. Introduction

Renewable energy conversion and storage devices are among the most promising technologies for sustainable and environmentally friendly energy generation and utilisation. MABs operating in alkaline electrolytes are promising candidates for rechargeable battery applications due to their low operation requirements and abundant catalyst choices. Amongst these devices, RZABs have drawn global attention because of their characteristics which include high theoretical energy output, operational safety, low cost, and most importantly its material balance due to the existence of an inexhaustible oxygen supply. This is an advantage over lithium-ion batteries which have an overbalanced cathode material to compensate for the first cycle loss of 5-20% of lithium and as a result a high initial irreversible capacity loss [1].

The electrochemical ORR and OER are the essential processes for the effective operation of the RZABs [2,3]. However, these reactions are well known for their extremely sluggish kinetics which leads to high potentials during the discharge and charge process limiting the extent of energy conversion in metal-air batteries [3]. Thus, effective and efficient electrocatalysts are necessary to drive these reactions. Platinum (Pt) group metals have been considered as the most common and efficient electrocatalysts for ORR and OER, but their high cost and scarcity, as well as activity failure and poor durability in alkaline media [4,5], manifested an interest in alternative electrocatalysts with characteristic low cost and abundance with no compromise on their performances in the energy storage and conversion systems [6].

Transition metal-based electrocatalysts have emerged as promising materials to replace the Pt group electrocatalysts for ORR and OER with several efforts made so far [7]. New and cost-effective electrode materials are expected to behave as bifunctional electrocatalysts, operating at high activity and stability and enabling

technology-level implementation. With this goal in mind, oxides [6], mixed oxides [8], single-atom catalysts [9], sulphides [10], chalcogenides [11], metal-organic frameworks (MOFs) [12], covalent-organic frameworks (COFs) [13], zeolitic imidazolate frameworks (ZIFs) [14], etc, of several low-cost transition metals have been considered. Periyaiah et al. [15] report MOFs as materials with unique structural advantages such, porous nature, large specific surface area with tuneable pores, electrical, and physiochemical properties, as well as adaptable chemistry, which make it the focus of research and development as bifunctional electrocatalysts for redox reactions. These materials comprise of metal coordination centers that bind to organic ligands, resulting in intricate, interconnected frameworks. The ardent characteristics of MOFs make them excellent sacrificial templates for preparing nanoporous transition metal-anchored MOF-derived carbons, inheriting the good properties of the parent materials [16]. However, the catalytic activity of conventional MOFs in oxygen reactions is typically restricted due to their insufficient active sites, slow mass transport, and low conductivity [17]. To improve its catalytic performance, a lot of work has been put into developing or optimising the structure of MOFs for beneficial electrocatalytic performances [18,19]. These techniques include increasing the surface area or oxygen vacancies, doping, introducing defects, and creating hybrid materials.

There are limited reports on the use of the MOF-derived carbons demonstrated as effective bifunctional electrocatalysts for ORR and OER in fabricated RZAB applications with impressive electrocatalytic performance [20,21]. Furthermore, there is no report on the use of acid-treated MOF as an electrocatalyst in RZAB. Acid treatment has been used to create defects over the surface of catalysts and to modify its micro-surface [22,23]. The surface defects help to improve the catalytic performance of the electrocatalysts. Jiang et al. investigated the influence of heat and post-acid treatment on the catalytic properties of MnO_2 [24]. They reported an enhanced reducibility of MnO_2 which created a higher mobility of oxygen species favourable for better catalytic activity. A similar observation was seen by Sun et al. [22] and Peng et al. [23]. In the work by Wang et al. [9], acid-treatment was used to remove the Co metal and SiO_2 to form single atoms catalyst (SAC) on micro and mesopores which were responsible for hosting active sites and providing pathways for reactant and product molecules.

In this research, a unique Co-based MOF was synthesised using a microwave-assisted method and employed as a sacrificial template for making Co-MOF-derived carbons, which are Co nanoparticles (Co NP@C_{BPDC}) and Co atomic clusters (Co AC@C_{BPDC}). Carbonising MOFs in an inert atmosphere can yield catalysts with some intrinsically good characteristics, such as highly concentrated active sites and well-organised frameworks with linked porous structures [12]. However, carbonisation at high temperatures tends to cause agglomeration of the metals, which affects the uniform distribution of metal and its active sites [25]. Thus, the Co NP was acid-treated to reduce the metals to their atomic clusters (Co AC). This increased the surface area of the material, as well as improved the chemisorption ability of the catalyst. The as-prepared materials were tested as electrocatalysts for ORR and OER, in alkaline medium. Furthermore, the same electrocatalyst was explored as bifunctional air electrocatalysts in RZAB applications for a parallel plate system and solid-state electrolyte. Under a parallel plate system, the battery was tested under deep cycling to assess the reversibility of zinc and its utilsation.

4.2. Experimental

4.2.1. Materials and reagents

The reagents used included ethanol, isopropanol, ultrapure water, 5% Nafion perfluorinated resin, ethylene glycol, acetone, zinc acetate, potassium hydroxide pellets, carbon black, cobalt nitrate hexahydrate, 4,4'-biphenyl dicarboxylic acid, hydrochloric acid, dimethylformamide, polytetrafluoroethylene, polyvinyl alcohol, carbon paper, copper strip, nickel foam and zinc plate

4.2.2. Physical characterisations

The crystalline structure, phase composition and purity, identification and quantification of the elements, nanoscopic imaging, and surface properties of Co NP@C_{BPDC} and Co AC@C_{BPDC} were thoroughly characterised using Powder X-ray diffraction (P-XRD), X-ray Photoelectron Spectroscopy (XPS), Transmission Electron Microscopy (TEM) and Brunauer–Emmett–Teller (BET).

4.2.3. Synthesis of Co nanoparticles (Co NP@C_{BPDC}) and Co atomic clusters (Co AC@C_{PBDC})

Co NP and Co AC were obtained through the sacrificial Co-MOF template by a previously established microwave-assisted solvothermal process [26], as schematically demonstrated (Scheme 4.1). Cobalt nitrate hexahydrate ($Co(NO_3)_2 \cdot 6H_2O$, 0.04 M) and 4,4'-biphenyldicarboxylic acid (BPDC, 0.02 M), were separately dissolved in a mixture of 1:1 ratio of solvent to surfactant, mixed and stirred for 2 h for uniform dispersion. This was followed by electromagnetic irradiation at 600 W and 150 °C for 40 min and cooled to room temperature. The rose purple precipitate obtained was centrifuged, washed with ethanol, and dried under vacuum at 60 °C. The Co NP@C_{BPDC} was prepared by carbonising the parent Co-based MOF sacrificial template under argon (Ar) flow at a constant rate (5 ^{o}C/min), while the Co AC@C_{BPDC} was made from the Co NP@C_{BPDC} by acid treatment.

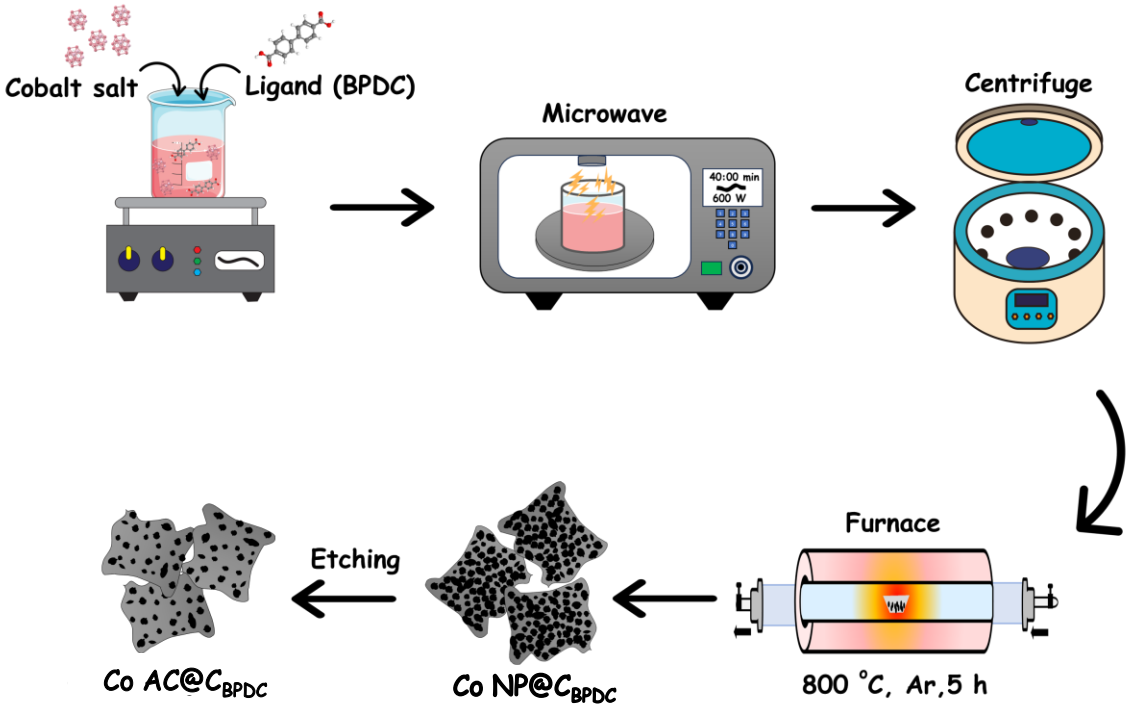

Scheme 4.1: The schematic synthesis diagram of Co NP@C_{BPDC} and Co AC@C_{BPDC}.

4.3. Results and discussion

4.3.1. Physical characterisation

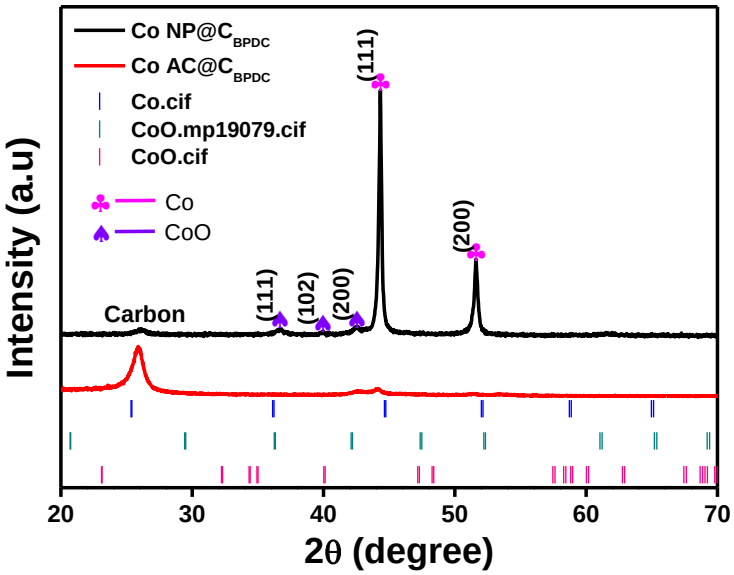

Figure 4.1: The powder XRD pattern of Co NP@C$_{BPDC}$ and Co AC@C$_{BPDC}$.

The XRD pattern of the materials was used to analyse the phase purity, lattice parameters, and crystalline structure of the material particles (Figure 4.1). The evidence of acid treatment was elucidated on the XRD profile of Co AC@C$_{BPDC}$ with an increased intensity of {002} facet at 2θ degree position of 25.9º and a slight shift to lower Bragg angles relative to Co NP@C$_{BPDC}$. This indicated a small increase in the interlayer spacing of Co AC@C$_{BPDC}$ that would enable more exposed active sites for rapid ion diffusion. The spectra of Co NP@C$_{BPDC}$ and Co AC@C$_{BPDC}$ were indexed to the crystallographic information file (CIF) of metallic Co and CoO. The metallic Co was represented by the dominant peaks observed particularly on Co NP@C$_{BPDC}$ at around 44.3º and 51.6º. This suggests that cobalt primarily exists as metallic Co with a face-centred cubic (fcc) in the Co@C$_{BPDC}$. Weak peaks at {111}, {102} and {200} were attributed to the trace amount of CoO. This indicated the coexistence of Co/CoO in Co@C$_{BPDC}$. A similar observation was reported by Juan and co-workers [27]. The cobalt was leached out of the inner layers of Co NP@C$_{BPDC}$ causing the formation of irregularities within the crystal which formed some defects in the lattice [28].

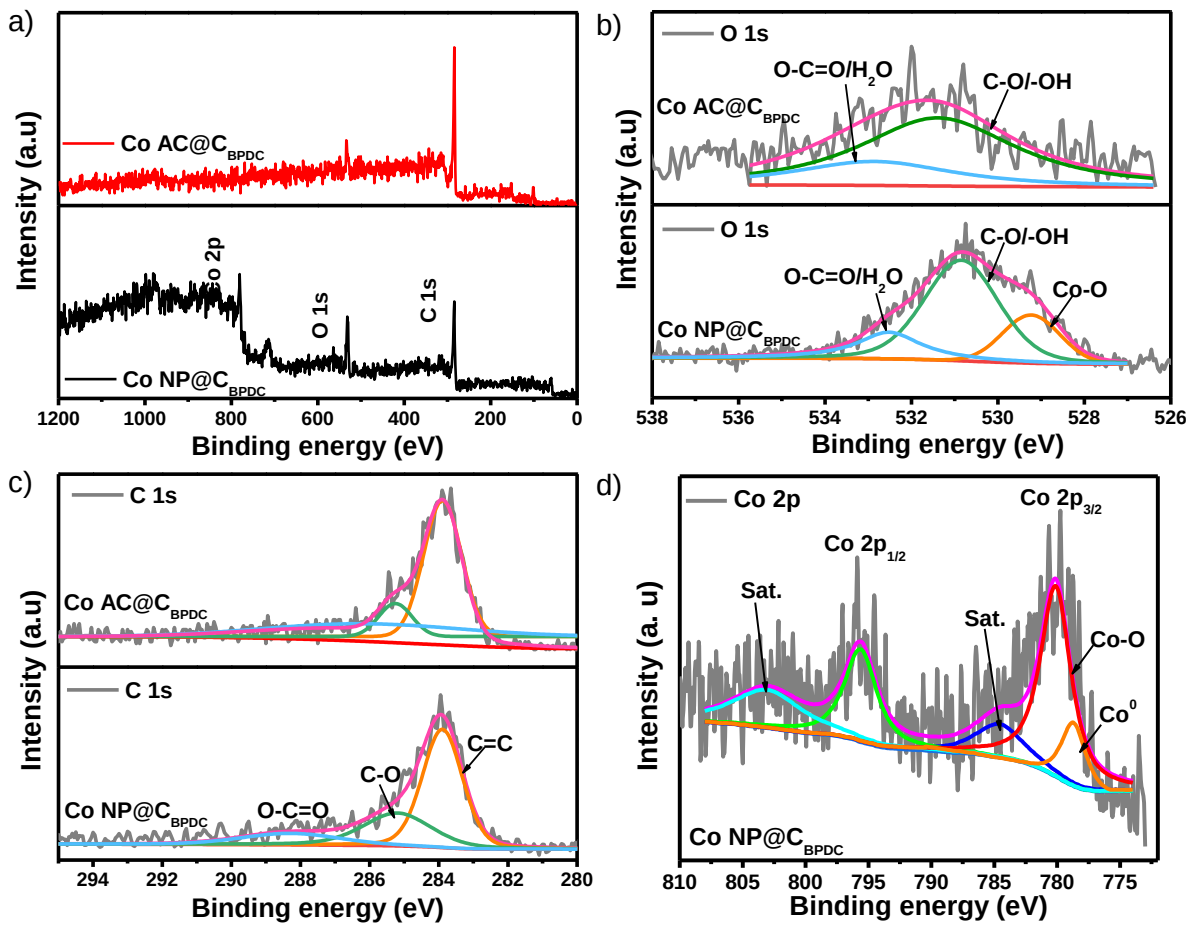

Figure 4.2: XPS survey spectra of (a) Co NP@C$_{BPDC}$ and Co AC@C$_{BPDC}$, (b) O 1s, (c) C 1s and (d) Co 2p spectrum of Co NP@C$_{BPDC}$.

XPS measurement was used to identify the active species and quantify the surface elemental composition. Figure 4.2a shows the survey scan spectra in the range of 0 eV to 1 200 eV confirming the presence of cobalt (Co 2p) and oxygen (O 1s) in the prepared composites, however, Co AC@C$_{BPDC}$ had no obvious Co 2p peak, but its presence was qualified by previously reported physical characterisation methods [26]. However, its absence may be due to the low metal concentration in the etched sample as a result of the detection limit of the XPS instrument used. The O 1s spectra in Figure 4.2b were fitted to two peaks for Co AC@C$_{BPDC}$ and three peaks for Co NP@C$_{BPDC}$. The peak at 529.3 eV observed in Co NP@C$_{BPDC}$ was due to the lattice oxygen which corresponded to the metal-oxygen bond of CoO. The peaks at 532.6 eV (Co NP@C$_{BPDC}$) and 532.9 eV (Co AC@C$_{BPDC}$) were due to O-C=O of the linker or chemisorbed species (H_2O) [29,30]. Located at the medium binding energy (Co NP@C$_{BPDC}$ = 530.9 eV; Co AC@C$_{BPDC}$ = 531.4 eV) was the hydroxyl species (-OH)

and carbon-oxygen bond (C-O). The area proportion of these bonds in Co AC@C_{BPDC} was calculated to be 80.1%, this was caused by the replacement of metal cations with hydroxyl ions. The carbon defects caused by the etching of Co in Co AC@C_{BPDC} will enable the absorption of more oxygen species than its parent material. Additionally, the pores will provide additional routes for mass transport, enabling them to reach the active sites more quickly and in larger amounts, enhancing the catalyst's overall efficiency. Pairing the excellent chemisorption ability of Co AC@C_{BPDC} to its reported high surface area and pore volume in Table 4.1 [26,31] will allow for enhanced electrochemical performance in comparison to its parent material. C1s was also deconvoluted to three peaks for both Co AC@C_{BPDC} and Co NP@C_{BPDC} (Figure 4.2c). The sp^2 peak at 284.0 eV was reported to be due to the presence of point defects that could arise from carbon vacancies and the hexagon rings [32]. Which was the dominant peak assigned to C=C in the benzene ring. While the peak at 285.3 eV was attributed to the carboxylic group O=C-O of BPDC and the peak at 288.3 eV was due to the C-O bond [33]. It was reported that the band originated from vacancy-like defects in the graphitic lattice [32]. The Co 2p region in Figure 4.2d was responsible for two main signals at 796.1 eV and 780.4 eV related to the core levels ascribed to Co $2p_{1/2}$ and Co $2p_{3/2}$, respectively. The Co $2p_{3/2}$ was deconvoluted to two peaks assigned to Co^0 (778.8 eV) and CoO (780.5 eV). Two shake-up satellite peaks corresponding to Co $2p_{1/2}$ (802.8 eV) and Co $2p_{3/2}$ (785.7 eV), were reported to suggest the presence of Co^{2+} bonded to oxygen [33].

Table 4.1: Nitrogen gas adsorption analysis of Co NP@C_{BPDC} and Co AC@C_{BPDC}.

Sample	Surface area (m^2/g)	Pore size (nm)	Pore volume (cm^3/g)
Co NP@C_{BPDC}	33.25	10.66	0.087
Co AC@C_{BPDC}	144.78	10.84	0.392

TEM was used to evaluate the effect of acid treatment on the surface of Co AC@C_{BPDC}. The micrographs show the pore structure and channels of the electrocatalysts. The micrographs reveal the presence of carbon around the metal nanoparticles. As seen in Figure 4.3a the mesopores of Co NP@C_{BPDC} were obscured by the catalyst, and upon acid treatment (Figure 4.3b) the pores were more exposed.

Treating Co AC@C_{BPDC} developed higher pore volume and surface area given in Table 4.1. This was caused by the removal of metal nanoparticles which resulted in increased pore volume as well as an increased surface area. A fair distribution of isolated atomic clusters across the carbon-derived surface could be observed and were depicted as isolated dark dots marked with orange circles. This proves the effective use of acid etching in the removal of metal nanoparticles. The porous network and fair catalyst distribution can optimise catalyst utilisation by ensuring the electrolyte can freely reach and interact with the catalyst's active sites.

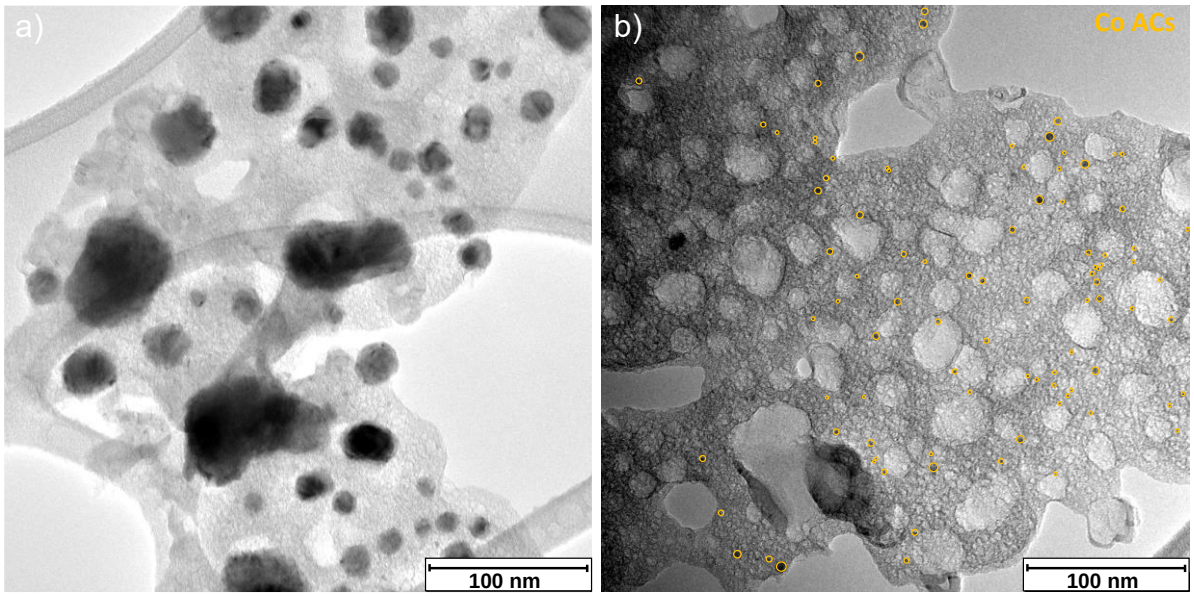

Figure 4.3: TEM images of (a) Co NP@C_{BPDC} and (b) Co AC@C_{BPDC}.

4.4. Electrochemical measurements

4.4.1. Oxygen reduction reaction (ORR)

The bifunctional electrocatalytic activity of the electrocatalysts was evaluated in 1 M KOH. The comparative cyclic voltammetry curves of Co NP@C_{BPDC} and Co AC@C_{BPDC} were measured under N_2 and O_2 saturated 1 M KOH solution at 50 mV/s (Figure 4.4a). Amongst the studied electrocatalysts in N_2 saturated supporting electrolyte, the Co AC@C_{BPDC} displayed a higher non-Faradaic or double-layer region, indicating that it had a better ability to store more charge in the supporting electrolyte compared to the Co NP@C_{BPDC}. This effect could be due to the etching that enabled high-density active sites created by highly-dispersed Co and CoO in Co AC@C_{BPDC} facilitating rapid transportation of the ions through its mesoporous surface. The

materials' charge storage efficiency was due to the observed variations in the microstructure orientation [34]. The result translated to increased capacitance of the etched material, due to its high specific surface area and increased pore volume with interconnected channels as revealed in Nitrogen Gas Adsorption analysis in Table 4.1, which provided more accessible sites for electrochemical reactions. In the O_2 saturated supporting electrolyte, there was a reduction of O_2 at a potential range of 0.70 V and 0.44 V where the Co AC@C_{BPDC} equally showed better O_2 reduction peak relative to the Co NP@C_{BPDC}. The poor electrical conductivity from Co NP@C_{BPDC} was the result of short active site density and agglomeration of the Co and CoO, which were unfavourable for efficient electrochemical processes. The addition of CB further improved the electrochemical response of Co AC@C_{BPDC}, evidenced by an increase in the capacitive response of Co AC@C_{BPDC}/CB (Figure 4.4b). This suggested a great improvement of catalytic activity from the CB contribution as a result of its high surface area and known good electrical conductivity which assisted electron movement during ORR. Also, the CB contributed immensely to the redox probe of the Co and CoO active sites in the composite (Co AC@C_{BPDC}/CB).

The ability of these materials to catalyse ORR was further studied by LSV. The electrochemical response of Co NP@C_{BPDC} was very poor compared to Co AC@C_{BPDC}. As observed in Figure 4.4c, the electrocatalyst with carbon black (Co AC@C_{BPDC}/CB) showed improved ORR kinetics with a more positive $E_{1/2}$ (0.66 V) and kinetic current density at 0.75 V (j_k@0.75 V = 0.26 mA/cm^2), compared to electrocatalyst without carbon (Co AC@C_{BPDC}; $E_{1/2}$ = 0.58 V, j_k@0.75 V = 0.06 mA/cm^2; Co NP@C_{BPDC}; $E_{1/2}$ = 0.55 V, j_k@0.75 V = 0.03 mA/cm^2). The onset potentials and current density along with Tafel slope (b_c) values (Figure 4.4d) of Co NP@C_{BPDC} (0.66 V; ~0.69 mA/cm^2; and 249.45 ± 4.67 mV/dec), Co AC@C_{BPDC} (0.76 V; ~2.91 mA/cm^2; and 142.17 ± 1.94 mV/dec) and Co AC@C_{BPDC}/CB (0.85 V; ~3.14 mA/cm^2; and 95.19 ± 0.66 mV/dec) followed a similar trend. Co AC@C_{BPDC}/CB exhibits more advantageous ORR kinetics, which is related to the acceleration of mass and electron transport.

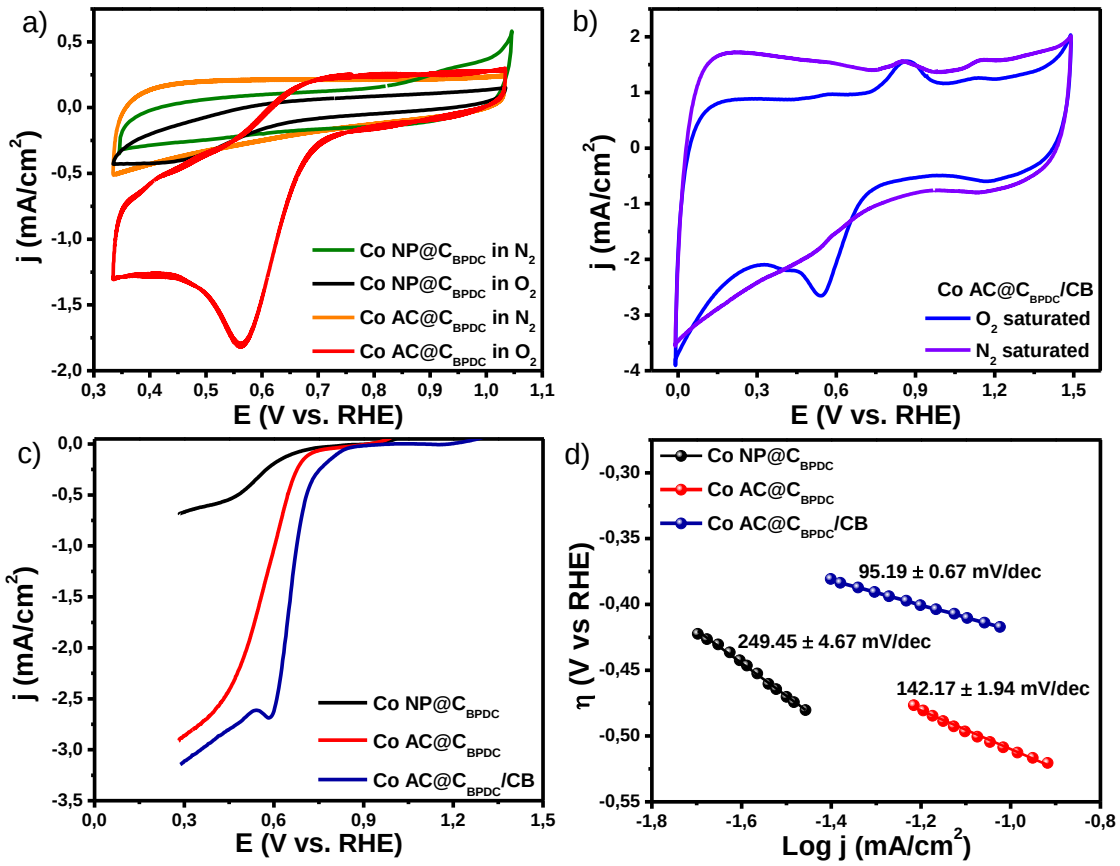

Figure 4.4: Cyclic voltammograms of (a) Co NP@C$_{BPDC}$ and Co AC@C$_{BPDC}$, (b) Co AC@C$_{BPDC}$/CB measured in 1.0 M KOH under N_2 and O_2 saturated solution at 50 mV/s, Co NP@C$_{BPDC}$, Co AC@C$_{BPDC}$ and Co AC@C$_{BPDC}$/CB (c) ORR polarisation curves at 1600 rpm at 10 mV/s and (d) corresponding Tafel plots.

The mass transport properties of the materials were investigated by running the ORR polarisation experiment at different rotation speeds. The ORR polarisation curves (Figure 4.5(a, c & e)) of the materials increased with increasing rotation speeds. The catalysts demonstrated mixed kinetic and diffusion-controlled currents and a clear mass transport-limited current plateau. Their shapes mirrored those of ORR polarisation curves seen in Pd–Ni nanoalloys [5], Pd_3Fe@Pt/C nanocatalysts [35], and FeCo@Fe/C core-shell nanocatalysts [36]. This phenomenon was often observed in porous electrodes where the oxygen diffusion depth within the electrode structure varies with applied potential [36]. This variation has been attributed to the use of either polymer or Nafion thin films in the ink preparation process [36]. Consequently, the plots were fitted to the conventional K-L equation (equation 2.23) [36], where the number of electrons involved and kinetic parameters during the ORR were

determined. The K-L plots for the electrocatalysts at different potentials are shown in Figure 4.5(b, d & f). The average number of electrons transferred for Co NP@C_{BPDC} was estimated to be 1.00 (Figure 4.5b), making it undesirable as an electrocatalyst for ORR. Hence, the use of CB in the ink preparation of Co NP@C_{BPDC} was not explored as the catalyst displayed very weak electrocatalytic activity. The estimated average number of electrons for Co AC@C_{BPDC} and Co AC@C_{BPDC}/CB were calculated to be 3.85 and 3.99 (Figure 4.5(d & f)), respectively. The electrocatalysts both obey the first-order kinetics and approximately a $4e^-$ pathway was obtained. During electrocatalysis, there was a fast and effective multi-electron reduction of molecular oxygen on Co AC@C_{BPDC}/CB [37]. This led to the direct formation of OH^- from O_2, thereby following the $4e^-$ ORR mechanism, as given in equation 4.1.

$$O_2 + H_2O + 4e^- \longrightarrow 4OH^- \quad (4.1)$$

The electron transfer rate constant (k) of the catalysts was calculated at the determined limiting current of 0.75 V using equations 2.24 and 2.25. k was determined to be 7.65×10^{-5} cm/s (Co NP@C_{BPDC}), 1.43×10^{-4} cm/s (Co AC@C_{BPDC}) and 6.44×10^{-4} cm/s (Co AC@C_{BPDC}/CB). Introducing CB proved to improve the rate constant of Co AC@C_{BPDC}/CB suggesting a faster electron transfer rate than Co AC@C_{BPDC}.

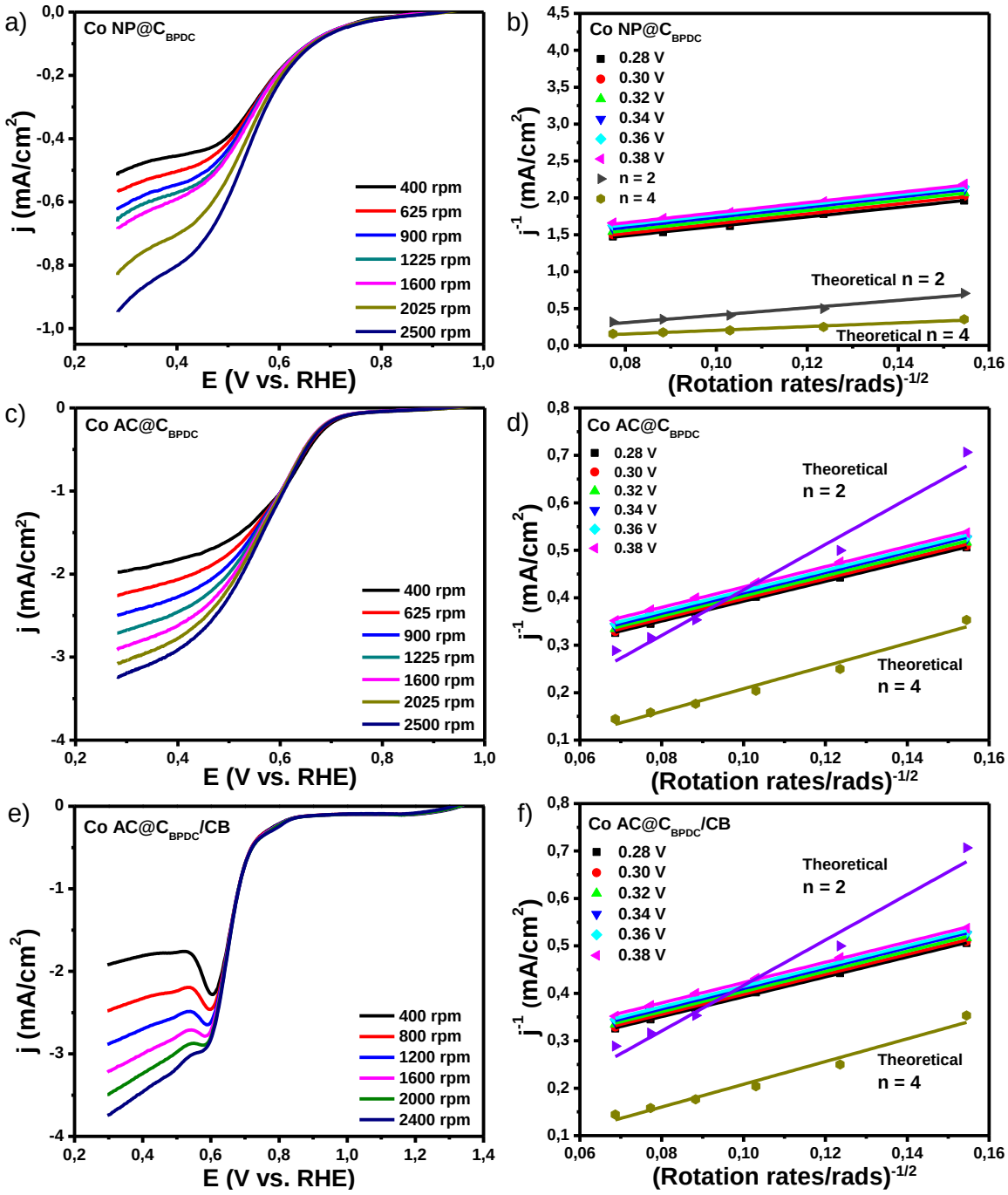

Figure 4.5: ORR polarisation curves at different rotation speeds for (a) Co NP@C_{BPDC}, (c) Co AC@C_{BPDC} and (e) Co AC@C_{BPDC}/CB and Koutecky-Levich (K-L) plots of (b) Co NP@C_{BPDC}, (d) Co AC@C_{BPDC} and (f) Co AC@C_{BPDC}/CB at varied potentials in O_2 saturated 1.0 M KOH.

Moreover, the stability of the electrocatalyst was evaluated for ORR. Figure 4.6, shows the LSV of Co AC@C_{BPDC}/CB before and after 5000 CV at an accelerated scan rate of 100 mV/s. An improved ORR curve after 5000 CV cycles was observed with $E_{1/2}$ at

0.71 V, implying that the composite (Co AC@C_{BPDC}/CB) became more activated after the accelerated 5000 CV scan, rather than slacken.

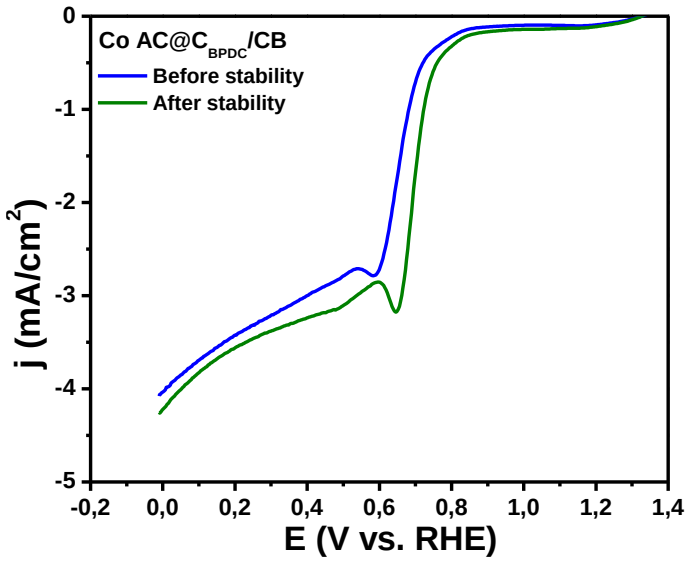

Figure 4.6: ORR polarisation curve variations of Co AC@C_{BPDC}/CB after stability at (10 mV/s; 1600 rpm).

4.4.2. Oxygen evolution reaction (OER)

Following the detailed characterisation, the OER catalytic activity of the electrocatalysts was investigated. The OER polarisation curves of the electrocatalysts at 1600 rpm showed similar onset potentials (1.52 V) for both Co AC@C_{BPDC} and Co AC@C_{BPDC}/CB (Figure 4.7a). That of Co NP@C_{BPDC} lacked behind at 1.62 V. This result revealed that the same energy is needed to catalyse OER by Co AC@C_{BPDC} and Co AC@C_{BPDC}/CB, while more energy is needed for catalysis of Co NP@C_{BPDC}. However, the addition of CB to Co AC@C_{BPDC} suppresses the production of O_2, evidenced by the increased overpotential at 10 mA/cm^2 (η_{10} = 400 mV), relative to Co AC@C_{BPDC} (370 mV). This was ascribed to the hydrophilic nature of carbon black which offered highly attractive adsorption sites for capturing oxygen and water and prevented their escape [38]. Hence, Co AC@C_{BPDC}/CB was not favourable for O_2 production. As seen in Figure 4.7b, Co AC@C_{BPDC} showed a lower Tafel slope of 62.58 $\pm$ 3.4 mV/dec, compared to Co AC@C_{BPDC}/CB (68.07 $\pm$ 4.6 mV/dec), demonstrating a more rapid OER catalytic kinetics of Co AC@C_{BPDC}. Co AC@C_{BPDC} also had a higher current density at 1.70 V of 42 mA/cm^2 compared to Co NP@C_{BPDC} (j@1.70 V = 13.43 mA/cm^2) and Co AC@C_{BPDC}/CB (j@1.70 V = 22.87 mA/cm^2). The

bifunctionality indicator ($\Delta E = E_{j10} - E_{1/2}$) indicated by the overall oxygen electrode curves in Figure 4.7c showed Co AC@C_{BPDC}/CB to have the smallest ΔE (0.96 V) value than Co AC@C_{BPDC} (ΔE = 1.05 V) and Co NP@C_{BPDC} (ΔE = 1.13 V). The BI responses of the catalysts were compared to 20wt% Pt/C for ORR and IrO_2 for OER, which showed a BI of 0.84 V. The improved bifunctional electrocatalytic response of Co AC@C_{BPDC}/CB was due to a combination of factors such as the presence of improved chemisorption ability, porosity and conductivity of CB, which facilitated the optimised adsorption and boosted the charge transfer kinetics of the electrocatalyst.

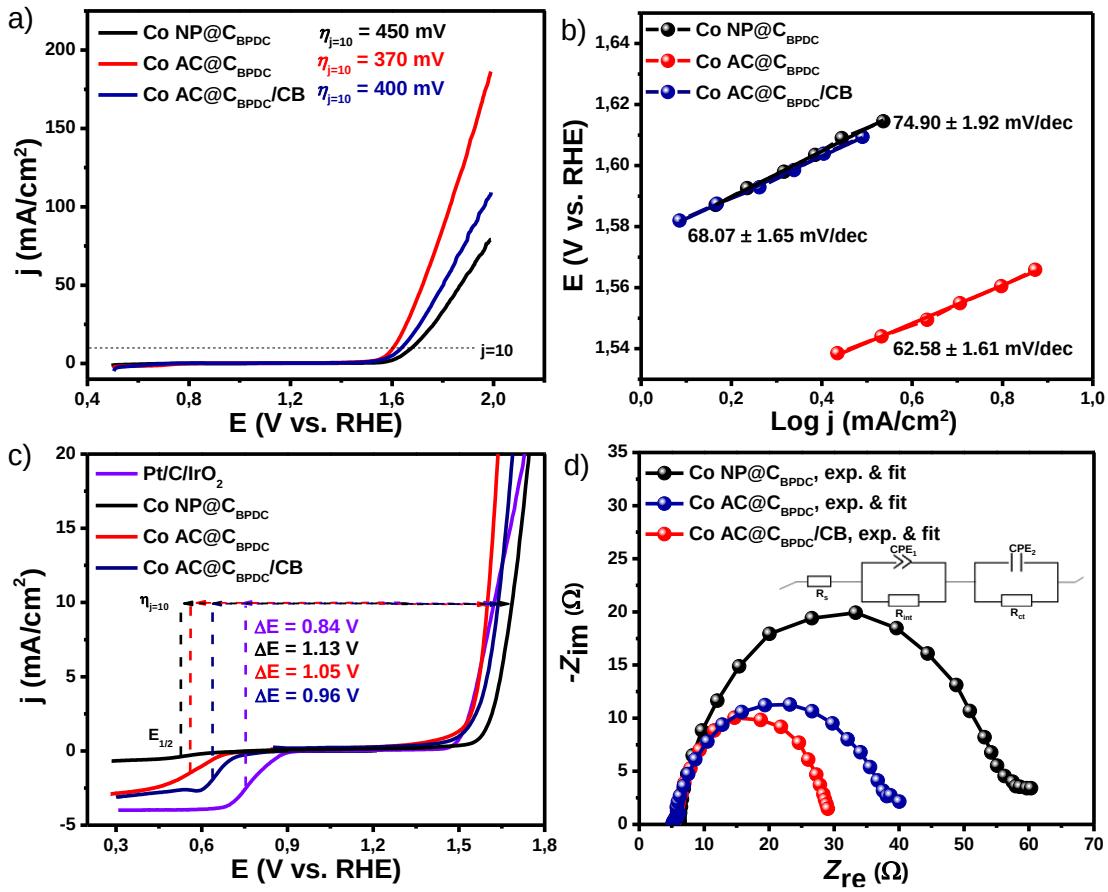

Figure 4.7: Co NP@C_{BPDC}, Co AC@C_{BPDC} and Co AC@C_{BPDC}/CB (a) OER polarisation curves, (b) Tafel plot, (c) ORR/OER polarisation curves compared to Pt/C/IrO_2, and (d) Nyquist plots for OER at respective η_{10} vs. RHE 1.0 M KOH at the scan rate of 10 mV/s at 1600 rpm.

The EIS technique was further used to probe the OER performance of the electrocatalysts. Nyquist plots of the electrocatalysts toward OER at 1600 rpm, 10 mV/s and respective η_{10} vs. RHE are shown in Figure 4.7d. An equivalent circuit was

used to analyse the impedance contribution from the faradaic process. The fitted results from the selected modelled Voigt EEC coincide well with the experimental data and were employed to extract the EIS parameters and summarised in Table 42. A complete semicircular loop was observed for all electrocatalysts under study, demonstrating that there was no mass transport limitation within the range of potentials investigated [39]. The diameter of the semicircle decreased as the potential required to drive the interfacial oxygen evolution reactions (OER) increased. Co NP@C_{BPDC}, Co AC@C_{BPDC} and Co AC@C_{BPDC}/CB recorded R_{ct} values of 46.29, 15.3 and 10.8 Ω, respectively. Co AC@C_{BPDC}/CB had the lowest R_{ct} value, which suggested a more effective electron transfer behaviour during OER compared to the other studied electrocatalysts. Thus Co AC@C_{BPDC}/CB was employed as an electrocatalyst for the RZAB application in the latter part of this work.

Table 4.2: EIS parameters for OER at respective η_{10} vs. RHE for the electrocatalysts.

EIS parameters	Co NP@C_{BPDC}	Co AC@C_{BPDC}	Co AC@C_{BPDC} /CB
R_s (Ω)	6.10 ± 0.44	5.32 ± 0.40	5.31 ± 0.07
R_{int} (Ω)	10.53 ± 1.60	9.31 ± 2.75	25.12 ± 0.77
CPE ($mF.s^{a-1}$)	0.87 ± 0.04	17.77 ± 0.13	6.22 ± 0.37
a	0.71	0.98	0.59
R_{ct} (Ω)	46.29 ± 5.77	15.32 ± 2.93	10.77 ± 0.57
C_{dl} (mF.s)	0.05 ± 0.02	2.46 ± 0.43	1.77 ± 0.12

4.5. Rechargeable zinc-air battery

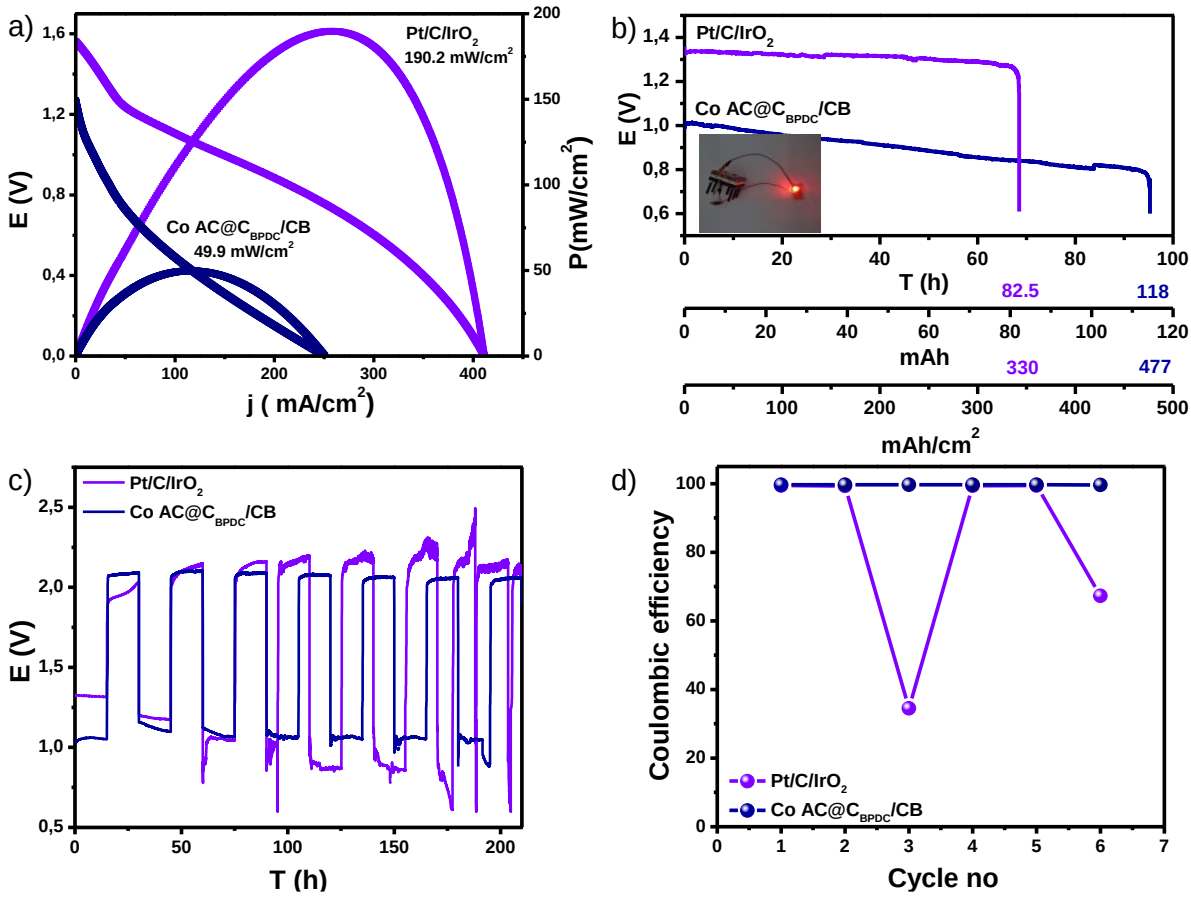

Figure 4.8: Co AC@C_{BPDC}/CB and Pt/C/IrO_2 (a) discharge polarisation and power density curves, (b) galvanostatic discharge curves at a fixed current density of 5 mA/cm^2 and a lit 1.6 V LED powered by Co AC@C_{BPDC}/CB, (c) GCD at 5 mA/cm^2 for 30 h per cycle and (d) Coulombic efficiency, conducted using 6.0 M KOH and 0.2 M zinc acetate electrolyte.

Based on the bifunctional electrochemical performance of Co AC@C_{BPDC}/CB, the material was used as an air cathode electrocatalyst to fabricate a rechargeable zinc-air battery (RZAB) in a parallel plate cell and a flexible zinc-air battery. Pt/C/IrO_2 was also studied for comparison. A parallel plate RZAB cell is resembled in Figure 2.2a. Here, the electrolyte flooded the chamber in the absence of a separator in which the anode and cathode were in no direct contact. As seen in Figure 4.8a, the OCV and maximum peak power density of Co AC@C_{BPDC}/CB were 1.23 V and 49.9 mW/cm^2, while that of Pt/C/IrO_2 was 1.56 V and 190.2 mW/cm^2, respectively. The Pt/C/IrO_2 presented a higher peak power density than Co AC@C_{BPDC}/CB, attributed to its high BI value. The battery was fully discharged to 0.6 V at 5 mA/cm^2 (Figure 4.8b), where

the areal energy reached 477 mAh/cm^2 for Co AC@C_{BPDC}/CB and 330 mAh/cm^2 for Pt/C/IrO_2. The catalyst underwent a 21.4% voltage loss at 0.80 V after 118 h of discharge where the discharge limitation of zinc was observed. To demonstrate the practicality of the catalyst, the Co AC@C_{BPDC}/CB was discharged on a 1.6 V LED (Figure 4.8b), and the bulb lit up with great brightness. This shows that the electrocatalyst can be used to power real-world devices.

The long-term stability of zinc-air battery is key when it comes to its application. Deep discharge-charge plateaus of Co AC@C_{BPDC}/CB and Pt/C/IrO_2 were conducted at 5.0 mA/cm^2 for multiple discharge charge cycles at 30 h per cycle as seen in Figure 4.8c. Deep cycling was used to allow an extended utilisation of zinc to assess its reversibility. The expanded hours of Co AC@C_{BPDC}/CB have a discharge-charge voltage gap of 1.03 V. Moreover, the battery could be repeatedly charged and discharged for 210 h with nearly constant discharge and charge plateaus. The plateaus of the charge-discharge represent the OER and ORR processes of the RZAB, respectively [40]. Pt/C/IrO_2 started with high discharge voltage recorded at 1.33 V, which decreased to 1.18 V (cycle 2), 1.05 V (cycle 3), 1.02 V (cycle 4), 0.86 V (cycle 5) and 0.87 V (cycle 6). The continued discharge/charge can cause the degradation of zinc and cause cell death upon its complete consumption. The zinc limitation effect in Co AC@C_{BPDC}/CB started to be noticeable at around 90 h (4th cycle) and that of Pt/C/IrO_2 was around 60 h (3rd cycle), which were reached at around the same time as that of the full cell discharge (Figure 4.8c). The battery's performance was compared to other reported literature and summarised in Table 4.3. The areal energy of Co AC@C_{BPDC}/CB performed above that of a Li-ion battery (35 mWh/cm^2) which is equivalent to a Li-ion pack of specific energy of 120 Wh/kg_{pack} [41]. Impressively, the Co AC@C_{BPDC}/CB did exceptionally well in terms of areal energy compared to most of the reported literature. The capacity of the RZABs with the Co AC@C_{BPDC}/CB was maintained throughout the cycling process with the charging and discharging voltages approximately constant. Its Coulombic efficiency was maintained at 99-100% for the cycles studied (Figure 4.8d). Due to the good OER/ORR electrocatalytic performance, stability, and practical application of Co AC@C_{BPDC}/CB, the electrocatalyst presents itself as a material to consider for real-time applications. At a DOD over 40%, it is easier to report the reversibility of the cell as all or most of the zinc is converted to ZnO which is then converted back to zinc [42]. Under low DOD, there is a large amount of

preserved zinc because of its partial oxidation at this stage. Thus, deep cycling represents a true cycle reversibility of zinc. Herein, DOD was calculated to be 51.3% (according to equation 2.41), which was above the minimum recommended DOD for deep cycling and practical battery demonstration capability.

The all-solid-state RZAB was assembled as shown in Figure 4.9a were a film electrolyte of 6 M KOH and 0.2 M zinc acetate and PVA was sandwiched by the zinc plate, coated carbon paper (coated with Co AC@C_{BPDC}/CB) and nickel foam. The flexible battery showed good discharge-charge performance at 5 mA/cm^2 which was maintained from 0 ^oC to 180 ^oC bending angles as seen in Figure 4.9b. The OCV of the battery was maintained at 1,73 V throughout all the bending angles (see Figure 4.9c). The battery's stability in Figure 4.9d was continued using the same battery and showed good stability. The stability test was stopped at 65 h operating time, totaling the set time to 70 h. The battery demonstrated excellent performance from bending stress to maintained performance of Co AC@C_{BPDC}/CB for a solid-state electrolyte configuration. This shows potential application in non-linear surfaces and flexible devices.

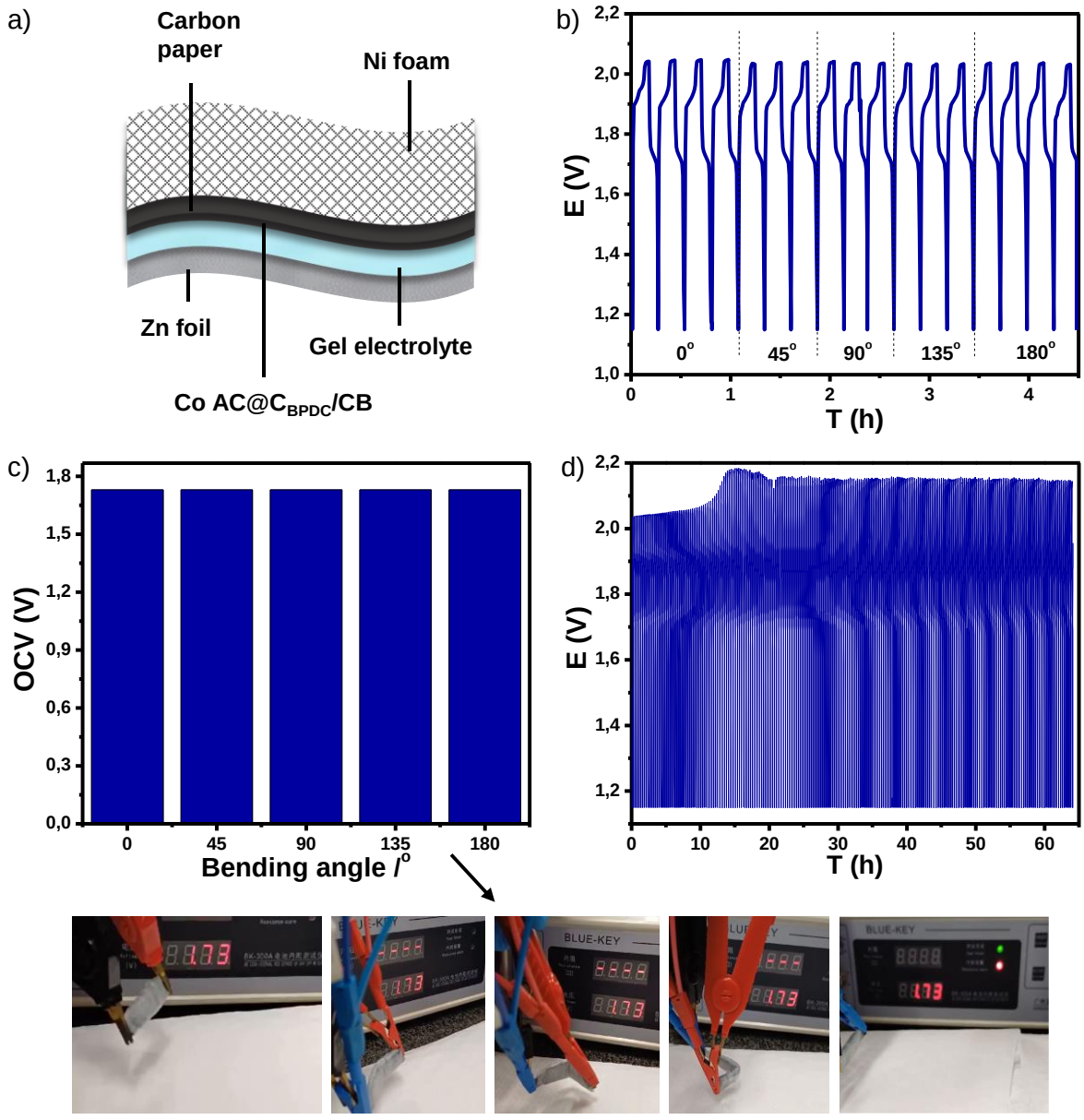

Figure 4.9: (a) A schematic illustration of a flexible solid zinc-air battery, (b) discharge-charge and (c) OCV at different bending angles, (d) cycling stability of Co AC@C_{BPDC}/CB at 5 mA/cm^2 at 10 minutes discharge charge times.

Table 4.3: Electrocatalytical comparison of two electrode rechargeable zinc-air batteries.

Catalyst	Current density (mA/cm^2)	Discharge time (h)	Areal Energy (mWh/cm^2)	Voltage gap ~ ΔE (V)	Stability	Reference
Co AC@C_{BPDC}/CB	5	15	**80.3**	1.00	210h (7 cycles)	This work
3DOM Co_3O_4	10	1	**12.4**	0.76	>400h (>200 cycles)	[6]
Bulk Co_3O_4	10	1	11.9	0.84	90 cycles	[6]
C–CoPAN900	1	0.5	0.63	0.70 to 0.78	>135h (135 cycles)	[43]
C–CoPAN900	2	25	63	0.90	250h (5 cycles)	[43]
C–CoPAN900 mat	2	0.5	1.3	0.70	160h (160 cycles)	[43]
C–CoPAN900 mat	20	0.5	11.9	0.85 to 0.94	55h (55 cycles)	[43]
Co_3O_4–C-NA	30	0.167	5.9	0.93 to 1.01	180 cycles	[44]
CNT- Co_3O_4/NC	15	0.167	3.3	0.70	50h (300 cycles)	[45]
MOF(Co)/C(3:1)-500	5	0.167	1.0	0.78 to 1.4	140h (420 cycles)	[46]
Ni-Co_3O_4/C-1	5	0.5	2.9	0.78	24 cycles	[47]
Co_3O_4@Co/NCNT	5	0.167	1.0	0.75 to 1.00	24h	[48]
ZIF-L-D- Co_3O_4/CC	5	0.167	1.2	0.75 to 0.83	384h	[49]
Fe-HPNC/ Co_3O_4 a	5	0.167	1.2	0.51 to 0.83	165h	[50]
Co_3O_4/NPGC	5	0.33	1.9	0.83	83h	[51]
Co_3O_4/Co@NCs b	10	0.083	1.1	0.89 to 0.94	600 h (3 600 cycles)	[52]
Co_3O_4/MnO_2-CNTs	10	0.083	0.83	1.00	198h	[53]
Co_3O_4/MnO_2-CNTs	100	4	**240**	1.00	20h	[53]

Co_3O_4/ Mn_3O_4/CN_x@CNFs	5	0.167	0.8	1.16	60h	[54]
Co_3O_4/WS_2	5	0.167	1.0	0.75	16h	[11]
$(Co,Fe)_3N$_R	30	1	**33**	0.85	300h	[55]
$(Co,Fe)_3N$_R	5	10	**57.5**	0.64	750h	[55]
NS@Co_3-x$NixO_4$/ Co_3O_4	20	0.5	10.5	0.90 to 0.85	90h	[56]
SS@Co_3O_4	20	0.5	10	0.93 to 0.91	90h	[56]
NF@$Co_{3-x}Ni_xO_4$	20	0.5	11	0.95 to 0.97	90h	[56]
$Mn_{0.25}$-Co_3O_4/CNTs	5	0.167	0.8	1.58	102h	[57]
Co_3O_4-NP/N-rGO	5	0.056	0.4	0.76 to 0.87	160h (1 600 cycles)	[58]
3D-Co@Co-NPC	5	0.083	0.5	0.80 to 0.83	90h (550 cycles)	[59]
CoO/N-CNT + NiFe LDH	50	2	**120**	0.85	40h (10 cycles)	[60]
CoO/N-CNT + NiFe LDH	20	10	**250**	0.70	200h (10 cycles)	[60]
Co_3O_4/CB	10	10	**100**	1.06 to 2.10	80h (4 cycles)	[61]
MCO/CNFs@NC	5	0.25	1.5	0.83 to 0.85	112 h (224 cycles)	[62]
NGM-Co	2	0.33	2	1.12 to 1.15	180 cycles	[63]
$CoWO_4$/WS_2@C-N		0.125	1,7	0.54 to 0.60	90h	[64]
Co_3O_4 NWs grown on SS mesh	17.6	3	**52.8**	1.00	600h	[65]
5% Co-doped TiO_2	5	10	**62.5**	0.81	130h (6 cycles)	[66]
Co-N_4/NC	10	3	**30**	1.16 to 1.47	20h (100 cycles)	[67]
Co–Nx/C NRA	50	2	111	0.90	80h (20 cycles)	[68]
S-N-C 900	5	0.33	2	0.84	600h (1800 cycles)	[69]
$MnCo_2O_4$-300	3	0.33	1.11	1.09	16h	[8]
$MnCo_2O_4$-600	3	0.33	1.04	1.16	72.2h (110 cycles)	[8]
LBC-15	10	0.167	1.83	0.95 to 0.98	200h (1200 cycles)	[70]
Co@Co_3O_4/FeNS-RGO	5	0.11	0.61	0.91 to 1.2	40h (360 cycles)	[71]
CoP/Co_3O_4-fC-pPVP	5	0.083	0.5	0.80	727h	[72]
Co_3O_4/carbon cloth electrode (PTFE-2)	10	0.33	0.31	1.074 to 1.106	400 cycles	[73]

Co_3O_4/Ni/GDL1	10	0.0694	0.833	0.69 to 0.78 to 0.76	425h	[74]
Co_3O_4/Ni/GDL1	20	0.083	2	0.80	37,5h (275 cycles)	[74]
40% Mn-Co_3O_4@CNTs	10	0.33	3.93	0.94	425h (1275 cycles)	[75]
Co@N-PCNF-1.0	5	0.25	1.475	0.92 to 1.05	200h	[76]
CNTs@(Fe,Co,Ni)PP-800	2	0.167	0.492	0.70 to 0.78	50h (300 cycles)	[77]
CoS_2(400)/N,S-GO	10	0.0	1	0.78	200h (70 cycles)	[10]
$La_{0.8}Sr_{0.2}CoO_3$	10	0.167	1.83	0.64 to 0.80	16h (100 cycles)	[78]
CoNi-CoO@NC/CP	5	0.167	0.983	0.85	50h (156 cycles)	[79]
MoCoZn/NCNTA	5	0.167	0.92	-	130h (780 cycles)	[80]
$NiCo_2S_4$/$RGO_{0.02}$	5	0.33	0.167	0.82	35h (210 cycles)	[81]
CoO@NC	5	0.167	0.917	0.75 to 0.81	200h (600 cycles)	[82]
Co_3O_{4-x}@C/Ni Foam (3 min)	10	0.25	3	0.87 to 0.85	358h (716 cycles)	[40]
P-CoNi@NSCs	5	0.167	1	0.87	620h (1860 cycles)	[83]
P-CoNi@NSCs	10	0.167	14	0.82	430h (1290 cycles)	[83]
Co_3O_4-S/NSG	10	0.083	0.913	1.00 to 1.34	4000 cycles	[84]
Co–B–O/NPC-50%	2	0.083	0.2	1.05	60h	[85]
$NiCo_2S_4$/$CNNs_{-1}$	10	0.083	1.04	0.69 to 0.72	180h (1000 cycles)	[86]
CoS_x/PBMF	10	0.1	1.1	0.83 to 0.86	220h (1100 cycles)	[87]
Co-N-C SAC	5	0.33	1.97	0.78	54 cycles	[9]

4.6. Conclusions

This work investigated the effect of acid treatment on the preparation of cobalt-MOF-derived carbon (Co@C_{BPDC}) for oxygen electrochemistry (ORR and OER) and air cathode in aqueous and all-solid-state RZABs. The newly synthesised Co AC@C_{BPDC} was endowed with intrinsic physicochemical merits, i.e., more available active sites, higher pore volume, and specific surface area, than its untreated counterpart (Co NP@C_{BPDC}), which were beneficial for its boosted oxygen electrochemistry. This was proved by the improved $E_{1/2}$, E_{onset}, η_{10}, ΔE and j_k of Co AC@C_{BPDC}, due to the robust Co/CoO active sites. The addition of CB to Co AC@C_{BPDC} further augmented the O_2 redox couple with lower ΔE, owing to the increased electrical conductivity of Co AC@C_{BPDC}/CB relative to Co AC@C_{BPDC}, proved by the EIS analysis. Hence, Co AC@C_{BPDC}/CB was utilised as an air cathode for the proof-of-concept in rechargeable aqueous (parallel plate or flooded cell) and all-solid-state Zn-air batteries. In the parallel plate RZAB, the Co AC@C_{BPDC}/CB exhibited impressive OCV (1.23 V), peak power density (49.9 mW cm^{-2}), areal energy density (477 mAh/cm^2), and long-term stability for 210 h, as well as retained its equilibrium voltage retention, Coulombic efficiency (ca. 100 %) and DOD (51.3%), which were comparable to the literature. The real-life practicality of the fabricated parallel plate RZAB was explored by lighting a 1.6 V bulb with excellent brightness. The all-solid-state RZAB gave a constant OCV (1.73 V) at varied bending angles (0 – 180 ^oC) and achieved excellent stability at 180 ^oC. This research showed the versatility of acid-treated MOF-derived carbon derivatives as highly active electrode materials for energy storage and conversion devices.

4.7. References

[1] Y. Sun, H.-W. Lee, Z.W. Seh, N. Liu, J. Sun, Y. Li, Y. Cui, High-capacity battery cathode prelithiation to offset initial lithium loss, Nat Energy 1 (2016) 15008. doi.org/10.1038/nenergy.2015.

[2] P. Anand, M. Wong, Y. Fu, Perovskite oxide composites for bifunctional oxygen electrocatalytic activity and zinc-air battery application- A mini-review, Energy Storage Mater 58 (2023) 362–380. doi.org/10.1016/j.ensm.2023.03.033.

[3] A.K. Ipadeola, A.B. Haruna, L. Gaolatlhe, A.K. Lebechi, J. Meng, Q. Pang, K. Eid, A.M. Abdullah, K.I. Ozoemena, Efforts at enhancing bifunctional electrocatalysis

and related events for rechargeable zinc-air batteries, ChemElectroChem 8 (2021) 3998–4018. doi.org/10.1002/celc.202100574.

[4] K.I. Ozoemena, Alkaline direct alcohol fuel cells: catalyst design, principles and applications, RSC Adv 6 (2016) 89523-89550. doi.org/10.1039/c6ra15057h.

[5] A.K. Ipadeola, P. V Mwonga, K.I. Ozoemena, Hydrogen oxidation and oxygen reduction reactions on palladium nano-electrocatalyst supported on nickel-deficient MOF-derived carbons, Electrochim Acta 390 (2021) 138860. doi.org/10.1016/j.electacta.2021.138860.

[6] M.G. Park, D.U. Lee, M.H. Seo, Z. Paul, Z. Chen, 3D ordered mesoporous bifunctional oxygen catalyst for electrically rechargeable zinc-air batteries, Small 12 (2016) 2707–2714. doi.org/10.1002/smll.201600051.

[7] A.B. Haruna, K.I. Ozoemena, Manganese-based bifunctional electrocatalysts for zinc-air batteries, Curr Opin Electrochem 21 (2020) 219–224. doi.org/10.1016/j.coelec.2020.02.021.

[8] M. Karimpour, M. Dorri, A. Babaei, C. Zamani, M. Soleimani, M. Pourfath, New insights on the effects of surface facets and calcination temperature on electrochemical properties of $MnCo_2O_4$ as bifunctional oxygen electrocatalyst in zinc-air batteries, Electrochim Acta 467 (2023) 143022. doi.org/10.1016/j.electacta.2023.143022.

[9] L. Wang, Z. Xu, T. Peng, M. Liu, L. Zhang, J. Zhang, Bifunctional single-atom cobalt electrocatalysts with dense active sites prepared via a silica xerogel strategy for rechargeable zinc-air batteries, Nanomaterials 12 (2022) 381. doi.org/10.3390/nano12030381.

[10] P. Ganesan, P. Ramakrishnan, M. Prabu, S. Shanmugam, Nitrogen and sulfur Co-doped graphene supported cobalt sulfide nanoparticles as an efficient air cathode for zinc-air battery, Electrochim Acta 183 (2015) 63–69. doi.org/10.1016/j.electacta.2015.05.182.

[11] Y. Ling, M. Li, K. Qu, Z. Yang, Electronically interacted Co_3O_4/WS_2 as superior oxygen electrode for rechargeable zinc–air batteries, Chem. Commun. 56 (2020) 15193–15196. doi.org/10.1039/d0cc07319a.

[12] Y. Zhou, B. Tang, S. Wang, J. Long, Cu-MOF@Co-MOF derived Co-Cu alloy nanoparticles and N atoms co-doped carbon matrix as efficient catalyst for enhanced oxygen reduction, Int J Hydrogen Energy 45 (2020) 15785–15795. doi.org/10.1016/j.ijhydene.2020.04.049.

[13] J. Ji, C. Zhang, S. Qin, P. Jin, First-principles investigation of two-dimensional covalent–organic framework electrocatalysts for oxygen evolution/reduction and hydrogen evolution reactions, Sustain Energy Fuels 5 (2021) 5615–5626. doi.org/10.1039/D1SE01257F.

[14] L. Zhou, P. Zhou, Y. Zhang, B. Liu, P. Gao, S. Guo, 3D star-like atypical hybrid MOF derived single-atom catalyst boosts oxygen reduction catalysis, Journal of Energy Chemistry 55 (2021) 355–360. doi.org/10.1016/j.jechem.2020.06.059.

[15] I. Periyaiah, M.P. Kumar, N. Kumaresan, R.V. Mangalaraja, F.V.H. Diaz, S.F. Sahlevani, S. Sasikala, G. Murugadoss, I. Perumal, M. Sasikumar, Facile synthesis of Co-Cu metal organic framework as efficient non-noble bifunctional electrocatalysts for overall water splitting, Applied Surface Science Advances 21 (2024) 100593. doi.org/10.1016/j.apsadv.2024.100593.

[16] M. Zhou, H. Wang, S. Guo, Towards high-efficiency nanoelectrocatalysts for oxygen reduction through engineering advanced carbon nanomaterials, Chem Soc Rev 45 (2015) 1273–1307. https://doi.org/10.1039/c5cs00414d.

[17] J. Zhang, C. Zhang, X. Duo, Z. Liu, C. Liu, L. Guo, A. Xie, S. Luo, Self-assembled acicular CuCo-MOF for enhancing oxygen evolution reaction, Ionics 26 (2020) 5123–5132. doi.org/10.1007/s11581-020-03651-0.

[18] A.K. Ipadeola, R. Barik, S.C. Ray, K.I. Ozoemena, Bimetallic Pd/SnO_2 Nanoparticles on metal organic framework (MOF)-derived carbon as electrocatalysts for ethanol oxidation, Electrocatalysis 10 (2019) 366–380. doi.org/ 10.1007/s12678-019-00518-5.

[19] W. Yang, X. Li, Y. Li, R. Zhu, H. Pang, Applications of metal-organic-framework-derived carbon materials, Advanced Materials 31 (2019) 1804740. doi.org/10.1002/adma.201804740.

[20] A. Adhikari, K. Chhetri, R. Rai, D. Acharya, J. Kunwar, M.R. Kandel, (Fe-Co-Ni-Zn)-based metal-organic framework-derived electrocatalyst for zinc-air batteries, Nanomaterials 13 (2023) 2612. doi.org/10.3390/nano13182612.

[21] S. Agarwal, X. Yu, A. Manthiram, A pair of metal organic framework (MOF)-derived oxygen reduction reaction (ORR) and oxygen evolution reaction (OER) catalysts for zinc-air batteries, Mater Today Energy 16 (2020) 100405. https://doi.org/10.1016/j.mtener.2020.100405.

[22] M. Sun, B. Zhang, H. Liu, B. He, F. Ye, L. Yu, C. Sun, H. Wen, The effect of acid/alkali treatment on the catalytic combustion activity of manganese oxide octahedral molecular sieves, RSC Adv 7 (2017) 3958–3965. doi.org/10.1039/C6RA27700d.

[23] Y. Peng, W. Si, J. Luo, W. Su, H. Chang, J. Li, J. Hao, J. Crittenden, Surface tuning of $La_{0.5}Sr_{0.5}CoO_3$ perovskite catalysts by acetic acid for NO_x storage and reduction, Environ Sci Technol 50 (2016) 6442-6448. doi.org/10.1021/acs.est.6b00110.

[24] Y. Jiang, G. Cheng, R. Yang, H. Liu, M. Sun, L. Yu, Z. Hao, Influence of preparation temperature and acid treatment on the catalytic activity of MnO_2, J Solid State Chem 272 (2019) 173-181. doi.org/10.1016/j.jssc.2019.01.031.

[25] D. Kim, I. Jang, Y. Sohn, E. Joo, C. Jung, N.D. Kim, J.Y. Jung, V.K. Paidi, K. Lee, P. Kim, S.J. Yoo, Effect of posttreatment on the catalytic performances of Fe-N-C for oxygen reduction reactions, Int J Energy Res 2023 (2023) Article ID 3265915. doi.org/10.1155/2023/3265915.

[26] L. Gaolatlhe, R. Barik, S.C. Ray, K.I. Ozoemena, Voltammetric responses of porous Co_3O_4 spinels supported on MOF-derived carbons: Effects of porous volume on dopamine diffusion processes, Journal of Electroanalytical Chemistry 872 (2020) 113863. doi.org/10.1016/j.jelechem.2020.113863.

[27] X. Yuan, X.-X. Hu, X.-L. Ding, H.-C. Kong, H.-D. Sha, H. Lin, W. Wen, G. Shen, Z. Guo, Z.-F. Ma, Y. Yang, Effects of cobalt precursor on pyrolyzed carbon-supported cobalt-polypyrrole as electrocatalyst toward oxygen reduction reaction, Nanoscale Res Lett 8 (2013) 478. doi.org/10.1186/1556-276X-8-478.

[28] S.L.S. J. Ouyang, D. Mu, Y. Zhang, H. Yang, Selective Fabrication of Barium Carbonate Nanoparticles in the Lumen of Halloysite Nanotubes, Minerals 8 (2018) 296. doi.org/10.3390/min8070296.

[29] Y. Liu, C. Wang, S. Ju, M. Li, A. Yuan, G. Zhu, FeCo-based hybrid MOF derived active species for effective oxygen evolution, Progress in Natural Science: Materials International 30 (2020) 185–191. doi.org/10.1016/j.pnsc.2020.02.006.

[30] Z. Liu, J. Xu, F. Zhang, L. Ji, Z. Shi, Defect-rich high-entropy oxide nanospheres anchored on high-entropy MOF nanosheets for oxygen evolution reaction, Int J Hydrogen Energy 48 (2023) 14622–14632. doi.org/10.1016/j.ijhydene.2022.12.333.

[31] K. Li, X. Yang, J. Gao, Y. Guo, Y. Wang, Y. Zou, Z. Li, Z. Lü, Modulation of perovskite electronic configuration by cobalt doping for efficient catalysts in zinc-air battery electrodes, Chemical Engineering Journal 475 (2023) 146301. doi.org/10.1016/j.cej.2023.146301.

[32] K. Ganesan, S. Ghosh, N. Gopala Krishna, S. Ilango, M. Kamruddin, A.K. Tyagi, A comparative study on defect estimation using XPS and Raman spectroscopy in few layer nanographitic structures, Physical Chemistry Chemical Physics 18 (2016) 22160–22167. doi.org/10.1039/C6CP02033J.

[33] S. Xie, F. Li, S. Xu, J. Li, W. Zeng, Cobalt/iron bimetal-organic frameworks as efficient electrocatalysts for the oxygen evolution reaction, Chinese Journal of Catalysis 40 (2019) 1205–1211. doi.org/10.1016/S1872-2067(19)63384-x.

[34] R.B. Rakhi, W. Chen, D. Cha, H.N. Alshareef, Substrate dependent self-organization of mesoporous cobalt oxide nanowires with remarkable pseudocapacitance, Nano Lett 12 (2012) 2559–2567. doi.org/10.1021/nl300779a.

[35] W. Wang, R. Wang, S. Ji, H. Feng, H. Wang, Z. Lei, Pt overgrowth on carbon supported PdFe seeds in the preparation of core-shell electrocatalysts for the oxygen reduction reaction, J Power Sources 195 (2010) 3498–3503. doi.org/10.1016/j.jpowsour.2009.12.015.

[36] O.O. Fashedemi, K.I. Ozoemena, Enhanced methanol oxidation and oxygen reduction reactions on palladium-decorated FeCo@Fe/C core-shell nanocatalysts in

alkaline medium, Physical Chemistry Chemical Physics 15 (2013) 20982–20991. doi.org/10.1039/c3cp52601a.

[37] H. Zhong, Y. Luo, S. He, P. Tang, D. Li, N. Alonso-vante, Y. Feng, Electrocatalytic cobalt nanoparticles interacting with nitrogen-doped carbon nanotube in-situ generated from a metal-organic framework for the oxygen reduction reaction, ACS Appl Mater Interfaces 9 (2016) 2541-2549. doi.org/10.1021/acsami.6b14942.

[38] D. Argyris, N.R. Tummala, A. Striolo, D.R. Cole, Molecular structure and dynamics in thin water films at the silica and graphite surfaces, The Journal of Physical Chemistry C 112 (2008) 13587–13599. doi.org/10.1021/jp803234a.

[39] X-Z. Yuan, C. Song, H. Wang, J. Zhan, Electrochemical Impedance Spectroscopy in PEM Fuel Cells: Fundamentals and applications, Springer, 2010: pp. 193–262. doi.org/10.1007/978-1-84882-846-9.

[40] D. Chen, L. Pan, P. Pei, S. Huang, P. Ren, X. Song, Carbon-coated oxygen vacancies-rich Co_3O_4 nanoarrays grow on nickel foam as efficient bifunctional electrocatalysts for rechargeable zinc-air batteries, Energy 224 (2021) 120142. doi.org/10.1016/j.energy.2021.120142.

[41] B.J. Hopkins, C.N. Chervin, J.F. Parker, J.W. Long, D.R. Rolison, An areal-energy standard to validate air breathing electrodes for rechargeable zinc-air batteries, Adv Energy Mater 10 (2020) 2001287. doi.org/10.1002/aenm.202001287.

[42] D. Deckenbach, J.J. Schneider, A long-overlooked pitfall in rechargeable zinc–air batteries: proper electrode balancing, Adv Mater Interfaces 10 (2023) 2202494. doi.org/10.1002/admi.202202494.

[43] Y.Z. B. Li, X. Ge, F. T. Goh, T. A. Hor, D. Geng, G. Du, Z. Liu, J. Zhang, X. Liu, Co_3O_4 nanoparticles decorated carbon nanofiber mat as binder-free air cathode for high performance rechargeable zinc-air batteries, Nanoscale 7 (2015) 1830-1838. doi.org/10.1039/b000000x.

[44] J. Ren, G. Yuan, C. Weng, Z. Yuan, Rationally designed Co_3O_4−C nanowire arrays on Ni foam derived from metal-organic framework as reversible oxygen evolution electrodes with enhanced performance for Zn−air batteries, ACS Sustain Chem Eng 6 (2018) 707–718. doi.org/10.1021/acssuschemeng.7b03034.

[45] C. Wang, K. Hung, T. Ko, S. Hosseini, Y. Li, Carbon-nanotube-grafted and nano-Co_3O_4-doped porous carbon derived from metal-organic framework as an excellent bifunctional catalyst for zinc-air battery, J Power Sources 452 (2020) 227841. doi.org/10.1016/j.jpowsour.2020.227841.

[46] X. Yi, X. He, F. Yin, B. Chen, G. Li, Co-CoO-Co_3O_4/N-doped carbon derived from metal-organic framework: The addition of carbon black for boosting oxygen electrocatalysis and Zn-air battery, Electrochim Acta 295 (2019) 966–977. doi.org/10.1016/j.electacta.2018.11.142.

[47] X.L. Yue Zheng, Li Huang, Rui Gao, Lirong Zheng, Zhongbo Hu, Boosting oxygen reduction activity of Co_3O_4 through a synergy of Ni-doping and carbon species dotting for Zn-air battery, J Electrochem Soc 170 (2023) 060532. doi.org/10.1149/1945-7111/acdd9f.

[48] T. Singh, C. Das, N. Bothra, N. Sikdar, S. Das, S.K. Pati, T.K. Maji, MOF derived Co_3O_4@Co/NCNT nanocomposite for electrochemical hydrogen evolution, Flexible zinc-air batteries, and overall water splitting, Inorg Chem 49 (2020) 3160–3170. doi.org/10.1021/acs.inorgchem.9b03516.

[49] Y. Zhong, Z. Pan, X. Wang, J. Yang, Y. Qiu, S. Xu, Hierarchical Co_3O_4 nano-micro arrays featuring superior activity as cathode in a flexible and rechargeable zinc-air battery, Advanced Science 6 (2019) 1802243. doi.org/10.1002/advs.201802243.

[50] F. Gui, Q. Jin, D. Xiao, Z. Jin, Y. Zhang, M. Yang, Q. Tan, C. Zhang, S. Siahrostami, Q. Xiao, High-performance zinc-air batteries enabled by hybridizing atomically dispersed FeN_2 with Co_3O_4 nanoparticles, J Mater Chem A Mater 11 (2023) 1312–1323. doi.org/10.1039/D2TA08305A.

[51] G. Li, X. Wang, J. Fu, J. Li, M.G. Park, Y. Zhang, G. Lui, Z. Chen, Pomegranate-inspired design of highly active and durable bifunctional electrocatalysts for rechargeable metal-air batteries, Angewandte, Angewandte Chemie - International Edition 55 (2016) 4977–4982. doi.org/10.1002/anie.201600750.

[52] N. Yu, C. Wu, W. Huang, Y. Chen, D. Ruan, K. Bao, H. Chen, Y. Zhang, Y. Zhu, Q. Huang, W. Lai, Y. Wang, H. Liao, S. Sun, Y. Wu, J. Wang, Nano energy highly efficient Co_3O_4/Co@NCs bifunctional oxygen electrocatalysts for long life

rechargeable Zn-air batteries, Nano Energy 77 (2020) 105200. doi.org/10.1016/j.nanoen.2020.105200.

[53] N. Xu, Y. Liu, X. Zhang, X. Li, A. Li, J. Qiao, J. Zhang, Self-assembly formation of bifunctional Co_3O_4/MnO_2-CNTs hybrid catalysts for achieving both high energy/power density and cyclic ability of rechargeable zinc- air battery, Sci Rep 6 (2016) 33590. doi.org/10.1038/srep33590.

[54] L. Li, L. Fu, R. Wang, J. Sun, X. Li, C. Fu, L. Fang, W. Zhang, Cobalt, manganese zeolitic-imidazolate-framework-derived $Co_3O_4/Mn_3O_4/CN_x$ embedded in carbon nanofibers as an efficient bifunctional electrocatalyst for flexible Zn-air batteries, Electrochimica Actamica A 344 (2020) 136145. doi.org/10.1016/j.electacta.2020.136145.

[55] Y.-P. Deng, Y. Jiang, R. Liang, S.-J. Zhang, D. Luo, Y. Hu, X. Wang, J.-T. Li, A. Yu, Z. Chen, Dynamic electrocatalyst with current-driven oxyhydroxide shell for rechargeable zinc-air battery, Nat Commun 11 (2020) 1952. doi.org/10.1038/s41467-020-15853-1.

[56] M. Wu, G. Zhang, N. Chen, W. Chen, J. Qiao, S. Sun, A self-supported electrode as a high-performance binder- and carbon-free cathode for rechargeable hybrid zinc batteries, Energy Storage Mater 24 (2020) 272–280. doi.org/10.1016/j.ensm.2019.08.009.

[57] S. Li, Z. Xia, W. Zhao, K. Wu, L. Suo, Y. Huo, L. Li, Dandelion-type Mn-promoted Co_3O_4/CNTs composite as an efficient bifunctional electrocatalyst for rechargeable zinc-air batteries, Ionics 27 (2021) 1619–1632. doi.org/10.1007/s11581-021-03963-9.

[58] X. Han, Y. He, X. Zheng, C. Zhong, Engineering catalytic active sites on cobalt oxide surface for enhanced oxygen electrocatalysis, Adv Energy Mater 8 (2017) 1702222. doi.org/10.1002/aenm.201702222.

[59] B. Liu, J. Li, X. Gong, Y. Zhang, Q. Zhou, Facile synthesis of flower-like dual-metal (Co/Zn) MOF-derived 3D porous Co@Co-NPC as reversible oxygen electrocatalyst for rechargeable zinc-air batteries, Ionics 26 (2020) 1913–1922. doi.org/10.1007/s11581-019-03364-z.

[60] Y. Li, M. Gong, Y. Liang, J. Feng, J. Kim, H. Wang, G. Hong, B. Zhang, H. Dai, Advanced zinc-air batteries based on high-performance hybrid electrocatalysts, Nat Commun 4 (2013) 1805. doi.org/10.1038/ncomms2812.

[61] D. Zhang, W. Hu, Study on failure mechanism on rechargeable alkaline zinc-air battery during charge/discharge cycles at different depths of discharge, Front Chem 11 (2023) 1–9. doi.org/10.3389/fchem.2023.1121215.

[62] T.T. Gebremariam, F. Chen, J. Wang, Y. Liu, Bimetallic Mn–Co oxide nanoparticles anchored on carbon nanofibers wrapped in nitrogen-doped carbon for application in Zn–air batteries and supercapacitors, ACS Appl Energy Mater 4 (2018) 1612–1625. doi.org/10.1021/acsaem.8b00067.

[63] C. Tang, B. Wang, H. Wang, Q. Zhang, Defect engineering toward atomic Co-N_x-C in hierarchical graphene for rechargeable flexible solid Zn-air batteries, Advanced Materials 29 (2017) 1703185. doi.org/10.1002/adma.201703185.

[64] D. Yin, M.-L. Wang, Y.-D. Cao, X. Yang, S.-Y. Ji, H.-P. Hao, G.-G. Gao, L.-L. Fan, H. Liu, Polyoxometalate@ZIF induced $CoWO_4/WS_2$@C-N nanoflower as a highly efficient catalyst for Zn–air batteries, ACS Appl Energy Mater 4 (2021) 6892–6902. doi.org/10.1021/acsaem.1c01000.

[65] D.U. Lee, J.Y. Choi, K. Feng, H.W. Park, Z. Chen, Advanced extremely durable 3D bifunctional air electrodes for rechargeable zinc-air batteries, Adv Energy Mater 4 (2014) 1301389. doi.org/10.1002/aenm.201301389.

[66] X.-H.L. and J.-S.C. Li-Na Han, Li-Bing Lv, Qian-Cheng Zhu, Xiao Wei, Highly, ultra-durable two-electrode Zn-air secondary batteries based on bifunctional titania nanocatalysts: Co^{2+} dopant boosts the electrochemical activity, J Mater Chem A Mater 4 (2016) 7841–7847. doi.org/10.1039/C6TA02143C.

[67] K. Chen, S. Kim, M. Je, H. Choi, Z. Shi, Ultrasonic plasma engineering toward facile synthesis of single-atom M-N_4/N-doped carbon (M = Fe, Co) as superior oxygen electrocatalyst in rechargeable zinc-air batteries, Nanomicro Lett 13 (2021) 60. doi.org/10.1007/s40820-020-00581-4.

[68] I.S. Amiinu, X. Liu, Z. Pu, W. Li, Q. Li, J. Zhang, From 3D ZIF nanocrystals to Co-N_x/C nanorod array electrocatalysts for ORR, OER, and Zn-air batteries, Adv Funct Mater 28 (2017) 1704638. doi.org/10.1002/adfm.201704638.

[69] W. Zhang, W. Pu, Y. Qu, H. Yang, Y. Liu, Facile synthesis of ultrathin S-NCo-doped carbon nanosheet as ORR electrocatalysts for application in sustainable zinc-air battery, Electrochim Acta 462 (2023). doi.org/10.1016/j.electacta.2023.142800.

[70] H. Zhou, W. Zhao, Z. Lu, S. He, B. Yin, Y. Zheng, L. Ge, H. Chen, Ba-doped $LaCoO_3$ perovskite as novel bifunctional electrocatalyst for zinc–air batteries, Electrochim Acta 462 (2023) 142757. doi.org/10.1016/j.electacta.2023.142757.

[71] J. Zhu, W. Tu, Z. Bai, H. Pan, P. Ji, H. Zhang, Z. Deng, H. Zhang, Zeolitic-imidazolate-framework-derived Co@Co_3O_4 embedded into iron, nitrogen, sulfur Co-doped reduced graphene oxide as efficient electrocatalysts for overall water splitting and zinc-air batteries, Electrochim Acta 323 (2019) 134821. doi.org/10.1016/j.electacta.2019.134821.

[72] Z. Liu, R. Wang, S. Li, Y. Gu, J. Lan, Q. Zhou, W. Xu, Oxygen vacancy-rich ultrafine CoP/Co_3O_4 nanoparticles as high-efficiency trifunctional electrocatalyst, Electrochim Acta 412 (2022) 140134. doi.org/10.1016/j.electacta.2022.140134.

[73] P. Tan, B. Chen, H. Xu, W. Cai, W. He, M. Ni, Investigation on the electrode design of hybrid Zn-Co_3O_4/air batteries for performance improvements, Electrochim Acta 283 (2018). doi.org/10.1016/j.electacta.2018.07.039.

[74] P. Wang, L. Wan, Y. Lin, B. Wang, Construction of mass-transfer channel in air electrode with bifunctional catalyst for rechargeable zinc-air battery, Electrochim Acta 320 (2019) 134564. doi.org/10.1016/j.electacta.2019.134564.

[75] X. Zhang, Q. Liu, S. Liu, E. Wang, Manganese-doped cobalt spinel oxide as bifunctional oxygen electrocatalyst toward high-stable rechargeable Zn-air battery, Electrochim Acta 437 (2023) 141477. doi.org/10.1016/j.electacta.2022.141477.

[76] M. Wu, X. Tian, W. Yang, B. Guo, J. Guo, Co nanoparticles embedded in wheat-like porous carbon nanofibers as bifunctional electrocatalysts for rechargeable zinc-air batteries, Electrochim Acta 411 (2022) 140090. doi.org/10.1016/j.electacta.2022.140090.

[77] G. Mei, L. Cui, Z. Dou, X. He, Heat-treated multi-walled carbon nanotubes-supported (Fe,Co,Ni)-coordinated polyporphyrin: A robust air cathode catalyst for rechargeable zinc-air batteries, Electrochim Acta 358 (2020) 136918. doi.org/10.1016/j.electacta.2020.136918.

[78] Q. Wang, Y. Xue, S. Sun, S. Li, H. Miao, Z. Liu, $La_{0.8}Sr_{0.2}Co_{1-x}Mn_xO_3$ perovskites as efficient bi-functional cathode catalysts for rechargeable zinc-air batteries, Electrochim Acta 254 (2017) 14–24.
doi.org/10.1016/j.electacta.2017.09.034.

[79] K. Ao, W.A. Daoud, Facile controlled formation of CoNi alloy and CoO embedded in N-doped carbon as advanced electrocatalysts for oxygen evolution and zinc-air battery, Electrochim Acta 395 (2021) 139204.
doi.org/10.1016/j.electacta.2021.139204.

[80] Y. Wang, F. Yan, X. Ma, C. Zhu, X. Zhang, Y. Chen, Hierarchically 3D bifunctional catalysts assembled with 1D MoC core/branched N-doped CNT arrays for zinc-air batteries, Electrochim Acta 367 (2021) 137522.
doi.org/10.1016/j.electacta.2020.137522.

[81] Y. Liang, Q. Gong, X. Sun, N. Xu, P. Gong, J. Qiao, Rational fabrication of thin-layered $NiCo_2S_4$ loaded graphene as bifunctional non-oxide catalyst for rechargeable zinc-air batteries, Electrochim Acta 342 (2020) 136108.
hdoi.org/10.1016/j.electacta.2020.136108.

[82] M. Chen, S. Han, M. Sun, J. Huang, Z. Li, Y. Xu, G. Cheng, L. Yu, Cobalt oxide nanosheets anchored on loofah sponge-derived carbon as a high-performance bifunctional electrocatalyst for rechargeable zinc-air batteries, J Alloys Compd 971 (2024) 172511. doi.org/10.1016/j.jallcom.2023.172511.

[83] X. He, J. Fu, M. Niu, P. Liu, Q. Zhang, Z. Bai, L. Yang, Long-range interconnected nanoporous Co/Ni/C composites as bifunctional electrocatalysts for long-life rechargeable zinc-air batteries, Electrochim Acta 413 (2022) 140183. doi.org/10.1016/j.electacta.2022.140183.

[84] L. Meng, W. Liu, Y. Lu, Z. Liang, T. He, J. Li, H. Nan, S. Luo, J. Yu, Lamellar-stacked cobalt-based nanopiles integrated with nitrogen/sulfur co-doped graphene as

a bifunctional electrocatalyst for ultralong-term zinc-air batteries, Journal of Energy Chemistry 81 (2023) 633–641. doi.org/10.1016/j.jechem.2023.02.035.

[85] L. Gao, M. Zhu, Z. Zhang, G. Cui, Cobalt-boron-oxide supported on N, P dual-doped carbon nanosheets as the trifunctional electrocatalyst and its application in rechargeable Zn-air battery and overall water-electrolysis, Electrochim Acta 327 (2019) 134980. doi.org/10.1016/j.electacta.2019.134980.

[86] J.-Z. He, W.-J. Niu, Y.-P. Wang, Q.-Q. Sun, M.-J. Liu, K. Wang, W.-W. Liu, M.-C. Liu, F.-C. Yu, Y.-L. Chueh, In-situ synthesis of hybrid nickel cobalt sulfide/carbon nitrogen nanosheet composites as highly efficient bifunctional oxygen electrocatalyst for rechargeable Zn-air batteries, Electrochim Acta 362 (2020) 136968. doi.org/10.1016/j.electacta.2020.136968.

[87] X. Shi, Y. Deng, L. Zhao, Y. Gong, R. Wang, H. Wang, B. He, In-situ photodeposition of CoS_x on $Pa_{0.5}Ba_{0.5}Mn_{0.25}Fe_{0.75}O_{3-\delta}$ perovskite to boost bifunctional oxygen electrocatalysis for rechargeable Zn-air batteries, Electrochim Acta 391 (2021) 138951. doi.org/10.1016/j.electacta.2021.138951.

CHAPTER 5
NOBLE METAL-FREE BIFUNCTIONAL HIGH-ENTROPY SPINEL OXIDE FOR REVERSIBLE ZINC-AIR BATTERY

5.1. Introduction

The energy demand and the movement towards a sustainable economy and a greener future are pushing the development of energy systems and supporting catalysts that are cost-effective and environmentally friendly. Thus, an increasing demand for highly active oxygen electrocatalysts that are cost-effective. However, the development of these electrocatalysts remains a challenge. The good electrochemical performance of the oxygen standards ruthenium and iridium oxides and platinum on carbon have a relatively high cost which makes them inefficient for large-scale applications. The use of reduced noble metal loading, non-noble metals, and their oxides as alternative catalysts have been pursued [1].

High-entropy alloys (HEAs) also known as multiple principal element alloys (MPEAs) or complex concentrated alloys (CCAs) [2] have become prominent in the last decade. They are defined as solid solution materials with five or more principal elements in a 5 to 35% molar ratio equal to or near equal atomic percent [3]. For an equimolar system, the stabilised solid solution produces a maximum molar configurational entropy of $\Delta S_{mix} = RlnN$, where N is the number of equimolar components and R is the gas constant [4]. High-entropy materials were developed to stabilise (near) equimolar combinations and create more durable systems [5]. This is accomplished by the metal elements forming a joint lattice. A suitable amount of variation in the structure, coordination, and cationic radii is provided by the equimolar combination [6]. This notion has been used to prepare entropy-stabilised materials [7]. HEAs were first proposed in 2004 by Yeh et al [3]. Since then different HEMs have been developed such as high-entropy oxide [8], nitrides [9], diborides [10,11], carbides [12,13], fluorides [14], chalcogenides [15], half-Heusler [16,17] and silicides [2]. High-entropy oxide (HEO) materials have attracted a lot of attention since their first development by Rost et al. [6]. In their work, they developed a $Mg_{0.2}Co_{0.2}Ni_{0.2}Cu_{0.2}Zn_{0.2}O$ single-phase entropy-driven metal oxide ceramic with a rock salt structure (with a FCC Bravais

lattice) using five cations with equiatomic ratios. This was the first time a confirmed entropy-stabilised oxide with a homogeneous single-phase system was reported.

The diversity of the valence states and chemical components of the oxides/hydroxides in the HEO layers provides a variety of intermediate states, which can help to lower the energy barrier for the chemical reactions, compared to mixed metal oxides with fewer elements [18]. HEOs can have a single structure, better phase stability due to the high-entropy effect, a lattice distortion effect, abundant unsaturated active sites, and a synergistic effect, among other features [19]. The "cocktail" effect, resulting from the mixing of different atomic species causes the appearance of unexpected characteristics due to the cross effect which gives HEMs their exceptional features. The mixed cationic sites can interact with different intermediate species and deliver good catalytic activity [20]. Other inherent properties include corrosion wear and oxidation resistance [21].

HEO synthesis requires high temperatures for uniformly mixed multiple elements with different atomic radii, valences, and oxidation potentials. It is important to develop alternative low-temperature synthetic approaches for the development of HEO nanoparticles. Researchers are excited about the potential of rechargeable zinc-air batteries because they offer several advantages over other types of batteries, such as high energy density, safety, cost-effectiveness, and environmental friendliness [22]. To improve the catalytic activity and diverse functionalities of HEOs, the synthesis of multicomponent high-entropy nanocomposites, such as high-entropy alloy@high-entropy oxides (HEA@HEO) such as a seven-component HEA (PtPdAuAgCuIrRu) clusters supported on seven-component HEO $(AlNiCoFeCrMoTi)_3O_4$ has been tested for oxygen activity [23].

5.2. Experiment

5.2.1. Materials and reagents

All the reagents were of analytical grade and used without further purification. The reagents included 5% Nafion perfluorinated resin containing a mixture of lower aliphatic alcohols and water, isopropanol, ethylene glycol (EG), citric acid (CA), cobalt nitrate ($Co(NO_3)_2$), copper nitrate ($Cu(NO_3)_2$), nickel nitrate ($Ni(NO_3)_2$), manganese

nitrate ($Mn(NO_3)_2$), iron nitrate ($Fe(NO_3)_2$), zinc acetate ($Zn(CH_3CO_2)_2$), potassium hydroxide pellets (KOH, ACS reagent), zinc acetate ($Zn(CH_3CO_2)$), carbon black (Timical Super C45), polytetrafluoroethylene (PTFE), carbon paper, copper strip and zinc plate.

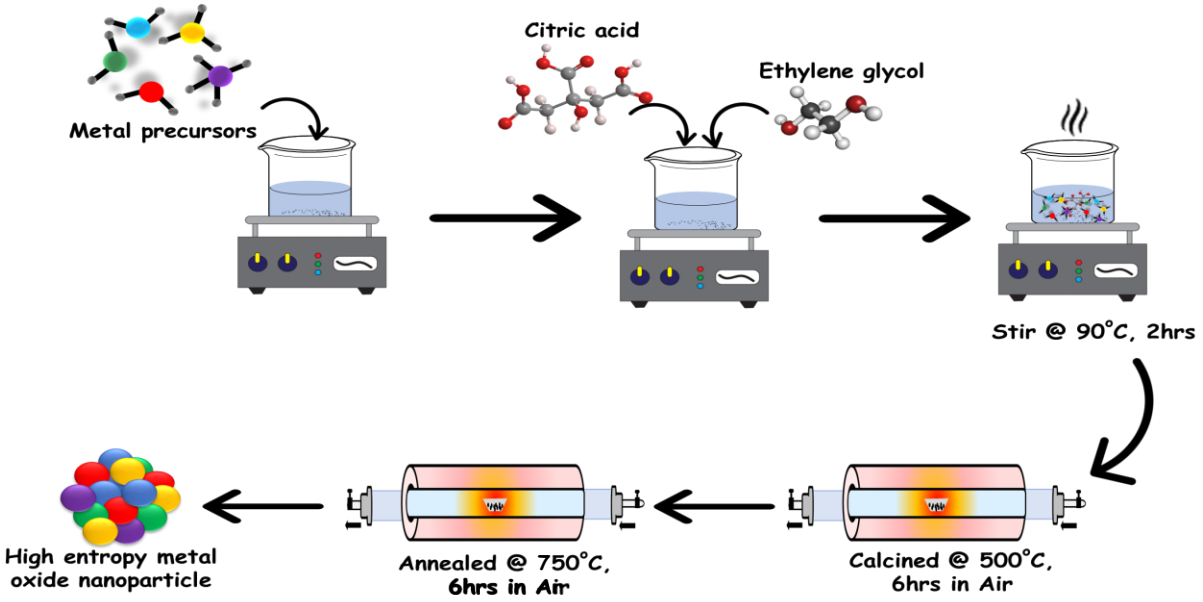

Scheme 5.1: Schematic illustration of the synthesis of HESOx.

5.2.2. Synthesis of $(CuCoNiFeMn)_3O_4$

The schematic illustration of the fabrication process of HESOx is shown in Scheme 5.1. The high-entropy oxide was synthesised through the Pechini method using $Cu(NO_3)_2$, $Co(NO_3)_2$, $Ni(NO_3)_2$, $Mn(NO_3)_2$ and $Fe(NO_3)_2$ nitrate salts. A 1:4 mixture of citric acid to ethylene glycol was measured and dissolved in deionised water. The stoichiometric amounts of the metal nitrate salts were weighed and each dissolved in deionised water and magnetically stirred. Thereafter, the metal nitrate solutions were added dropwise into the CA and EG solution. The solution was then heated from room temperature to 90 ^oC while constantly stirring to form a polymeric resin. The resin eventually dehydrated ultimately forming a black powder. The powder was annealed to 500 ^oC and maintained for 6 hours in air. A portion of the resulting sample (HESOx-500) was further annealed to 750 ^oC for 6 hours in air resulting in HESOx-750.

Table 5.1: Comparative synthesis procedures of high-entropy materials.

High-entropy material	Synthesis method	Morphology	Reference
CoCuFeMnNi	Pechini at 90 ^{o}C followed by calcination at 500 ^{o}C and 750 ^{o}C	Spherical	This work
MnFeCoNi, CrMnFeCoNi, and CuMnFeCoN	Vacuum/argon Schlenk lines at 90 to 260 ^{o}C	Octahedral	[24]
(Co,Cu,Fe,Mn,Ni)/MWCNT	Autoclave and heated at 170 °C for 15 h followed by calcination at 400 ^{o}C	Multiwall carbon nanotube	[18]
FeNiCoMnRu@CNT	Calcination at 600 ^{o}C in argon using a tube furnace	Nanotube	[25]
FeCoNiMnV HEA/N-CNTs	One-step pyrolysis at 800 ^{o}C under N_2 atmosphere	Bamboo-like carbon nanotubes entrapped with nano-particles	[26]
AlNiCoFeCrMoV/CoNC	Induction-melting furnace under Ar followed by melt-spinning to prepare the alloy ribbons. This was then followed by chemical dealloying in a 0.5 M NaOH solution for 12 h at room temperature	Nanoporous ribbon	[27]
Al-Ni-Co-Ru-Mo-Cr-Fe-Ti	The pure metals were melted in an induction-melting furnace under Ar. The alloy was melted again in the quartz tube and injected into the air to contact the high-speed rotating copper roller. Followed by etching in 0.5 M NaOH	Multicomponent amorphous-like material	[28]
AlNiCoRuMo	The pure metals were melted in an induction-melting furnace under Ar. The alloy was melted again in the quartz tube and injected into the air to contact the high-speed rotating copper roller. Followed by etching in 0.5 M NaOH	Nanowire	[29]
$Fe_{12}Ni_{23}Cr_{10}Co_{55-x}Mn_x$/ CNT	The metals were dissolved in water, which	Spherical HEM	[30]

	was deoxygenated by bubbling nitrogen gas. After introducing PVP and CNTs, the material was acid-treated with H_2SO_4 and HNO_3 at 120 °C. $NaBH_4$ was added to the solution which was filtered and freeze-dried. The powder was sintered at 900 °C in Ar and 10% H_2 and then quenched in liquid nitrogen.	on carbon nanotubes	
FeCoNiMoW	The metal mixture was vacuumed at 70 ℃ and increased to 260 ºC in Ar Schlenk line, followed by cooling to 220 ºC then rapidly cooled down to room temperature.	Urchin-like particle	[31]
CuCoMnNiFe	The metals were melted in a vacuum in a furnace three to four times and solidified. Then vacuum sealed inside a quartz tube and homogenised at 1000 °C. then quenched in cold water to freeze. The powder was then cryomilled in liquid nitrogen under Ar.	Spherical	[32]

5.2.3. Physical Characterisation

Several characterisation techniques were used to study the composition, structure, and behaviour of the synthesised materials (HESOx-500 and HESOx-750). These techniques include Powder X-ray diffraction (P-XRD), Raman spectroscopy, X-ray Photoelectron Spectroscopy (XPS), Scanning Electron Microscopy (SEM), Energy Dispersive Spectroscopy (EDS), Transmission Electron Microscopy (TEM), Brunauer–Emmett–Teller (BET), Thermogravimetric analysis (TGA), Ultraviolet photoelectron spectroscopy (UPS) and Electron paramagnetic resonance spectroscopy (EPR).

5.3. Results and Discussion

5.3.1. Physical characterisation

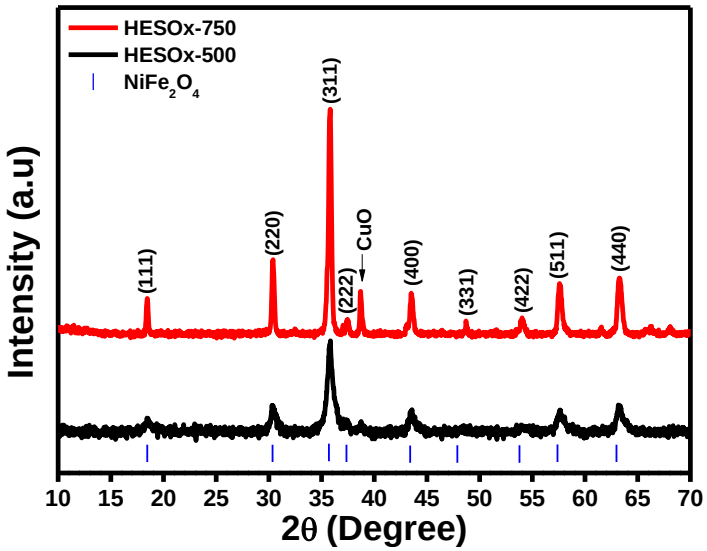

Figure 5.1: Powder XRD diffractogram of HESOx-500 and HESOx-750.

The crystal structure change of the HESOx was studied with powder X-ray diffractogram (P-XRD) (Figure 5.1) at 2θ range of 10°-90°. As in similar reports by Dąbrowa et al. [33], Wang et al. [18] and Xue et al [34] all cations show similar ionic radii and can exist in the Me^{2+} state forming a Fd-3m spinel single phase MeO oxide [33]. Three phases in alloys are mainly expected i.e. FCC, BCC and ordered BCC (B2) [3]. Thus, the expected combination resulted in the formation of a single-phase HESOx. The FCC was the predominant phase with the strongest diffraction peaks at 30.5º and 35.8º corresponding to the reflections of {220} and {311}, respectively. The lower intensity peaks were located at 18.5º, 37.5º, 43.5º, 48.8º, 54.0º, 57.7º and 63.2º associated with the reflection of {111}, {222}, {400}, {331}, {422}, {511} and {440} as labelled in Figure 5.1, which was very similar to the pattern of $NiFe_2O_4$ [35–37]. In a study by Rost et al [6], in the preparation of entropy-stabilised oxides, they found that after 700 ºC, two significant phases emerge: rocksalt and tenorite. However, the rocksalt completely converts to a single phase between 850 and 900 ºC. A similar work by Dessica et al. [38] also showed a similar outcome. A trace of CuO tenorite was observed at 38.76 2θ, which was more intense in the spectra of HESOx-750. In terms of the two samples (HESOx-500 and HESOx-750), there is no evident change in the phase structure in terms of peak shift. However, the diffraction peak intensity of the HESOx-750 was intense and sharper with an increase in the calcination

temperature, indicating the improvement of crystallinity. There was an evident change in the crystallinity and grain sizes with an increase in the annealing temperature, which is deduced from the reduced full width at half maximum. The particle size calculated from the Scherrer equation was calculated to be 10.995 nm for HESOx-500 and 24.670 nm for HESOx-750. The increase in the particle size was due to the higher annealing temperature which caused particle agglomeration.

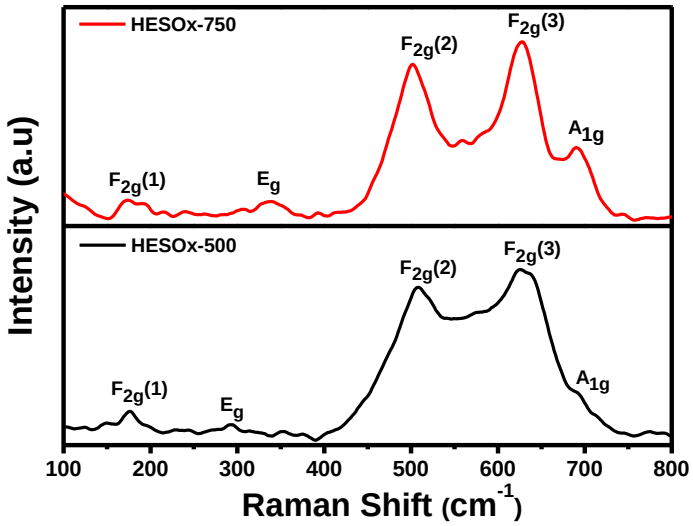

Figure 5.2: Raman spectroscopy of HESOx-500 and HESOx-750.

Figure 5.2 shows Raman modes also observed by Diallo et al. [39], where they reported a spinel structure predicted by the factor group analysis for the fcc spinels (space group Fd-3m) with assigned five phonon modes namely E_g, A_{1g} and $3F_{2g}$. The A_{1g} mode is responsible for the symmetric stretching vibration of the oxygen anion in relation to the metal ion on the tetrahedral side. These can be observed at 681-706 cm^{-1} for HESOx-500 and a weaker band at 674-732 cm^{-1} for HESOx-750. The symmetric and antisymmetric bending of the oxygen atom in the M-O bond at the octahedral sides was responsible for the bands that appeared at 135-213 cm^{-1}, 283-310 cm^{-1}, 390-537 cm^{-1} and 587-681 cm^{-1} for HESOx-500, and 154-206 cm^{-1}, 316-369 cm^{-1}, 423-546 cm^{-1} and 568-667 cm^{-1} for HESOx-750, which corresponded to the $F_{2g}(1)$, E_g, $F_{2g}(2)$ and $F_{2g}(3)$ modes, respectively [40–43], demonstrating the vibration of the spinel structure. The E_g mode was associated with the symmetric bending vibration of oxygen anions, and the T_{2g} mode was attributed to the asymmetric stretching of oxygen anions [20].

However, the Raman spectra collected for HESOx-500 and HESOx-750 agreed well with those reported by Diallo. The Raman modes of the HESOx samples appear to be broader and shifted when compared. The observed band shift in both directions from the A_{1g}, F_{2g} and E_g might be due to metal ion replacements in the spinel structure and the differences in charge and ionic radii which caused a change in the stretching and vibrational energy [43,44]. The shift can also be linked to an increase in particle size and cation redistribution with an increase in annealing temperature [45]. An observed broadening of the high-entropy modes has also been reported by Zhang et al. [46], Dąbrowa et al [33] and Krysko et al [8]. As expected for high-entropy compounds, these widened and shifted Raman modes offer direct evidence of severe lattice distortions in the high-entropy spinels [8]. The peak broadening was caused by the change in the phonon lifetime which resulted from a wide range of phonon energy distribution depending on how various mass atoms were distributed within these materials [8]. These energy variations were caused by the slow movement of vibrational modes across regions of the sample containing a greater concentration of smaller elements and more quickly through regions containing a greater number of atoms with higher masses, resulting in broader Raman peaks [8].

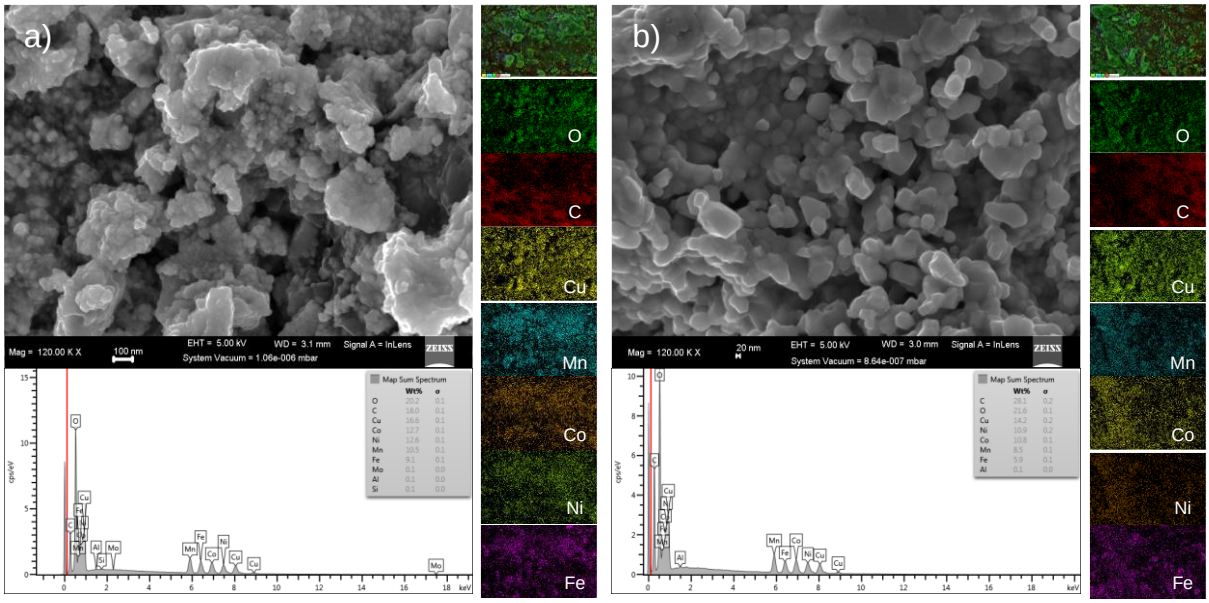

Figure 5.3: SEM images along with EDX and elemental mapping of (a) HESOx-500 and (b) HESOx-750.

The change in the morphology with an increase in temperature could be observed from the SEM images. Figure 5.3a (HESOx-500) showed clusters of dominant nanospheres and other nanoforms. A more crystalline structure of mixed morphology was observed for HESOx-750 (Figure 5.3b). The compositional homogeneity at the nanoscale was confirmed by EDX mapping for different metallic elements. The EDX analysis for both materials showed the presence of all the elements with a fair distribution of weight percentage. The elemental mapping showed high dispersity of the five elements and oxygen with no apparent trend towards separation or aggregation on the scanned area.

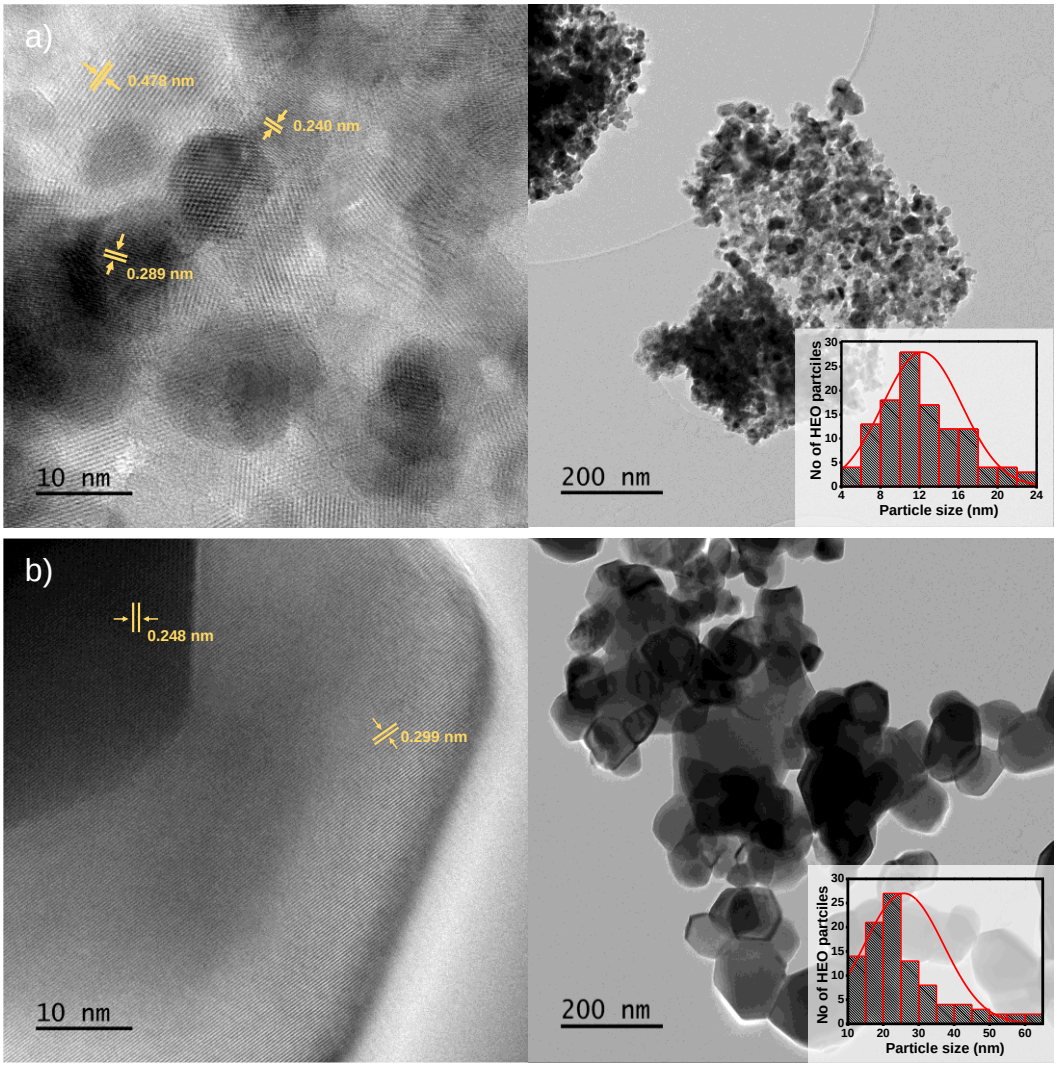

Figure 5.4: HR-TEM images of (a) HESOx-500 and (b) HESOx-750.

The microstructure of the complexes was further studied with high-resolution transition electron microscopy (HR-TEM). The morphologies were in good agreement with the observed SEM image of HESOx-500 and HESOx-750. The sharp lattice fringes seen in Figure 5.4 were in support of the good crystallinity seen in P-XRD. The lattice d spacing for HESOx-500 was measured to be 0.289 nm, 0.478 nm and 0.240 nm, indexing to {220}, {111} and {311} lattice planes in the spinel structure, respectively [34]. In the case of HESOx-750 were the {111} and {311} diffraction planes the *d* spacings of 0.299 nm and 0.248 nm. These results were in support of high crystallinity and single structure of the material observed from P-XRD. Furthermore, the average particle size of the material was approximated at 11 $\pm$ 0.8 nm for HESOx-500 (Figure 5.4a) and 25 $\pm$ 0.6 nm for HESOx-750 (Figure 5.4b), agreeing to the calculated nanoparticle size from P-XRD.

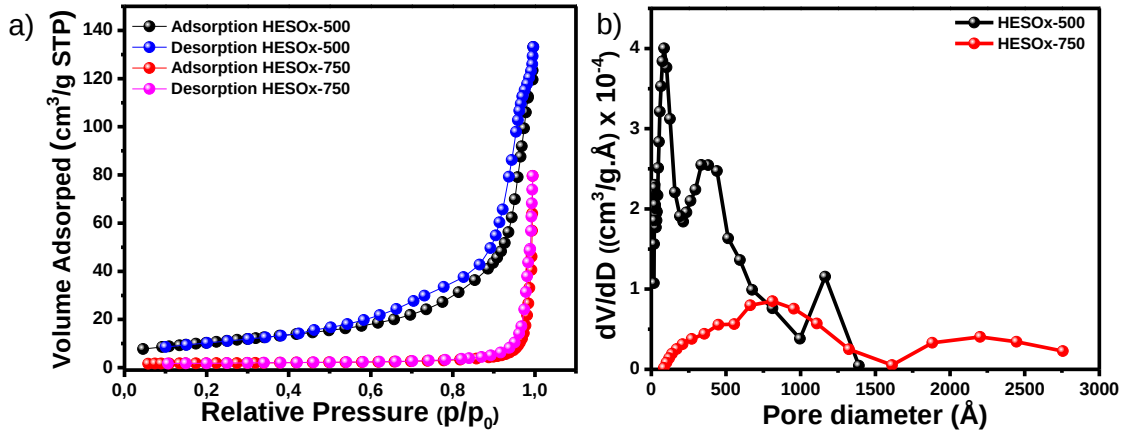

Figure 5.5: (a) N_2 adsorption-desorption isotherm and (b) Pore size distribution of HESOx-500 and HESOx-750.

Table 5.2: Nitrogen gas adsorption analysis of HESOx-500 and HESOx-750.

Catalyst	BET surface area (m^2/g)	Pore volume (cm^3/g)	Pore size (Å)
HESOx-500	37.60	0.18	193.52
HESOx-750	5.98	0.097	1003.52

The surface area and pore size distribution of both materials were determined by N_2 adsorption-desorption isotherm. Figure 5.5 represents the BET analysis of HESOx-

500 and HESOx-750, their BET results are summarised in Table 5.2. The BET isotherm in Figure 5.5a displayed hysteresis loops at a relative pressure of 0.4 to 1 for HESOx-500 and 0.7 to 1 for HESOx-750. HESOx-500 (Figure 5.5a) showed a type IV isotherm with a combination of H3 hysteresis loop, characteristic of meso-macroporous and irregular pore structure. The specific surface area (S_{BET}) of HESOx-500 was 37.6 m^2/g with a total pore volume of 0.18 cm^3/g. The corresponding Barrett-Joyner-Halenda (BJH) pore size distribution in Figure 5.5b also showed that the sample had a meso-macroporous structure with a pore size range of 23.4 to 1167.7 Å. The effect of increased heat treatment on HESOx-750 was evidenced by a smaller S_{BET} of 6.0 m^2/g (Figure 5.5a). This was because high combustion temperatures can cause particles to agglomerate and increase in size and reduce the specific surface areas of the material. HESOx-750 (Figure 5.5a) showed a type III isotherm and a H4 hysteresis loop. The type III isotherm can be observed on the surface of a nonporous or macroporous solid [47]. The BJH pore size distribution appeared to be broad in the range of 83.7 to 2754.9 Å, indicating the existence of macropores. Generally, materials with high surface area and mesoporous configurations show better electrochemical response.

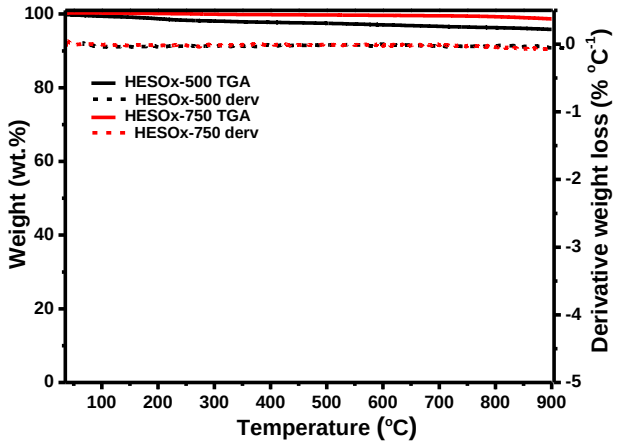

Figure 5.6: TGA and derivative analysis of HESOx-500 and HESOx-750.

TGA was used to study the transformation of HESOx-500 and HESOx-750. The sample weight was monitored from 35-900 °C at a heating rate of 10 °C/min under air at a flow rate of 20 ml/min. Figure 5.6 shows that both materials had high stabilising temperatures due to the compatible chemical composition of the elements as a result of their similar atomic radii. HESOx-750 showed a steady state temperature decay

from 100 ^{o}C to 900 ^{o}C. HESOx-500 had a more dramatic weight loss profile at 4.1% which was very high compared to HESOx-750 which had a weight loss of 0.9%. Their derivative curves showed no obvious degradation profiles. From TGA it is conclusive that an increase in the thermal treatment temperature significantly improved the thermal stability of the structure.

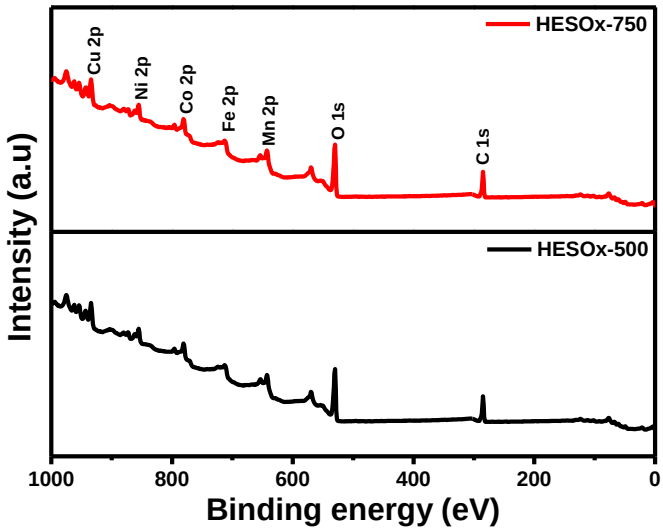

Figure 5.7: XPS survey spectra of HESOx-500 and HESOx-750.

X-ray photoelectron spectroscopy (XPS) of HESOx-500 and HESOx-750 were analysed to further investigate the composition of the complex and its purity, the survey spectra in Figure 5.7 showed the core levels of Cu, Ni, Co, Mn, Fe, and O were measured for both samples. The black line in the fine-scan data (Figure 5.8) represented the original data, the sum of the peak fits was shown with a pink dotted line and the peak fits of the individual components were shown using coloured lines. The fine scans of the elemental spectra were deconvoluted to determine the peak positions of the respective binding energies. The deconvoluted peaks co-existed with their respective satellite peaks. The scans showed +2 and +3 oxidation states of the metal ions. The presence of the metallic peaks in the materials had small intensities indicating that only a small amount of the material atoms was reduced to the metallic form. HESOx-750 showed a shift to higher binding energy with only iron shifting to lower binding energy. The higher shift implied electron movement from the elements to the surrounding atoms while the lower shift attracted electrons [24]. The existence of Cu^{2+} in Figure 5.8a was evidenced by two strong satellite peaks in the materials [48]. The Cu^{2+} could be observed at the major peaks of $2p_{1/2}$ and $2p_{3/2}$, which co-

existed with Cu^0 in HESOx-750. The fine-scan of Ni 2p in Figure 5.8b was assigned to Ni $2p_{3/2}$ and Ni $2p_{1/2}$ along with their satellite peaks, both deconvoluted to Ni^{3+} and Ni^{2+} at higher and lower binding energy respectively. The Ni^{3+} peak at $2p_{3/2}$ suggested the bonding of nickel to iron [49]. The Fe scan shifted towards a negative biding energy assuming electron transfer towards it [24].

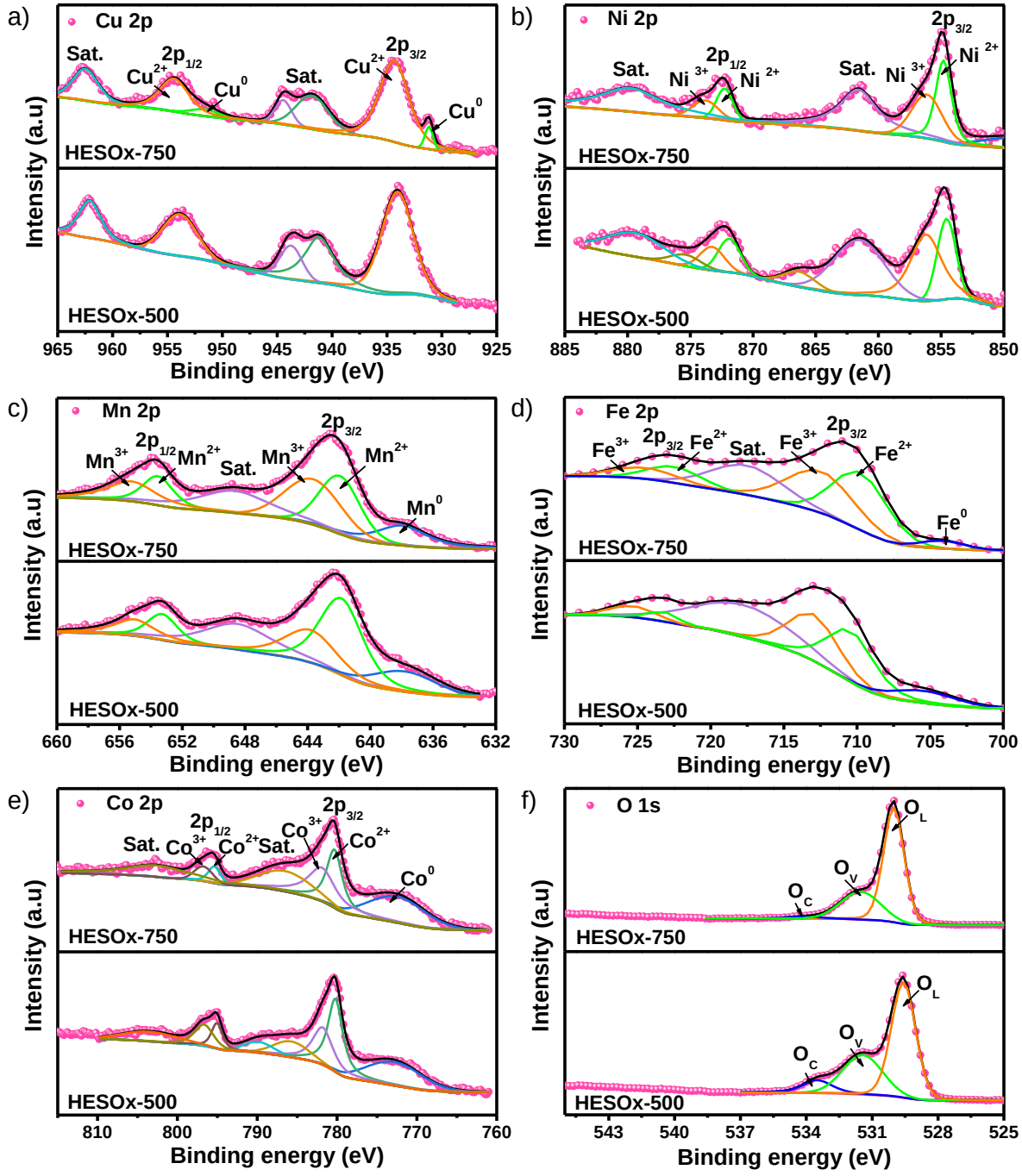

Figure 5.8: XPS spectra of a) Cu 2p, b) Ni 2p, c) Mn 2p, d) Fe 2p, e) Co 2p and f) O 1s of HESOx-500 and HESOx-750.

The scan also showed two doublet peaks of Mn $2p_{3/2}$ and Mn $2p_{1/2}$ responsible for Mn^{2+} and Mn^{3+} (Figure 5.8c). The fine scans of Fe in Figure 5.8d showed the presence of metallic iron (Fe^{0}), Fe^{2+} and Fe^{3+}. The Co 2p scan in Figure 5.8e showed Co $2p_{3/2}$ and Co $2p_{1/2}$ peaks and their two satellite peaks assigned to Co^{2+} oxidation state [18]. In the fine-scan of O 2p (Figure 5.8f), three peaks were observed and assigned to three surface oxygen species; the O_C chemisorbed and dissociated oxygen species (O_2^-, O^{2-} or O^-) and hydroxide ions (OH^-); oxygen vacancies (O_V) associated with the O_2^- defect ions; and the lattice oxygen (O_L) corresponding to the metal-oxygen bond [50]. Table 5.3 summarises the relative percentage variation of oxygen on the surface of the HESOx materials. The relative percentage of O_c in HESOx-500 (9.6%) was higher than that of HESOx-750 (0.3%). The porosity of HESOx-500 allowed it to absorb more oxygen species than its parent material. However, no other peaks were observed in the O1s region. This may be due to the absence of impurities and contamination in the oxide film. The oxygen defects produced were desirable for water-splitting electrocatalysis processes because they could act as active sites to interact with the oxygen-containing intermediates [51].

Table 5.3: O 1s XPS spectra curve fitting of HESOx-500 and HESOx-750.

Sample		O_L (Co−O)	O_V (vacancy)	O_C (chemisorbed)
HESOx-500	binding energy (eV)	529.6	531.4	533.5
	relative percentage (%)	58.0	32.4	9.6
HESOx-750	binding energy (eV)	530.0	531.5	534.1
	relative percentage (%)	69.9	29.8	0.3

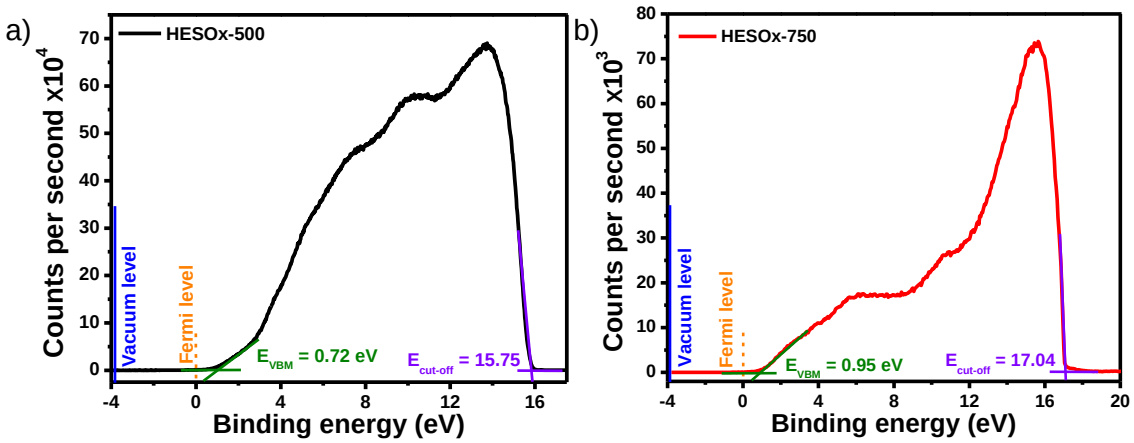

Figure 5.9: Ultraviolet photoelectron spectroscopy (UPS) measurements of (a) HESOx-500 and (b) HESOx-750.

Ultraviolet photoelectron spectroscopy (UPS) with a He (I) (21.22 eV) excitation source was used to analyse the changes in the work function (φ), valence band maximum (E_{VBM}) also known as valence band edge and ionisation potential (IP) of the materials with an increase in annealing temperature. As seen in Figure 5.9(a & b), the secondary electron cut-off of HESOx-750 was shifted towards higher binding energy compared to HESOx-500, which reflected a lower work function of the HESOx-750. The φ was calculated using equation 5.1 [52]:

$$\varphi = hv - E_{cut\text{-}off} - E_f \quad (5.1)$$

where hv was the incident photon energy, $E_{cut\text{-}off}$ was the high-binding-energy secondary cut-off, and E_f was the energy at the Fermi level (E_f = 0 eV). The work function of HESOx-500 and HESOx-750 were calculated to be 5.47 eV and 4.08 eV, respectively. The E_{VBM} value was computed using linear extrapolation in Figure 5.9, by fitting a straight line on the low kinetic energy cut-off, followed by finding its intersect on the baseline of the spectra. The IP was then determined by IP = hv - ($E_{cut\text{-}off}$ - E_{VBM}) yielding 6.19 eV for HESOx-500 and 5,03 eV for HESOx-750. In the work by A.R. Lopes da Silva, they demonstrated that compounds with smaller HOMO energy and high IP were more stable [53]. The compounds with these features showed higher oxidation potential peaks, denoting that the lower the energy of the HOMO orbital, the more stable the compound because of the high energy needed to remove the electrons in the orbital. This meant that even though HESOx-750 had a lower φ compared to HESOx-500, i.e. it can easily remove electrons from its surface, HESOx-500 had higher stability compared to it.

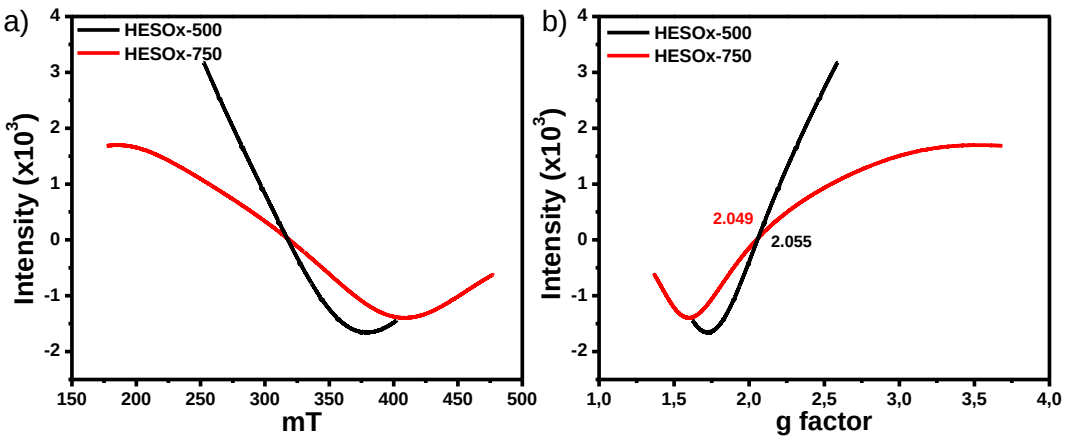

Figure 5.10: (a) ERP spectra and (b) Calculated g-factor plot of HESOx-500 and HESOx-750.

The electron paramagnetic resonance (EPR) was used to investigate the concentration of oxygen vacancies in the HESOx catalysts. The EPR technique is sensitive to unpaired electrons. The g factor in Figure 5.10 for HESOx-500 was 2.055 and 2.049 for HESOx-750. Xue et al. also reported a g factor of 2.004 which was determined as trapped electrons on surface oxygen vacancies [53]. They suggested an increase in intensity of the signal with calcination temperature to be due to more oxygen vacancies that were present in the material. Though the observed signals in this work were not obvious to estimate the oxygen valency state of the materials, it could be observed from Figure 5.10 that the lower heat-treated material had a higher intensity. It is known that higher calcination temperature can change the surface morphology and pore structure of materials causing nanoparticle aggregation which in turn reduces the catalytic activity. A material with a higher concentration of oxygen defect (HeSOx-500) sites would be able to adsorb more oxygen species and accelerate the use and addition of lattice oxygen [53]. Furthermore, the metal oxides' ability to constantly accept the adsorption and activation of gas-phase oxygen on their surface oxygen vacancies in order to create surface-adsorbed oxygen, helped accelerate the participation of lattice oxygens in reactions [53].

5.4. Electrochemical measurements

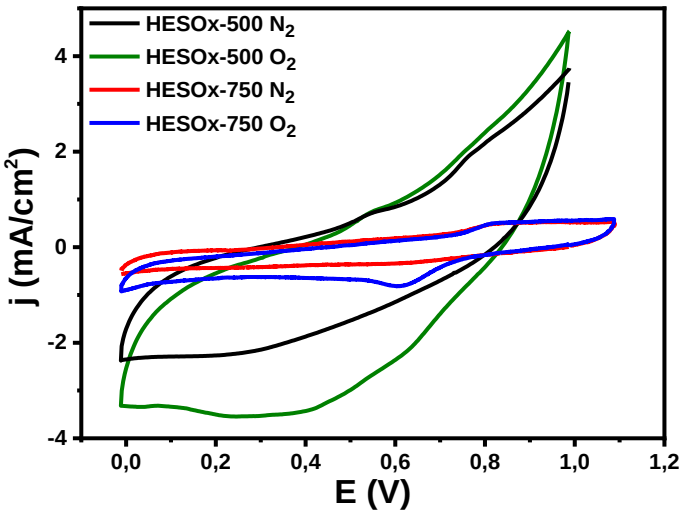

Figure 5.11: Cyclic voltammetry curves of HESOx-500 and HESOx-750 measured in 1 M KOH under N_2 and O_2 saturated solution at 50 mV/s.

Cyclic voltammetry (CV) in 1 M KOH was initially used to evaluate the electrochemical response of the catalysts in the electrolyte. The reported HESOx cathode electrode was optimised with carbon black, to improve mass transport and conductivity. The comparative cyclic voltammetry curves were measured under N_2 and O_2 saturated 1 M KOH solution at 50 mV/s (Figure 5.11). In the N_2 saturated medium, no identifiable electrochemical characteristic was obtained other than the non-Faradaic current characteristic of a double-layer charge-discharge. When the electrolyte was saturated with O_2, a prominent cathodic peak was seen for HESOx-750 and a weak peak for HESOx-750, but a stronger conductive response indicating a better electrocatalytic activity toward ORR. HESOx-500 showed a higher non-Faradaic response, indicative of an improved ability to store more charge than HESOx-750. Cyclic voltammetry was conducted at different scan rates (Figure 5.12(a & b)) and used to measure the double layer capacitance (C_{dl}) and the electrochemical active surface area (ECSA) (Figure 5.12(c & d)) of HESOx-500 and HESOx-750. The C_{dl} was calculated to be 10.01 $\pm$ 0.7 mF/cm^2 for HESOx-500 and 0.92 $\pm$ 0.6 mF/cm^2 for HESOx-750. The large C_{dl} of HESOx-500 indicated that the catalyst could provide more active sites to boost the catalytic reaction rate. The ECSA of HESOx-500 was 250.25 $\pm$ 0.5 cm^{-2} while that of HESOx-750 was 23 $\pm$ 0.4 cm^{-2}.

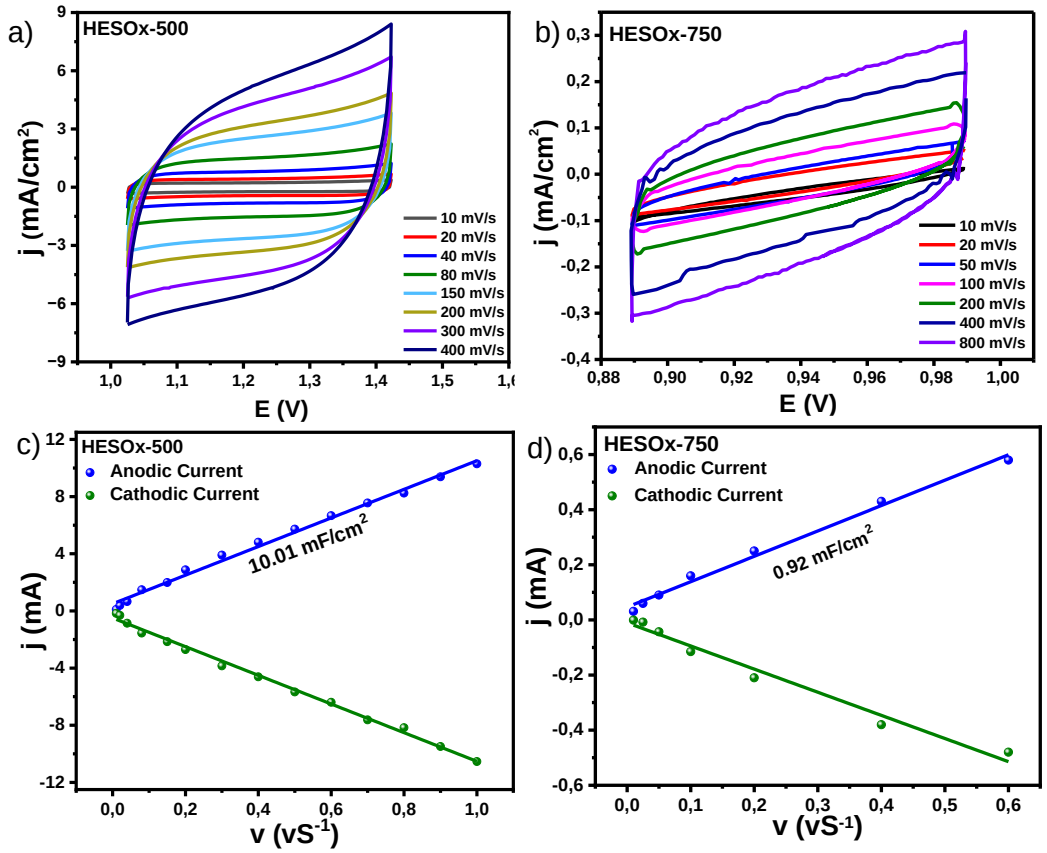

Figure 5.12: Non-Faradaic cyclic voltammetry curves of (a) HESOx-500 and (b) HESOx-750 and the C_{dl} of c) HESOx-500 and (d) HESOx-750 measured in 1 M KOH at different scan rates.

5.4.1. Oxygen reduction reaction (ORR)

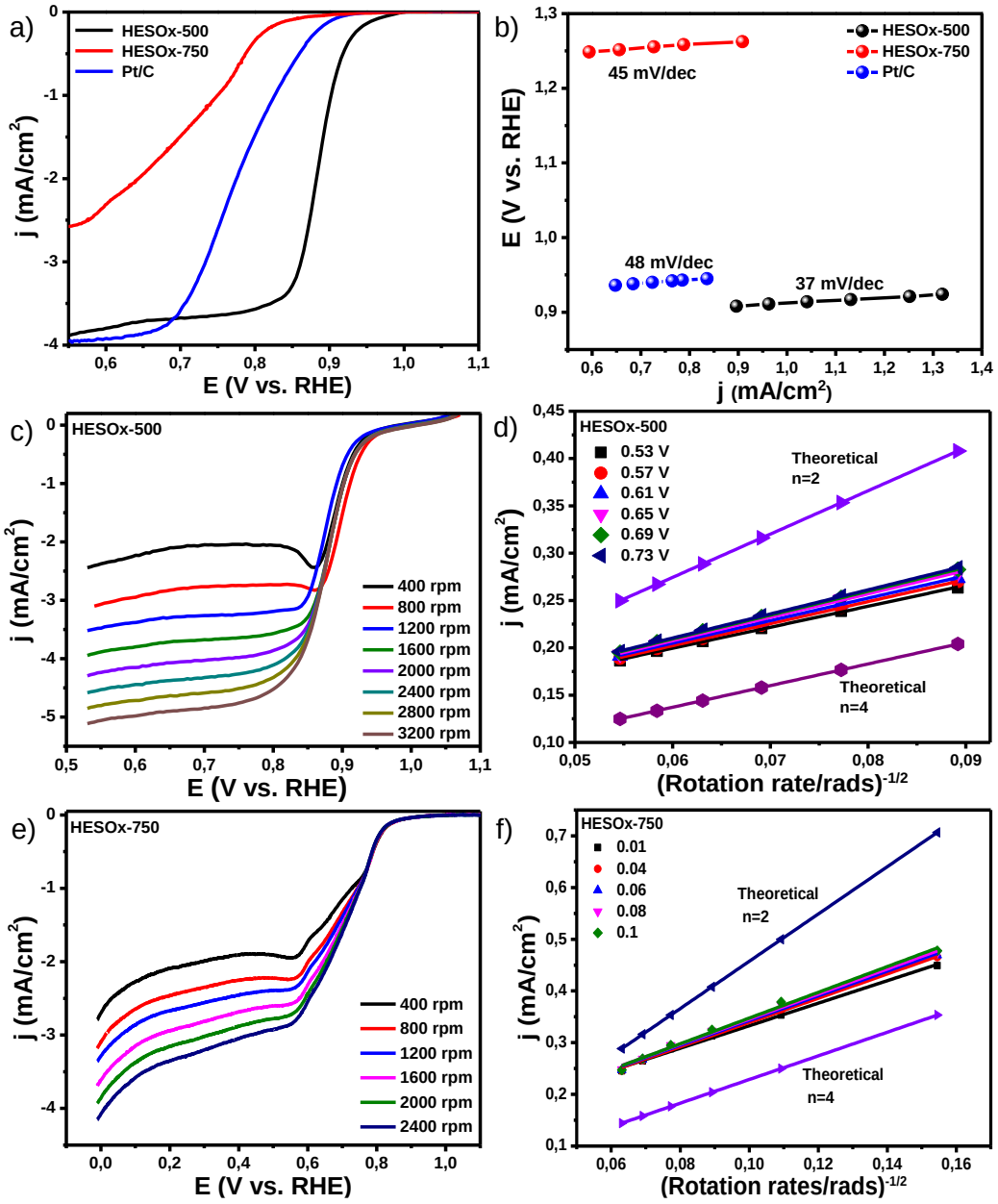

Figure 5.13: HESOx-500, HESOx-750 and Pt/C (a) ORR polarisation curves at 1600 rpm at 10 mV/s and (b) corresponding Tafel plots, ORR polarisation curves at different rotation speed for (c) HESOx-500 and (e) HESOx-750, and Koutecky-Levich (K-L) plots of (d) HESOx-500 and (f) HESOx-750 at varied potentials in O_2 saturated 1.0 M KOH.

To evaluate the ORR performance of HESOx-500 and HESOx-750, LSV was performed in an O_2 saturated electrolyte. The ORR parameters of HESOx samples were compared to Pt/C at 1600 rpm (Figure 5.13a). The half-way potential ($E_{1/2}$) and onset potential (E_{onset}) are key parameters that were used to evaluate ORR. The $E_{1/2}$ of HESOx-500, HESOx-750 and Pt/C were measured to be 0.88 V, 0.70 V and 0.78 V, respectively. While the E_{onset} potentials were 0.93 V (HESOx-500), 0.83 V (HESOx-750) and 0.89 V (Pt/C). The Tafel slope was used to study the catalytic mechanism of electrocatalysis for the ORR (Figure 5.13b). The small Tafel slope of HESOx-500 (37 $\pm$ 6.7 mV/dec) to HESOx-750 (45 $\pm$ 5.0 mV/dec) and Pt/C (48 $\pm$ 3.7 mV/dec), indicated a highly favourable reaction kinetics and higher catalytic efficiency and sensitivity of the electrocatalyst. Figure 5.13(c & e) shows the LSV curve of HESOx-500 at different rotation speeds in the range of 400 rpm to 3200 rpm at 10 mV/s. As anticipated, the enhanced diffusion of oxygen surrounding the electrode surface caused the limiting current density to increase with rotation speed. The kinetics of the electrode were then investigated using the Koutecky-Levich plot (Figure 5.13(d & f)). An estimate of 3.97 for HESOx-500 and 3.73 for HESOx-750 was made for the potential-independent electron transfer number for ORR based on the overlap of the curves obtained at various voltages. Hence, the HESOx-500 electrode demonstrated a strong selectivity for a one-step four-electron oxygen reduction route. The electron transfer rate constant (k) was calculated at j_L of 0.90 V using equations 2.24 and 2.25 and determined to be 3.35 x 10^{-3} cm/s and 8.55 x 10^{-5} cm/s for HESOx-500 and HESOx-750, respectively. The higher rate constant of HESOx-500 supports a faster electron transfer rate and implies improved efficiency of the electrochemical device.

5.4.2. Oxygen evolution reaction (OER)

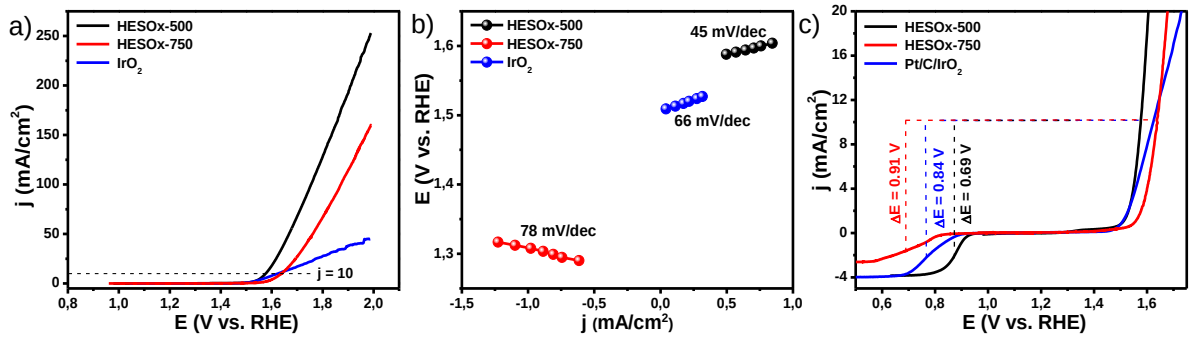

Figure 5.14: HESOx-500, HESOx-750 and Pt/C/IrO_2 (a) polarisation curves at 1600 rpm and 10 mV/s, (b) Tafel slopes and (c) ORR/OER polarisation curves compared to Pt/C/IrO_2 vs. RHE in 1.0 M KOH at the scan rate of 10 mV/s at 1600 rpm.

OER activity of the catalyst was also studied in 1 M KOH electrolyte (Figure 5.14a). The overpotential of HESOx-500 at 10 mA/cm^2 (η_{10}) was recorded at 340 mV, which was higher than that of HESOx-750 (410 mV) and IrO_2 (390 mV). The response also corresponded to observed Tafel slope (Figure 5.14b) values following the inverse trend (HESOx-500 < HESOx-750 < IrO_2), translating to a faster electron kinetics for HESOx-500. The potential difference (ΔE) between the $E_{1/2}$ for ORR and the η_{10} for OER served as the quantitative assessment of the bifunctionality of the catalysts' potential performance toward oxygen processes. The ΔE (Figure 5.14c) was calculated to be 0.69 V for HESOx-500, 0.91 V for HESOx-750 and 0.84 V for Pt/C/IrO_2. The great performance of HESOx-500 was attributed to the combination of the synergistic effects of various metal elements, a large number of electroactive sides, and the presence of oxygen defects. The performance of the oxygen reactions was compared to the reported literature in Table 5.4. These results suggested a good electrochemical performance and stability of HESOx-500 nanoparticles for practical electrochemical applications.

Table 5.4: ORR and OER performance comparison of HEMs with recently reported catalysts.

Catalyst	Electrolyte	E_{onset} (V)	$E_{1/2}$ (V)	$E_{j=10\ mV/s}$ (mV)	ΔE (V)	Tafel (mV/dec)	Reference
CoCuFeMnNi-500 CoCuFeMnNi-750 Pt/C+IrO_2	1 M KOH	0.93 0.82 0.89	0.88 0.73 0.78	340 410 390	0.69 0.91 0.84	45 66 78	This work
CrMnFeCoNi MnFeCoNi CuMnFeCoNi RuO_2-20wt%Pt/C	0.1 M KOH	0.88	0.78	265 258 298 293	0.734 0.76	37.9 46.8 49.1 90.0	[24]
FeNiCoMnRu@CNT	Seawater + 1 M KOH	-	-	319	-	56	[25]
FeCoNiMnV HEA/N-CNTs FeCoNiMnV HEA/N-CNTs-700 FeCoNiMnV HEA/N-CNTs-900 FeCoNiMn FeCoNi Pt/C	0.1 M KOH	0.99 0.94 0.91 0.95 0.94 0.96	0.85 0.81 0.78 0.81 0.80 0.83	-	-	77.22 84.24 86.33 99.39 82.01 87.66	[26]
(Co,Cu,Fe,Mn,Ni)/MWCNT, Co,Cu,Fe,Mn,Ni	1 M KOH	-	-	350 400	-	59.5 76.7	[18]
AlNiCoFeCrMoV/CoNC	0.1 M KOH ORR and 1 M KOH OER	-	0.85	254	0.64	54.6	[27]
Al-Ni-Co-Ru-Mo-Cr-Fe-Ti AlNiCoRuMo RuO_2 Pt/C	0.1 M KOH ORR and 1 M KOH OER	0.99 0.99 0.92 0.98	0.865 0.87 0.78 0.85	240 245 310	0.605 0.605 0.76	51.3 54.6 72.4	[28]

AlNiCoRuMo	0.1 M KOH ORR and 1 M KOH OER	0.99	0.875	245	0.61	54.5	[29]
$Fe_{12}Ni_{23}Cr_{10}Co_{30}Mn_{25}$/ CNT	0.1 M KOH ORR and 1 M KOH OER	0.87	0.84	284	0.70	62	[30]
FeCoNiMoW FeCoNi FeCoNiMo FeCoNiW RuO_2	0.1 M KOH ORR and 1 M KOH OER	0.83	0.71	233 304 294 283 326	0.75	36.7	[31]
CuCoMnNiFe	1 M KOH	0.78	0.69	380	0.92	89.7	[32]

5.4.3. Rechargeable Zinc-air battery

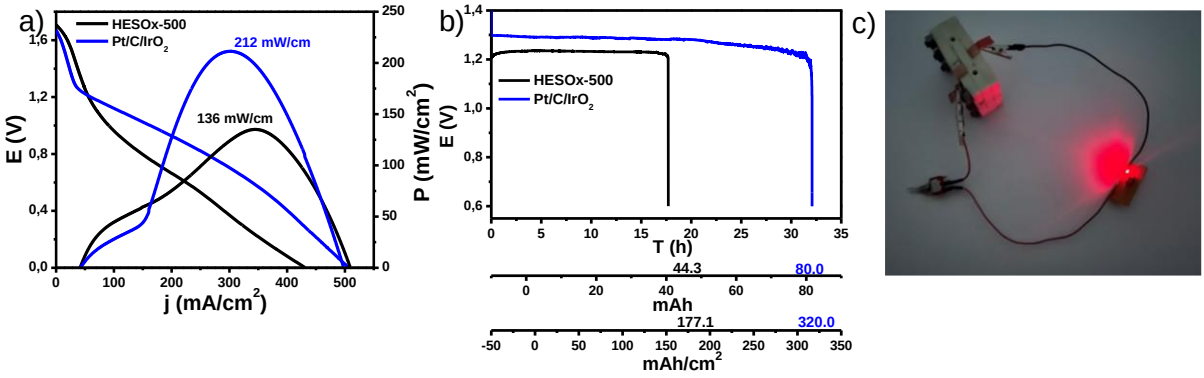

Figure 5.15: HESOx-500 and Pt/C/IrO_2 (a) Peak Power density, (b) galvanostatic discharge curves at a fixed current density of 10 mA/cm^2, and (c) a lit 1.6 V LED of HESOx-500.

Due to its superior ORR and OER catalytic properties, HESOx-500 was used as a cathode electrocatalyst in the fabrication of a RZAB. Figure 5.15a shows the discharge polarisation and power density plots. The OCV of HESOx-500 was recorded at a high of 1.71 V (103% of its theoretical limit of 1.66 V [1]) while that of Pt/C/IrO_2 was 1.67 V. However, the peak power density of Pt/C/IrO_2 (212 mW/cm^2) was much higher than that of HESOx-500 (136 mW/cm^2). When the battery was allowed to fully discharge at 10 mA/cm^2 (Figure 5.15b), both materials showed a relatively stable discharge plateau. HESOx-500 had a steady discharge voltage at 1.23 V up to its termination at 17.70 h (44.3 mAh) and Pt/C/IrO_2 showed a very high discharge voltage of 1.30 V that was maintained for 20.5 h and reduced to 1.22 V upon its death at 32.08 h (80.0 mAh). As a proof-of-concept, one cell of HESOx-500 was used to power a 1.6 V red light emitting diode (LED), which was lit with great brightness (Figure 5.15c).

Furthermore, the material's stability was tested in a parallel plate cell under deep (Figure 5.16a) and shallow (Figure 5.17) cycling. Figure 5.16a shows the deep discharge-charge cycle stability of HESOx-500 and Pt/C/IrO_2 operated at 10 mA/cm^2 at 8 h per cycle. HESOx-500 maintained a long-term cycling to 376 h (47 cycles) while Pt/C/IrO_2 could only run up to 176 h (22 cycles). The discharge-charge voltage gap of HESOx-500 ranged from 0.81 V to 1.17 V. The OER (charge) and ORR (discharge) processes of HESOx-500 showed good reversibility. The HESOx network minimised the undesired elemental segregation and promoted chemical stability of the complex

[20]. In the case of Pt/C/IrO_2 the potential gap started at 0.72 V (first cycle, discharge voltage of 1.30 V) to 0.92 V (second cycle, discharge voltage 1.23 V), which increased to 1.16 V on the fourth cycle (discharge voltage 1.02 V). The performance of Pt/C/IrO_2 was limited by the electrocatalysts which showed a fast ORR performance reduction due to the detachment of Pt from the carbon support and potentially leading to its agglomeration, thus reducing the electroactive surface area needed to effectively carry out ORR. While for OER (charging), IrO_2 showed an unstable plateau profile. When evaluating the material's performance under a shallow galvanostatic discharge-charge profile, a similar response was observable with Pt/C/IrO_2 showing stability of ca. 12 h, and HESOx-500 cycled to 100 h at a potential gap of 0.96 V (Figure 5.17).

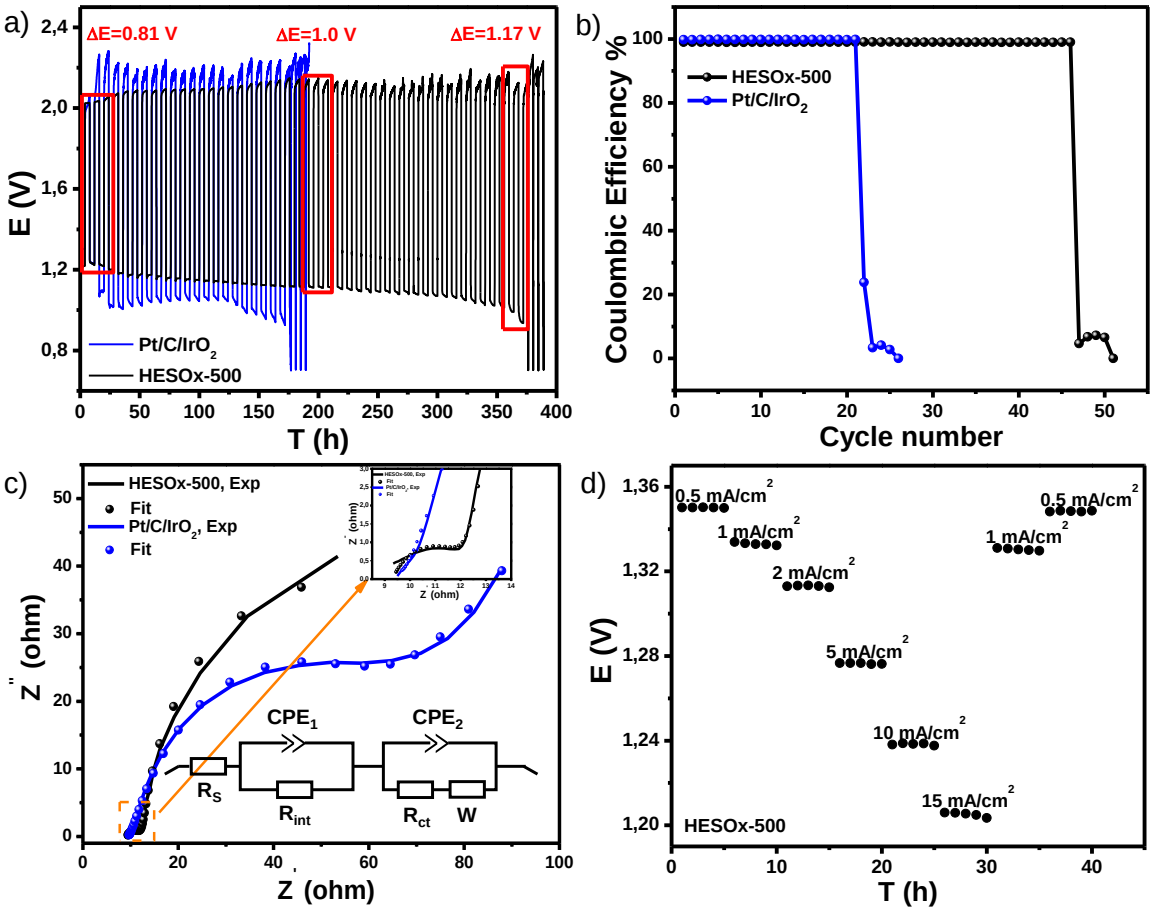

Figure 5.16: HESOx-500 and Pt/C/IrO_2 (a) long-term galvanostatic discharge-charge cycling curves, (b) Coulombic efficiency, (c) Nyquist plots and HESOx-500 (d) change in the discharge voltages at different current densities with time.

A comparison of the outstanding performance of HEM-based cathode materials for RZABs was compared as summarised in Table 5.5. The areal energy of HESOx-500

could be compared to that of a Li-ion battery (35 mWh/cm_{geo}^2 [54]) and its performance outperformed other reported HEMs. A 100% cycle Coulombic efficiency was achieved for both catalysts (Figure 5.16b). EIS was also used to support the good electrocatalytic activity of HESOx-500. The Nyquist plot was fitted with an appropriate circuit and the results summarised in Table 5.6. The catalyst showed the smallest charge transfer resistance (R_{ct}) measured from the Nyquist plots (Figure 5.16c), due to faster interfacial ion transfer kinetics. The improved activity of HESOx-500 was attributed to the high activity of the electrochemical active sites and synergy between Mn, Fe, Co, Cu and Ni. These metals facilitated random d-band hybridisation, which resulted in continuous and broad binding energy distributions, allowing enough adsorption sites for intermediates containing oxygen and eventually favouring the multi-step processes [26]. The rate capability test (Figure 5.16d) was able to recover a relatively stable discharge plateau with an observed returnable voltage from 15 mA/cm^2 to 0.5 mA/cm^2.

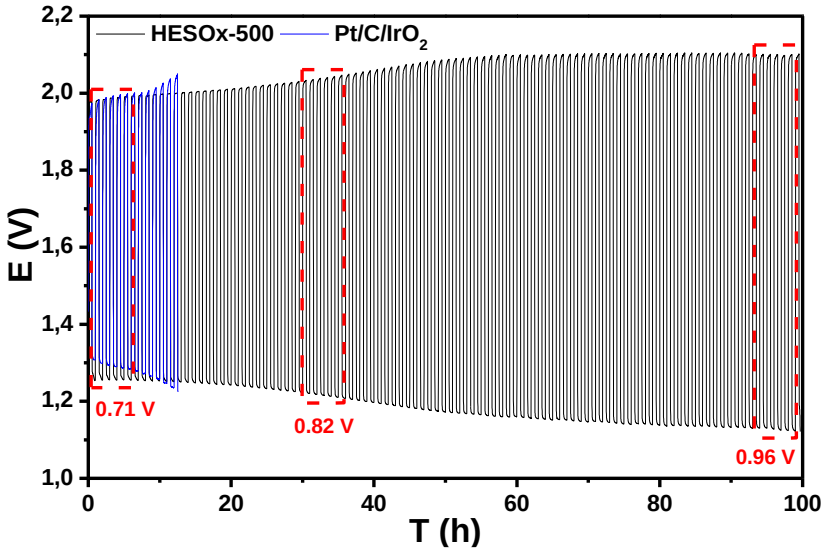

Figure 5.17: Shallow galvanostatic discharge-charge cycles of HESOx-500 and $Pt/C/IrO_2$ at 5 mA/cm^2 for 40 minutes per cycle.

Table 5.5: Electrocatalytical comparison of HEMs for application in RZAB.

Catalyst	Power density (mW/cm^2)	Current density (mA/cm^2)	Discharge time (h)	Areal Energy (mWh/cm^2)	Voltage gap ~ ΔE (V)	Stability	Reference
HESOx-500	136	10 5	4 0.3333	44.4 0.393	0.81 to 1.17 0.73 to 0.97	376h (47 cycles) 100h (300 cycles)	This work
CrMnFeCoNi	116.5	8 5 12	0.1667 0.1667 0.1667	1.4 0.833 2.1	1.05 1.15 0.98	240h (720 cycles) 400h (1200 cycles) 240h (720 cycles)	[24]
FeCoNiMnV HEA/N-CNTs	185.12	5	0.1667	0.917	0.88	566h (1698 cycles)	[26]
AlNiCoFeCrMoV/CoNC	162	2 5 10	0,5	1.2 3 5.5	0.68 to 0.73 0.71 to 0.80 0.81 to 0.89	700h (700 cycles) 140h 140h	[27]
Al-Ni-Co-Ru-Mo-Cr-Fe-Ti	126.8	10	1	11	0.84 to 0.86	300h (150 cycles)	[28]
AlNiCoRuMo	146	2	0.0833	0.2	0.75	500h (3000 cycles)	[29]
		10	0.5	5.25	0.95	ca. 60h	[29]

$Fe_{12}Ni_{23}Cr_{10}Co5_{30}Mn_x$/ CNT	128.6	5	0.0833	0.5	0.77	256h	[30]
FeCoNiMoW	116.9	8	0.1667	1.49	0.90 to 1.12	660h	[31]
CuCoMnNiFe	16.5	5 5	0.0833 0.0833	0.395 0.3	1.1 1.05 to 1.7	26h 88h (1045 cycles)	[32]

Table 5.6: EIS parameters for RZAB.

EIS parameters	HESOx-500	Pt/C/IrO_2
R_s (Ω)	9.31 ± 0.12	9.75 ± 0.12
R_{int} (Ω)	65.43 ± 8.34	1.30 ± 0.77
CPE1 (mF.s^$^{(a-1)}$)	26.77 ± 0.01	0.095 ± 0.04
a	0.66	0.89
R_{ct} (Ω)	2.71 ± 0.10	41.98 ± 0.57
CPE2 (mF.s^$^{(a-1)}$)	2.97 ± 0.36	2.15 ± 0.05
W (Ω.$s^{-1/2}$)	3.41 ± 0.20	29.27 ± 0.49

5.5. Conclusion

In summary, this work developed a promising new approach for fabricating HESOx nanoparticles using modified Pechini method, allowing low-temperature synthesis of HESOx from 500^{o}C to 750^{o}C. The physical characterisation techniques confirmed spherical phase nanoparticles and showed uniform metal distribution from elemental mapping. The entropy stabilisation effect prevented elemental segregation. The low-temperature HESOx-500 showed a higher ECSA than HESOx-750. The materials were further tested for ORR and OER and compared to the Pt/C/IrO_2 standards. The catalytic performance of HESOx-750 was lower compared to HESOx-500 which was given more focus. The observed $E_{1/2}$ (0.88 V), E_{onset} (0.93 V), η_{10} (340 mV) and ΔE (0.69 V) showed excellent response of HESOx-500 compared to Pt/C+IrO_2 ($E_{1/2}$ = 0.78 V, E_{onset} = 0.89 V, η_{10} = 390 mV, ΔE = 0.84 V). In a two-electrode system, the peak power density plot showed an OCV of 1.71 V for HESOx-500 and 1.66 V for Pt/C/IrO_2 and power density of 136 mW/cm^2 and 212 mW/cm^2, respectively. Pt/C/IrO_2 showed an initial high discharge voltage (1.30 V) which degraded to around 1.00 V after the third cycle. The long-term galvanostatic charge-discharge cycled for less than 200 h. The poor performance might be due to the detachment of Pt/C from the support and agglomeration during cycling. While IrO_2 might be subject to dissolution in the highly concentrated electrolyte. However, its long-term galvanostatic discharge-charge cycles and voltage gap fell short to HESOx-500. The catalyst showed excellent long-

term for 374 h of continuous discharge-charge cycling at a current density of 10 mA/cm^2. HESOx-500 demonstrated remarkable stability during cycling, making them a potential alternative to traditional catalysts that suffer from degradation issues. This stability was attributed to the material's structure, which prevented metal separation and maintained oxygen vacancies. However, further research is needed to address the limitations in power density.

5.6. References

[1] A.K. Ipadeola, A.B. Haruna, L. Gaolatlhe, A.K. Lebechi, J. Meng, Q. Pang, K. Eid, A.M. Abdullah, K.I. Ozoemena, Efforts at enhancing bifunctional electrocatalysis and related events for rechargeable zinc-air batteries, ChemElectroChem 8 (2021) 3998–4018. doi.org/10.1002/celc.202100574.

[2] J. Gild, J. Braun, K. Kaufmann, E. Marin, T. Harrington, P. Hopkins, K. Vecchio, J. Luo, A high-entropy silicide: ($Mo_{0.2}Nb_{0.2}Ta_{0.2}Ti_{0.2}W_{0.2}$)$Si_2$, Journal of Materiomics 5 (2019) 337–343. doi.org/10.1016/j.jmat.2019.03.002.

[3] J.-W. Yeh, S.-K. Chen, S.-J. Lin, J.-Y. Gan, T.-S. Chin, T.-T. Shun, C.-H. Tsau, S.-Y. Chang, Nanostructured high-entropy alloys with multiple principal elements: novel alloy design concepts and outcomes, Adv Eng Mater 6 (2004) 299–303. https://doi.org/10.1002/adem.200300567.

[4] A.B. Haruna, E.U. Onoh, K.I. Ozoemena, Emerging high-entropy materials as electrocatalysts for rechargeable zinc–air batteries, Curr Opin Electrochem 39 (2023) 101264. doi.org/10.1016/j.coelec.2023.101264.

[5] C. Oses, C. Toher, S. Curtarolo, High-entropy ceramics, Nat Rev Mater 5 (2020) 295–309. doi.org/10.1038/s41578-019-0170-8.

[6] C.M. Rost, E. Sachet, T. Borman, A. Moballegh, E.C. Dickey, D. Hou, J.L. Jones, S. Curtarolo, J. Maria, Entropy-stabilized oxides, Nat Commun 6 (2015) 8485. doi.org/10.1038/ncomms9485.

[7] N. Dragoe, D. Bérardan, Order emerging from disorder, Science (1979) 366 (2019) 573–574. doi.org/10.1126/science.aaz1598.

[8] E. Krysko, L. Min, Y. Wang, N. Zhang, J.P. Barber, G.E. Niculescu, J.T. Wright, F. Li, K. Burrage, M. Matsuda, R.A. Robinson, Q. Zhang, R. Katzbaer, R. Schaak, M. Terrones, C.M. Rost, Z. Mao, Studies on the structure and the magnetic properties of high-entropy spinel oxide (MgMnFeCoNi)Al_2O_4, APL Mater 11 (2023) 101123. doi.org/10.1063/5.0161401.

[9] T. Jin, X. Sang, R.R. Unocic, R.T. Kinch, X. Liu, J. Hu, H. Liu, S. Dai, Mechanochemical-assisted synthesis of high-entropy metal nitride via a soft urea strategy, Advanced Materials 30 (2018) e1707512. doi.org/10.1002/adma.201707512

[10] J. Gild, Y. Zhang, T. Harrington, S. Jiang, T. Hu, M.C. Quinn, W.M. Mellor, N. Zhou, K. Vecchio, J. Luo, High-Entropy Metal Diborides: A new class of high-entropy materials and a new type of ultrahigh temperature ceramics, Sci Rep 6 (2016) 37946. doi.org/10.1038/srep37946.

[11] F. Monteverde, F. Saraga, M. Gaboardi, J.R. Plaisier, Compositional pathways and anisotropic thermal expansion of high-entropy transition metal diborides, J Eur Ceram Soc 41 (2021) 6255–6266. doi.org/10.1016/j.jeurceramsoc.2021.05.053.

[12] J. Zhou, J. Zhang, F. Zhang, B. Niu, L. Lei, W. Wang, High-entropy carbide: A novel class of multicomponent ceramics, Ceram Int 44 (2018) 22014–22018. doi.org/10.1016/j.ceramint.2018.08.100.

[13] E. Castle, T. Csanádi, S. Grasso, J. Dusza, M. Reece, Processing and properties of high-entropy ultra-high temperature carbides, Sci Rep 8 (2018) 8609. doi.org/10.1038/s41598-018-26827-1.

[14] J. Gild, M. Samiee, J.L. Braun, T. Harrington, H. Vega, P.E. Hopkins, K. Vecchio, J. Luo, High-entropy fluorite oxides, J Eur Ceram Soc 38 (2018) 3578–3584. doi.org/10.1016/j.jeurceramsoc.2018.04.010.

[15] B. Jiang, Y. Yu, J. Cui, X. Liu, L. Xie, J. Liao, Q. Zhang, Y. Huang, S. Ning, B. Jia, B. Zhu, S. Bai, L. Chen, S.J. Pennycook, J. He, High-entropy-stabilized chalcogenides with high thermoelectric performance, Science (1979) 371 (2021) 830–834. doi.org/10.1126/science.abe1292.

[16] K. Chen, R. Zhang, J.-W.G. Bos, M.J. Reece, Synthesis and thermoelectric properties of high-entropy half-Heusler $MFe_{1-x}Co_xSb$ (M = equimolar Ti, Zr, Hf, V, Nb, Ta), J Alloys Compd 892 (2022) 162045. doi.org/10.1016/j.jallcom.2021.162045.

[17] A. Karati, M. Nagini, S. Ghosh, R. Shabadi, K.G. Pradeep, R.C. Mallik, B.S. Murty, U. V. Varadaraju, $Ti_2NiCoSnSb$ - a new half-Heusler type high-entropy alloy showing simultaneous increase in Seebeck coefficient and electrical conductivity for thermoelectric applications, Sci Rep 9 (2019) 5331. doi.org/10.1038/s41598-019-41818-6.

[18] D. Wang, Z. Liu, S. Du, Y. Zhang, H. Li, Z. Xiao, W. Chen, R. Chen, Y. Wang, Y. Zou, S. Wang, Low-temperature synthesis of small-sized high-entropy oxides for water oxidation, J Mater Chem A Mater 7 (2019) 24211–24216. doi.org/10.1039/c9ta08740k.

[19] J.L. Braun, C.M. Rost, M. Lim, A. Giri, D.H. Olson, G.N. Kotsonis, G. Stan, D.W. Brenner, J. Maria, P.E. Hopkins, Charge-induced disorder controls the thermal conductivity of entropy-stabilized oxides, Advanced Materials 30 (2018) 1805004. doi.org/10.1002/adma.201805004.

[20] T. Li, Y. Yao, B.H. Ko, Z. Huang, Q. Dong, J. Gao, W. Chen, J. Li, S. Li, X. Wang, R. Shahbazian-yassar, F. Jiao, L. Hu, Carbon-supported high-entropy oxide nanoparticles as stable electrocatalysts for oxygen reduction reactions, Adv Funct Mater 2010561 (2021) 31. doi.org/10.1002/adfm.202010561.

[21] C. Liu, W. Peng, C.S. Jiang, H. Guo, J. Tao, X. Deng, Z. Chen, Composition and phase structure dependence of mechanical and magnetic properties for AlCoCuFeNi high entropy alloys, J Mater Sci Technol 35 (2019) 1175–1183. doi.org/10.1016/j.jmst.2018.12.014.

[22] Y. Li, H. Dai, Recent advances in zinc-air batteries, Chem Soc Rev 43 (2014) 5257–5275. https://doi.org/10.1039/c4cs00015c.

[23] Z. Jin, X. Zhou, Y. Hu, X. Tang, K. Hu, K.M. Reddy, X. Lin, H.-J. Qiu, A fourteen-component high-entropy alloy@oxide bifunctional electrocatalyst with a record-low ΔE of 0.61 V for highly reversible Zn–air batteries, Chem Sci 13 (2022) 12056–12064. doi.org/10.1039/D2SC04461G.

[24] R. He, L. Yang, Y. Zhang, X. Wang, S. Lee, T. Zhang, L. Li, Z. Liang, J. Chen, J. Li, A. Ostovari Moghaddam, J. Llorca, M. Ibáñez, J. Arbiol, Y. Xu, A. Cabot, A CrMnFeCoNi high entropy alloy boosting oxygen evolution/reduction reactions and zinc-air battery performance, Energy Storage Mater 58 (2023) 287–298. doi.org/10.1016/j.ensm.2023.03.022.

[25] Q. Zhang, K. Lian, Q. Liu, G. Qi, S. Zhang, J. Luo, X. Liu, High entropy alloy nanoparticles as efficient catalysts for alkaline overall seawater splitting and Zn-air batteries, J Colloid Interface Sci 646 (2023) 844–854. doi.org/10.1016/j.jcis.2023.05.074.

[26] D.-H. Wu, M. Ul Haq, L. Zhang, J.-J. Feng, F. Yang, A.-J. Wang, Noble metal-free FeCoNiMnV high entropy alloy anchored on N-doped carbon nanotubes with prominent activity and durability for oxygen reduction and zinc–air batteries, J Colloid Interface Sci 662 (2024) 149–159. doi.org/10.1016/j.jcis.2024.02.044.

[27] T. Yu, H. Xu, Z. Jin, Y. Zhang, H.-J. Qiu, Noble metal-free high-entropy oxide/Co-N-C bifunctional electrocatalyst enables highly reversible and durable Zn-air batteries, Appl Surf Sci 610 (2023) 155624. doi.org/10.1016/j.apsusc.2022.155624

[28] Z. Jin, J. Lyu, K. Hu, Z. Chen, G. Xie, X. Liu, X. Lin, H. Qiu, Eight-component nanoporous high-entropy oxides with low Ru contents as high-performance bifunctional catalysts in Zn-air batteries, Small 18 (2022) 2107207. doi.org/10.1002/smll.202107207.

[29] Z. Jin, J. Lyu, Y.-L. Zhao, H. Li, X. Lin, G. Xie, X. Liu, J.-J. Kai, H.-J. Qiu, Rugged high-entropy alloy nanowires with in situ formed surface spinel oxide as highly stable electrocatalyst in Zn–Air batteries, ACS Mater Lett 2 (2020) 1698–1706. doi.org/10.1021/acsmaterialslett.0c00434.

[30] X. Cao, Y. Gao, Z. Wang, H. Zeng, Y. Song, S. Tang, L. Luo, S. Gong, FeNiCrCoMn high-entropy alloy nanoparticles loaded on carbon nanotubes as bifunctional oxygen catalysts for rechargeable zinc-air batteries, ACS Appl Mater Interfaces 15 (2023) 32365–32375. doi.org/10.1021/acsami.3c04120.

[31] R. He, L. Yang, Y. Zhang, D. Jiang, S. Lee, S. Horta, Z. Liang, X. Lu, A. Ostovari Moghaddam, J. Li, M. Ibáñez, Y. Xu, Y. Zhou, A. Cabot, A 3d-4d-5d High entropy alloy

as a bifunctional oxygen catalyst for robust aqueous zinc–air batteries, Advanced Materials 35 (2023) 2303719. doi.org/10.1002/adma.202303719.

[32] C. Madan, S.R. Jha, N.K. Katiyar, A. Singh, R. Mitra, C.S. Tiwary, K. Biswas, A. Halder, Understanding the evolution of catalytically active multi-metal sites in a bifunctional high-entropy alloy electrocatalyst for zinc–air battery application, Energy Advances 2 (2023) 2055–2068. doi.org/10.1039/D3YA00356F.

[33] M.M. J. Dąbrowa, M. Stygar, A. Mikuła, A. Knapik, K. Mroczka, W. Tejchman, M. Danielewski, Synthesis and microstructure of the $(Co,Cr,Fe,Mn,Ni)_3O_4$ high entropy oxide characterized by spinel structure, Mater Lett (2017). doi.org/10.1016/j.matlet.2017.12.148.

[34] T. Xue, Y. Wang, L. Yang, Z. Li, Y. Gao, Development of quinary layered double hydroxide-derived high-entropy oxides for toluene catalytic removal, Catalysts 13 (2023) 119.

[35] M. Parishani, M. Nadafan, Z. Dehghani, R. Malekfar, G.H.H. Khorrami, Optical and dielectric properties of $NiFe_2O_4$ nanoparticles under different synthesized temperature, Results Phys 7 (2017) 3619–3623. doi.org/10.1016/j.rinp.2017.09.049.

[36] A. Al-Hunaiti, A. Ghazzy, N. Sweidan, Q. Mohaidat, I. Bsoul, S. Mahmood, T. Hussein, Nano-magnetic $NiFe_2O_4$ and its photocatalytic oxidation of vanillyl alcohol—synthesis, characterization, and application in the valorization of lignin, Nanomaterials 11 (2021) 1010. doi.org/10.3390/nano11041010.

[37] P. Priyadharshini, P.A. Shobika, P. Monisha, S.S. Gomathi, K. Pushpanathan, Nickel ferrite magnetic nanoparticles: evidence for superparamagnetism in smaller size particles, Journal of the Australian Ceramic Society 58 (2022) 1455–1480. doi.org/10.1007/s41779-022-00784-5.

[38] T.D. Desissa, M. Meja, D. Andoshe, F. Olu, F. Gochole, G. Bekele, O.A. Zelekew, T. Temesgen, B. Brehane, K.D. Kuffi, T. Hunde, Synthesis and characterizations of (Mg, Co, Ni, Cu, Zn)O high-entropy oxides, SN Appl Sci 3 (2021) 733. doi.org/10.1007/s42452-021-04724-z.

[39] A. Diallo, A.C. Beye, T.B. Doyle, E. Park, M. Maaza, Green synthesis of Co_3O_4 nanoparticles via Aspalathus linearis: Physical properties, Green Chem Lett Rev 8253 (2015) 30–36. doi.org/10.1080/17518253.2015.1082646.

[40] T. Matthews, T.H. Dolla, S.S. Gwebu, T.A. Mashola, L.T. Dlamini, E. Carleschi, P. Ndungu, N.W. Maxakato, Mn-Ni-Co-O spinel oxides towards oxygen reduction reaction in alkaline medium: $Mn_{0.5}Ni_{0.5}Co_2O_4$/C synergism and cooperation, Catalysts 11 (2021) 1059. doi.org/10.3390/catal11091059.

[41] D. McNulty, H. Geaney, C. O'Dwyer, Carbon-coated honeycomb Ni-Mn-Co-O inverse opal: a high capacity ternary transition metal oxide anode for Li-ion batteries, Sci Rep 7 (2017) 42263. doi.org/10.1038/srep42263.

[42] V. D'Ippolito, G.B. Andreozzi, D. Bersani, P.P. Lottici, Raman fingerprint of chromate, aluminate and ferrite spinels, Journal of Raman Spectroscopy 46 (2015) 1255–1264. doi.org/10.1002/jrs.4764.

[43] J.-L. Ortiz-Quiñonez, U. Pal, M.S. Villanueva, Structural, magnetic, and catalytic evaluation of spinel Co, Ni, and Co–Ni ferrite nanoparticles fabricated by low-temperature solution combustion process, ACS Omega 3 (2018) 14986–15001. doi.org/10.1021/acsomega.8b02229.

[44] P. Legutko, J. Pęza, A. Villar, M. Marzec, T. Jakubek, M. Kozieł, Elucidation of unexpectedly weak catalytic effect of doping with cobalt of the cryptomelane and birnessite systems active in soot combustion, Top Catal 62 (2019) 599–610. doi.org/10.1007/s11244-019-01132-x.

[45] R.S. Yadav, I. Kuřitka, J. Vilcakova, J. Havlica, J. Masilko, L. Kalina, J. Tkacz, J. Švec, V. Enev, M. Hajdúchová, Impact of grain size and structural changes on magnetic, dielectric, electrical, impedance and modulus spectroscopic characteristics of $CoFe_2O_4$ nanoparticles synthesized by honey mediated sol-gel combustion method, Advances in Natural Sciences: Nanoscience and Nanotechnology 8 (2017) 045002. doi.org/10.1088/2043-6254/aa853a.

[46] G. Zhang, I. Milisavljevic, K. Grzeszkiewicz, P. Stachowiak, D. Hreniak, Y. Wu, New optical ceramics: High-entropy sesquioxide X_2O_3 multi-wavelength emission phosphor transparent ceramics, J Eur Ceram Soc 41 (2021) 3621–3628. doi.org/10.1016/j.jeurceramsoc.2021.01.027.

[47] M. Thommes, K. Kaneko, A. V. Neimark, J.P. Olivier, F. Rodriguez-Reinoso, J. Rouquerol, K.S.W. Sing, Physisorption of gases, with special reference to the evaluation of surface area and pore size distribution (IUPAC Technical Report), Pure and Applied Chemistry 87 (2015) 1051–1069. doi.org/10.1515/pac-2014-1117.

[48] S. Poulston, P.M. Parlett, P. Stone, M. Bowker, Surface oxidation and reduction of CuO and Cu_2O studied using XPS and XAES, Surface and Interface Analysis 24 (1996) 811–820. doi.org/10.1002/(SICI)1096-9918(199611)24:12<811::AID-SIA191>3.0.CO;2-Z.

[49] J. Soo Kang, M.-A. Park, J.-Y. Kim, S. Ha Park, D. Young Chung, S.-H. Yu, J. Kim, J. Park, J.-W. Choi, K. Jae Lee, J. Jeong, M. Jae Ko, K.-S. Ahn, Y.-E. Sung, Reactively sputtered nickel nitride as electrocatalytic counter electrode for dye- and quantum dot-sensitized solar cells, Sci Rep 5 (2015) 10450. doi.org/10.1038/srep10450.

[50] Y. Lu, W. Zhan, Y. He, Y. Wang, X. Kong, Q. Kuang, Z. Xie, MOF-templated synthesis of porous Co_3O_4 concave nanocubes with high specific surface area and their gas sensing properties, Applied Materials and Interfaces 6 (2014) 4186−4195.

[51] W.T. Hong, M. Risch, K.A. Stoerzinger, A. Grimaud, J. Suntivich, Y. Shao-Horn, Toward the rational design of non-precious transition metal oxides for oxygen electrocatalysis, Energy Environ Sci 8 (2015) 1404–1427. doi.org/10.1039/C4EE03869J

[52] H. Lan, X. Chen, P. Fan, G. Liang, Inorganic and lead-free $CsBi_3I_{10}$ thin-film solar cell prepared by single-source thermal evaporation, Journal of Materials Science: Materials in Electronics 32 (2021) 11183–11192. doi.org/10.1007/s10854-021-05783-z.

[53] A.R. Lopes da Silva, A. Jhones dos Santos, C.A. Martínez-Huitle, Electrochemical measurements and theoretical studies for understanding the behavior of catechol, resorcinol and hydroquinone on the boron doped diamond surface, RSC Adv 8 (2018) 3483–3492. doi.org/10.1039/C7RA12257H.

[54] B.J. Hopkins, C.N. Chervin, J.F. Parker, J.W. Long, D.R. Rolison, An areal-energy standard to validate air breathing electrodes for rechargeable zinc-air batteries, Adv Energy Mater 10 (2020) 2001287. doi.org/10.1002/aenm.202001287.

CHAPTER 6

POLYMER-COATED ZINC OXIDE: A PROMISING ANODE MATERIAL FOR NEXT-GENERATION RECHARGEABLE ZINC-AIR BATTERIES

6.1. Introduction

Zn-air battery is a potential power source and energy storage device. Zinc anode is chemically stable in aqueous solutions as it can sustain several cycles during its earlier life cycles. However, the solid-solute-solid mechanism (Zn-$Zn(OH)_4^{2-}$-ZnO) of rechargeable Zn-air batteries is known to limit its reversibility. The majority of zinc-air battery research is focused on improving the bifunctionality of the cathode materials that are produced with methods that are environmentally friendly and at a low cost [1,2]. Thus, the performance of Zn-air batteries is no longer constrained by the air electrodes due to the extensive research efforts on cathode electrocatalysts, some also studied in Chapter 4 and 5 of this Thesis. Nonetheless, other unresolved concerns for secondary zinc-air batteries persist, notably with regard to cycle life and longevity. Major problems include passivation caused by zinc oxide (ZnO) precipitation, formation of dendrite, carbonate formation, and hydrogen gas evolution which bring about zinc corrosion during cycling, premature cell death, and poor cycle life.

Other downside effects include the reduction of zincate ion solubility, reduced electrolyte conductivity, and hydroxide concentration and capacity fade. This pushes the need to rethink the design of the zinc anode structure to help effectively facilitate the reaction mechanism in order to control the zinc oxidation during discharge and reduction during charging. The exploration of zinc sponge, zinc foam, alloyed zinc, and coated zinc oxide have been explored. Zinc oxide nanoparticles coated with carbon shell have demonstrated significant application potential among the other explored approaches. This is because the coating offers several advantages: it can suppress the hydrogen overpotential, slow down corrosion of the zinc oxide, and maintain the particle's shape during use. The coating works in several ways; it prevents ZnO from dissolving, increases the base material conductivity, and causes a symmetrical dispersion of electrons on the ZnO particle surface, reduces the contact surface between the carbon material and ZnO, which inhibits dendrite development to some extent [3].

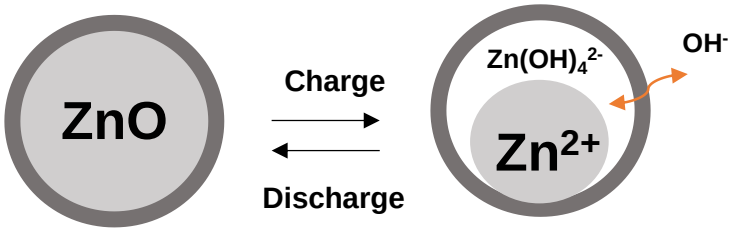

Scheme 6.1: Schematic illustration of ZnO to Zn^{2+} pathway with a coated carbon shell, with a primary function of encapsulating zincate ions while allowing the passage of hydroxide ions.

As seen in scheme 6.1, coating helps to ensure electrochemical accessibility and rechargeability of active Zn^{2+} species, by trapping formed zincate ions within the shell to prevent the supersaturation of passive ZnO layers. Further facilitating OH^- ions through the amorphous carbon network [4]. Its electrochemical processes can be represented by equations 6.1 to 6.4:

Charge: $ZnO + 2OH^- + H_2O \rightarrow Zn(OH)_4^{2-}$ (6.1)

$Zn(OH)_4^{2-} + 2e^- \rightarrow Zn + 4OH^-$ (6.2)

Discharge: $Zn + 4OH^- \rightarrow Zn(OH)_2 + 2e^-$ (6.3)

$Zn(OH)_4^{2-} \rightarrow ZnO + 2OH^- + H_2O$ (6.4)

A large number of coating materials, such as metal oxides, polymers, or carbon, have been tested to avoid electrode shape change phenomena and increase the use and retention of the active material [5,6]. Zhang et al. used PDA coating as a strategy for interfacial interaction enhancement and as a platform for further metal coating [7]. The thickness of PDA could be controlled by varying the concentration of dopamine [8]. In this work, ZnO was used due to its ability to form Zn^{2+} pathways. The oxide was coated to help prevent or minimise the effect of corrosion. Polydopamine (PDA) coating was used due to its ability to adhere to a wide range of organic and inorganic substrates of different morphologies. The thin layers of polydopamine are formed by the oxidative self-polymerisation of dopamine. The reaction process uses mild reaction conditions and the coating is a versatile platform for subsequent reactions, to further enhance surface activity or functionality [9]. The possible reaction mechanism of dopamine is the oxidation of catechol to benzoquinone which further oxidises to melanin resulting

in the formation of polydopamine (PDA) [9]. PDA is known to exhibit excellent adsorption ability, high hydrophilicity, good mechanical properties, good chemical reactivity electromagnetic interface shielding [7,8]. The PDA coating is assumed to efficiently prevent the movement of corrosion ions in the corrosion system [10]. In order to examine the degradation of ZnO and the impact of the coating materials, open circuit potential (OCP), linear polarisation resistance (LPR), charge and discharge processes were applied. Improvements in electrochemical performance were investigated by comparing the outcomes of coated zinc particles to non-modified particulate zinc that were cycled under identical conditions. Complete discharge and charge phases were used to explore the degradation of zinc at maximum utilisation and to highlight the influence of the coating.

6.2. Experiment

6.2.1. Materials and reagents

All the reagents were of analytical grade and used without further purification. The reagents included zinc acetate dehydrate, Tris-buffer (pH 8.5), dopamine hydrochloride, sodium hydroxide (NaOH), 5% Nafion resin, isopropanol, potassium hydroxide (KOH), potassium ferricyanide, potassium ferrocyanide, potassium chloride, carbon black, polytetrafluoroethylene, carbon paper, copper strip, and zinc plate.

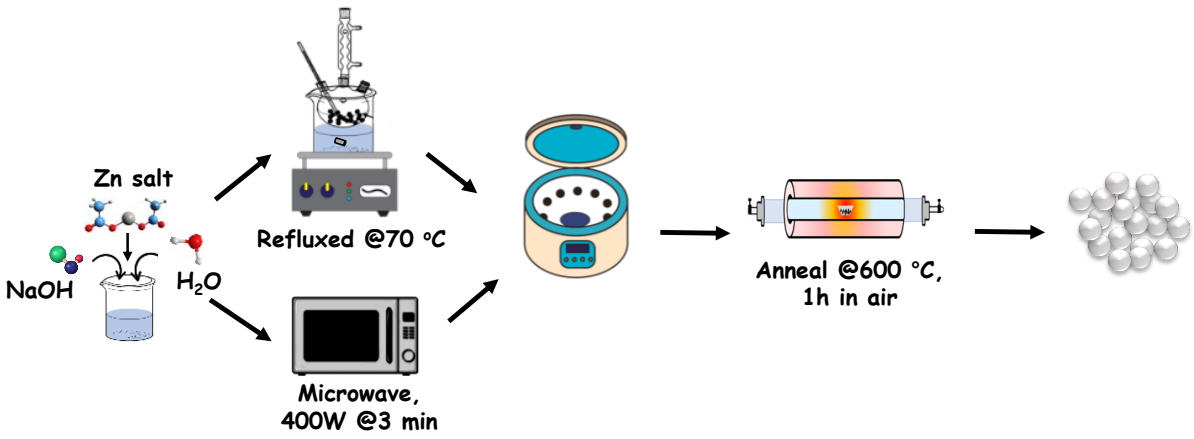

Scheme 6.2: The schematic synthesis illustration of the synthesis of ZnO_I and ZnO_{mw}.

6.2.2. Synthesis of ZnO

ZnO was prepared by a method by Devaraj et al.[11] with a slight modification. As illustrated in Scheme 6.2, 10.975 g of zinc acetate dihydrate was dissolved in 50 mL of DI water. Followed by dissolving 2.0 g NaOH in 50 mL DI water. Then the NaOH solution was added dropwise to the zinc acetate solution and stirred at 1500 rev/min for 2 hours at 70 ^{o}C to form a white precipitate. The precipitate was then collected by vacuum filtration followed by washing with DI water and ethanol several times, followed by drying in an oven at 60 ^{o}C overnight. The white product was annealed at 600 ^{o}C for 1 h in air.

6.2.3. Synthesis of ZnO by microwave

The synthesis followed a similar synthesis route as that in 6.2.2 (see Scheme 6.2, alternative synthesis pathway). However, after mixing the acetate and NaOH solutions, the mixture was exposed to microwave irradiation for 3 min at 400 W to a form white precipitate.

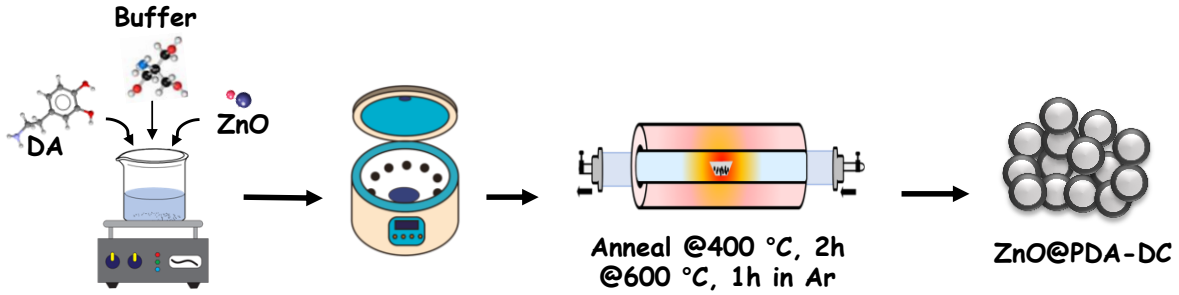

Scheme 6.3: The schematic synthesis illustration of the synthesis of coated ZnO.

6.2.4. Synthesis of coated ZnO@PDA-DC

The synthesis (Scheme 6.3) was done following the work done by Wu et al. [12] with slight modifications. 100 mg of ZnO (ZnO_l or ZnO_{mw} or ZnO_c (<100 nm particle size obtained from Sigma) nanoparticles was dispersed into 100 mL DI water followed by sonicating for 10 minutes, then 1 mL of Tris-buffer (pH 8.5) and 2:1 mass ratio of dopamine hydrochloride was added and then stirred for 24 hours. The resulting solution was collected and washed with DI water two times in the centrifuge and dried overnight. Then the sample was heated in a tube furnace under Ar gas to 400 °C at a

rate of 1 °C/min and maintained for two hours, thereafter the furnace was ramped to 600 °C with a rate of 5 °C/min for one hour. The black powder obtained at the end of the reaction was polydopamine-coated ZnO nanoparticles, where ZnO_c, ZnO_l and ZnO_{mw} were used to represent commercial, conventional and microwave synthesis approaches. ZnO and ZnO@PDA-DC are used as general expressions for the materials prepared.

6.2.5. Physical Characterisation

Several characterisation techniques were used to study the composition, structure, and behaviour of the synthesised materials. These techniques include P-XRD, SEM, EDS, TEM, BET, FT-IR and TGA.

6.2.6. Electrode Fabrication and Electrochemical Measurements

The catalyst's ink was made by dispersing the sample in a 1:9 water and isopropanol solution with Nafion and sonicated for ~30 minutes. Thereafter, 20 µL the prepared catalyst ink was drop-casted on the polished RDE and dried in air, obtaining a loading of 0.2 ± 0.02 mg/cm^2. This was followed by conducting the open circuit potential (OCP), hydrogen evolution reactions (HER), linear polarisation resistance (LPR), and electrochemical impedance spectroscopy (EIS) in 6 M KOH. A GCE electrode was used for studies conducted in ferri-ferrocyanide solution.

6.2.7. Zinc-air battery assembly

A conducting material (carbon black (CB)) with ZnO@PDA-DC active material (1:9) was used as an anode electrocatalyst. The RZAB was fabricated with a micro-3D printed cell that comprises of a polished zinc plate as anode, a catalyst slurry on carbon paper as a bifunctional air electrocatalyst (HESOx-500 was used due to its outstanding OER/ORR and RZAB responses detailed in Chapter 5) and copper strip as a current collector. The preparation of the slurry followed the same method outlined in Chapter 3 subsection 3.4.2. A solution of 6.0 M KOH and 0.2 M zinc acetate was used as the electrolyte.

6.3. Results and Discussion

6.3.1. Physical characterisation

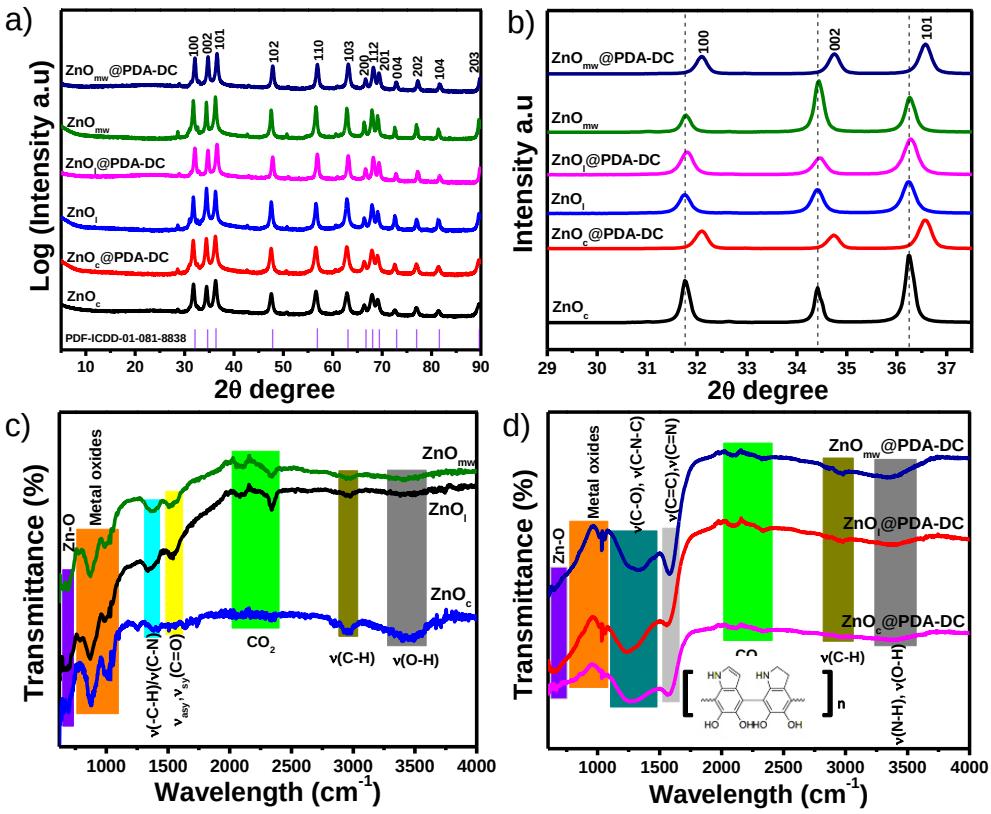

Figure 6.1: Powder XRD of ZnO and ZnO@PDA-DC showing (a) enhanced plots and (b) expanded plots to show the shift in the spectra powder XRD and (c & d) FT-IR.

The P-XRD was used to determine the crystalline nature of the materials. The P-XRD patterns were collected from 5-90 2θ degrees and shown in Figure 6.1(a &b). The studied ZnO and ZnO@PDA-DC were indexed to the powder diffraction file (PDF) card no 01-081-8838 (Figure 6.1a). The material was identical to the hexagonal phase of ZnO with a P63mc space group. In Figure 6.1a, the logarithmic intensity was used to enhance the spectra. The presence of the carbon coating was evidenced by a carbon peak at around 23 2θ degrees for ZnO@PDA-DC materials. There was an observed shift in the P-XRD spectra of ZnO@PDA-DC (Figure 6.1b) to higher 2θ degrees due to compressive residual stress. FT-IR was used as a complementary technique to P-XRD. FT-IR spectroscopy is often used to directly identify chemical functional groups within a sample. The functional groups in ZnO and ZnO@PDA-DC were identified from

FT-IR, recorded in the range 4000-500 cm^{-1}. The presence of the metal oxides in Figure 6.1c could be evidenced by the vibration modes at 646.8-726.4 cm^{-1} (Zn-O) and 761.4-1099.4 cm^{-1} (metal-oxides) [13]. Other vibrational modes observed were C-H and C-N (1313.9-1429.3 cm^{-1}), C=O (1479.6-1616.9 cm^{-1}) CO_2 (2020.8-2392.1 cm^{-1}), C-H (2883.6-3034.8 cm^{-1}) and O-H (3284.2-3595.4 cm^{-1}). This was a result of the reaction intermediates or small residues of zinc acetate used for the synthesis of ZnO nanoparticles [14]. In Figure 6.1d, the coated ZnO had a stretching vibration at 3231.0-3574.8 cm^{-1} due to the appearance of hydroxyl (O-H) and amine (N-H) groups of the catechol in polydopamine [15]. The peak at 1099.6-1476.2 cm^{-1} was assigned to the vibration of C-O [15]. The peaks at 1524.8-1657.1 cm^{-1} were due to the aromatic ring and vibration of the amide N-H group [16]. The presence of these groups confirmed the coating of ZnO with PDA.

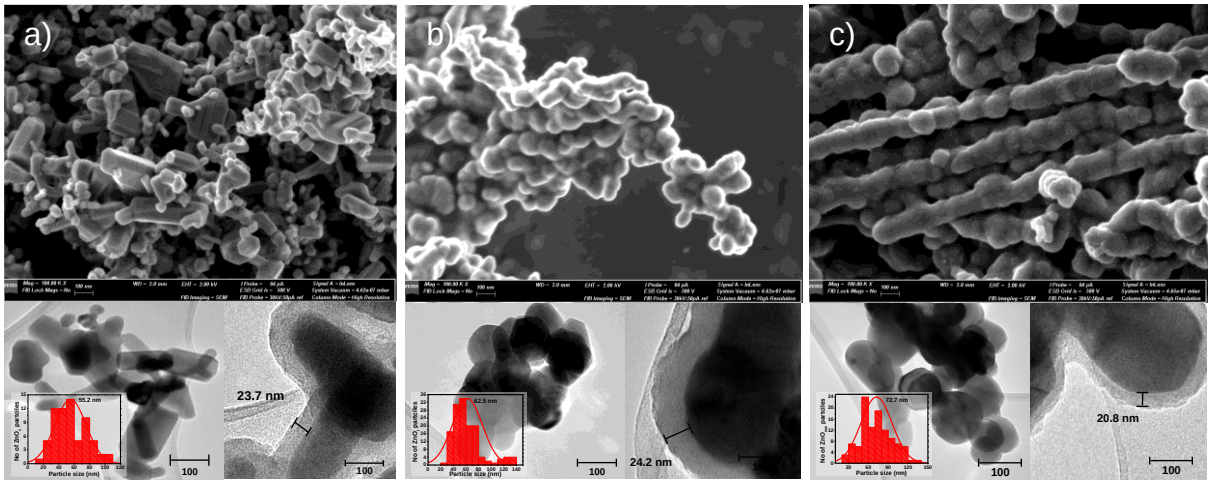

Figure 6.2: SEM and TEM images of (a) ZnO_c and ZnO_c@PDA-DC, (b) ZnO_l and ZnO_l@PDA-DC and (c) ZnO_{mw} and ZnO_{mw}@PDA-DC.

The SEM and TEM images of ZnO and ZnO@PDA-DC are shown in Figure 6.2. The TEM images of ZnO compared to ZnO@PDA-DC, showed darker spherical nanoparticles surrounded by a lighter outer shell which indicated the successful coating of ZnO with PDA. The boundary was very clear indicating a tight encapsulation of the metal oxide [17]. The SEM image in Figure 6.2a showed ZnO_c to have a mixed morphology of nanoparticles consisting of two- and three-dimensional spheres, hexagonal and other shapes. Its TEM image also showed its mixed morphology with an estimated average particle size of 55.2 $\pm$ 0.3 nm. The confirmed coating can be seen with an estimated coating thickness of 23.7 $\pm$ 0.4 nm. The SEM images of ZnO_l

(Figure 6.2b) and ZnO_{mw} (Figure 6.2c) showed a dominance of spherical morphology also seen from TEM images. The average particle size of ZnO_{l} was 62.5 ± 0.4 nm and that of ZnO_{mw} was 72.7 ± 0.8 nm, with a coating thickness of 24.2 ± 0.6 nm and 20.8 ± 0.6 nm, respectively.

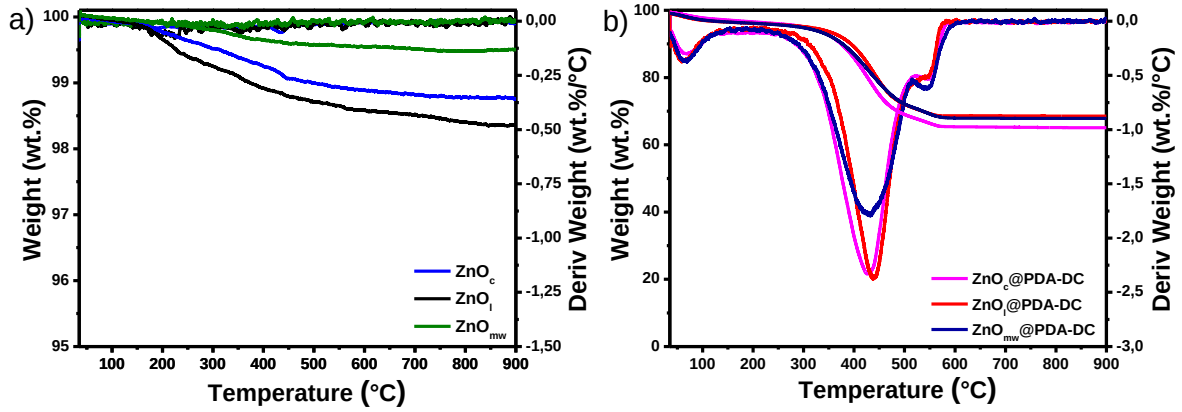

Figure 6.3: TGA analysis and derivative curves of (a) ZnO_c, ZnO_l and ZnO_{mw} (b) ZnO_c@PDA-DA, ZnO_l@PDA-DA and ZnO_{mw}@PDA-DA.

The sample weight of the samples was monitored using TGA in Figure 6.3. TGA and derivative thermogravimetric (DTG) curves of pristine metal oxides showed a degradation step at around 170 °C to 180 °C with mass loss of 1.22% (ZnO_c), 1.64% (ZnO_l) and 0.52% (ZnO_{mw}) at 800 °C shown in Figure 6.3a. While the coated metal oxides shown in Figure 6.3b show decomposition signatures associated with polydopamine. Three decomposition stages were observed on the TGA and the corresponding DTG. The first decomposition was observed at 35-120 °C associated with the evaporation of weak bonds of water, little alcohols and lipids in the raw material. The maximum temperature was 65.8 °C (ZnO_c@PDA-DC), 60.3 °C (ZnO_l@PDA-DC) and 65.2 °C (ZnO_{mw}@PDA-DC) with a weight loss of 2.14%, 2.89% and 2.76%, respectively. The small weight loss was due to the strong chemically bound water [18]. The second decomposition step was due to the removal of side hydroxyl groups and partial chain scission. The third decomposition temperature was associated with the decomposition of the polymer backbone [18]. The residual weight loss percentage at 800 °C followed the order ZnO_l@PDA-DC (31.5%) < ZnO_{mw}@PDA-DC (32.2%) < ZnO_c@PDA-DC (34.6%).

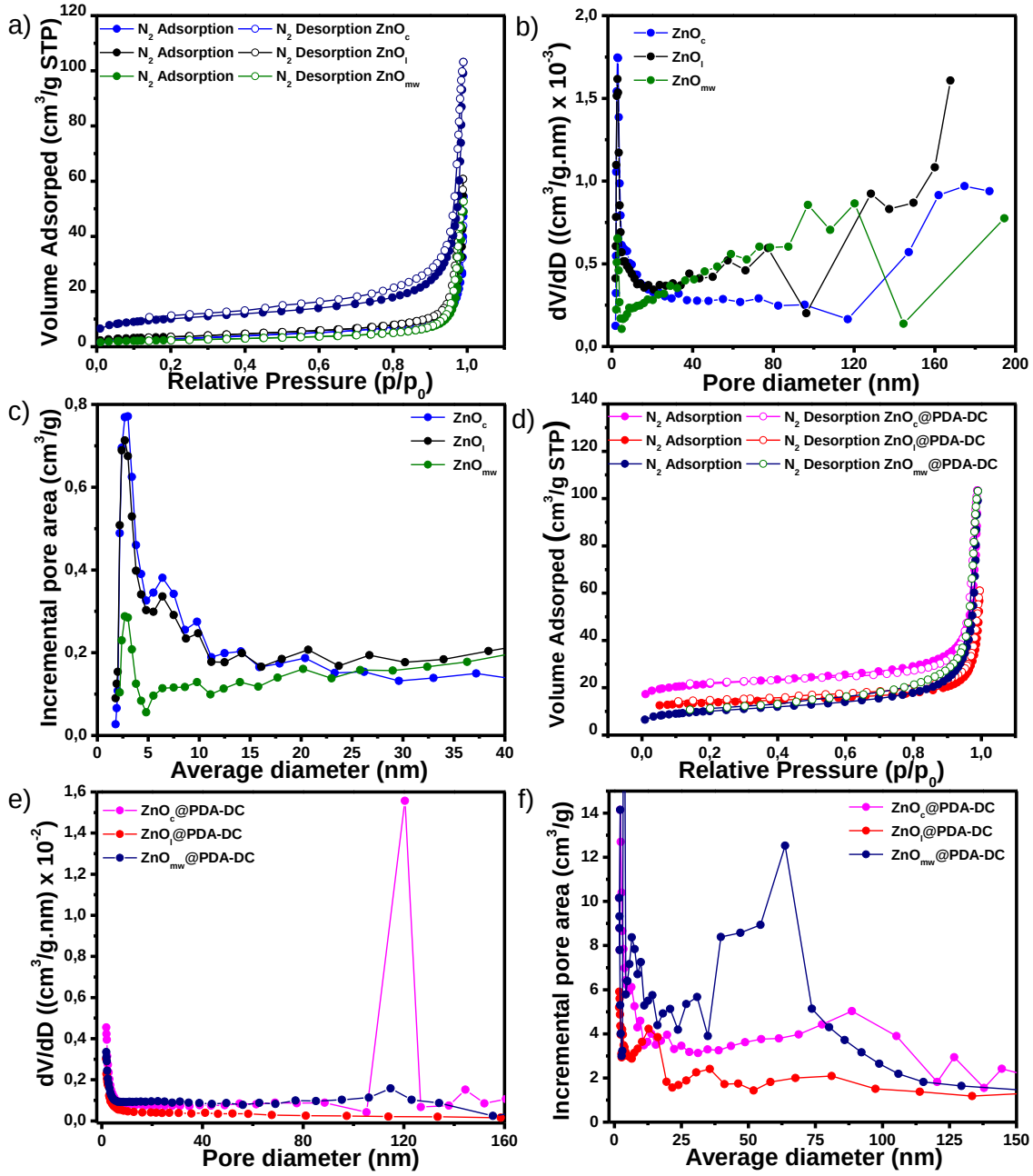

Figure 6.4: (a & d) BET adsorption-desorption isotherm plots, (c & e) average pore volume, and (d & f) incremental average pore area of ZnO and ZnO@PDA-DC, respectively.

The specific surface area of bare ZnO and its coated counterparts were examined from BET analysis through the adsorption-desorption of N_2 (Figure 6.4(a & b)). The average pore volume and pore sizes of the samples were also obtained in Figure 6.4(b, c, e & f). The data was summarised in Table 6.1. The BET surface area calculated using the standard multi-point BET method showed an increase of over double its initial value upon coating following the order ZnO_c@PDA-DC (70.58 m^2/g)

< ZnO_l@PDA-DC (47.93 m^2/g) < ZnO_{mw}@PDA-DC (34.43 m^2/g). As anticipated, the trend of surface area was in support of TEM estimated nanoparticle distribution, where smaller particle-sized materials result in higher surface area. The adsorption isotherms of the pristine metal oxides (Figure 6.4a) and the coated materials (Figure 6.4d) displayed type IV hysteresis loops, confirming the presence of mesoporous structures. The incremental pore area of the materials (Figure 6.4(c & f)) also supported the presence of mesoporous structures.

Table 6.1: Nitrogen gas adsorption analysis of ZnO and ZnO@PDA-DC.

Catalyst	BET surface area (m^2/g)	Pore volume (cm^3/g)	Pore size (nm)
ZnO_c	10.39	0.085	30.24
ZnO_c@PDA-DC	70.58	0.135	25.43
ZnO_l	12.61	0.093	33.96
ZnO_l@PDA-DC	47.93	0.072	23.86
ZnO_{mw}	8.08	0.08	48.37
ZnO_{mw}@PDA-DC	34.43	0.15	29.58

6.3.2. Electrochemical measurements

Scan rate studies (Figure 6.5) were conducted for the materials under study to investigate the response of the coated materials. As anticipated the current response of ZnO@PDA-DC increased with an increase in scan rate. The C_{dl} of ZnO_c (77.83 mF/cm^2) was the second highest to ZnO_{mw} (82.84 mF/cm^2), indicating the presence of more active species in 6 M KOH (Figure 6.5g). The opposite was observed for ZnO_l@PDA-DC which had the lowest C_{dl} at 15.62 mF/cm^2 for anodic response current, this was due to the suppression of active material by the protective film. The electrochemical behaviour of the materials was examined in an electrochemically reversible redox system (potassium ferricyanide-ferrocyanide of 3 mM in 0.1 M KCl) using cyclic voltammetry (CV). The materials were unable to reduce and oxidise the

probe as seen in Figure 6.6(a & b). However, the pristine samples showed a reduction of the metal oxide at around 0.63 V to 0.67 V (Figure 6.6a). The coated materials showed improved current response with a suppression of the metal oxide reduction, where the ZnO_I@PDA-DC showed 10 times the response in comparison to the studied materials.

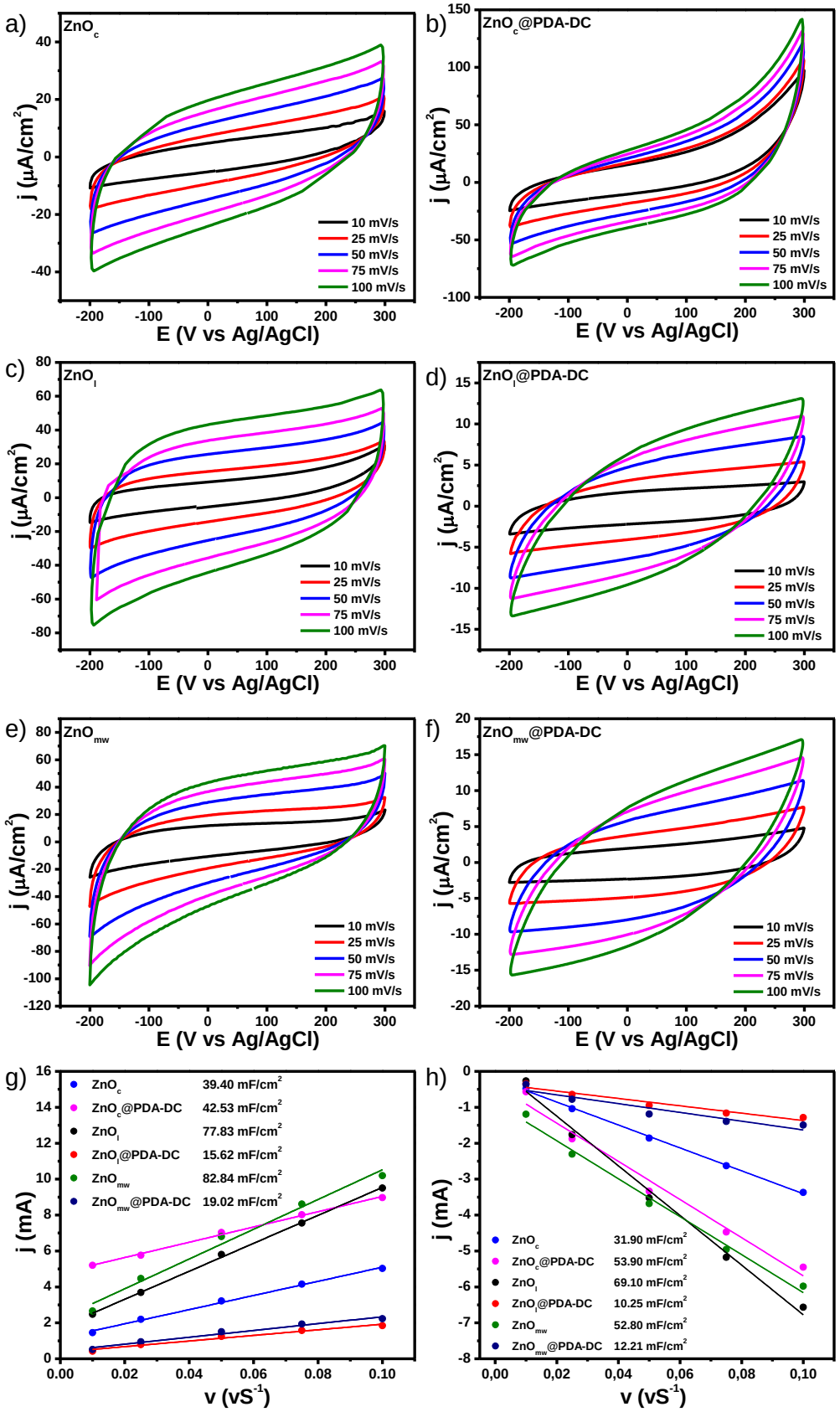

Figure 6.5: Cyclic voltammograms of (a) ZnO_c, (b) ZnO_c@PDA-DC, (c) ZnO_l, (d) ZnO_l@PDA-DC, (e) ZnO_{mw}, (f) ZnO_{mw}@PDA-DC, (g) anodic and (h) cathodic C_{dl} of ZnO and ZnO@PDA-DC at different scan rate in 6 M KOH.

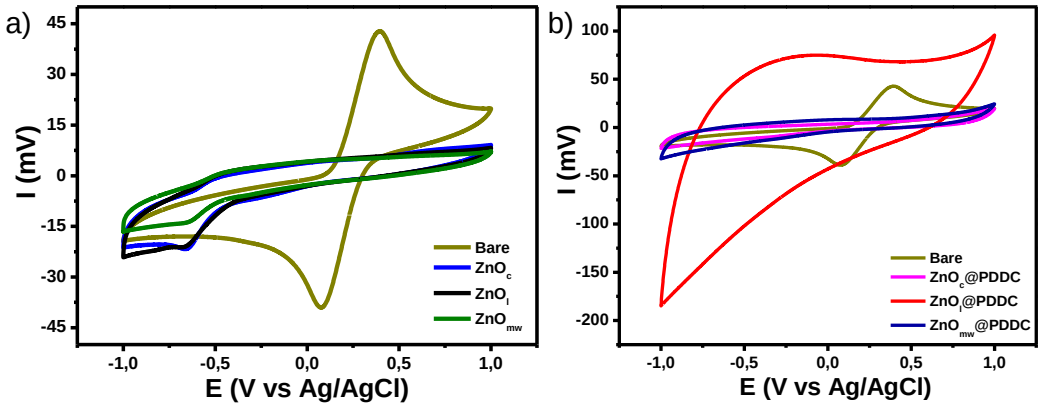

Figure 6.6: Cyclic voltammograms of (a) ZnO and (b) ZnO@PDA-DC in redox probe.

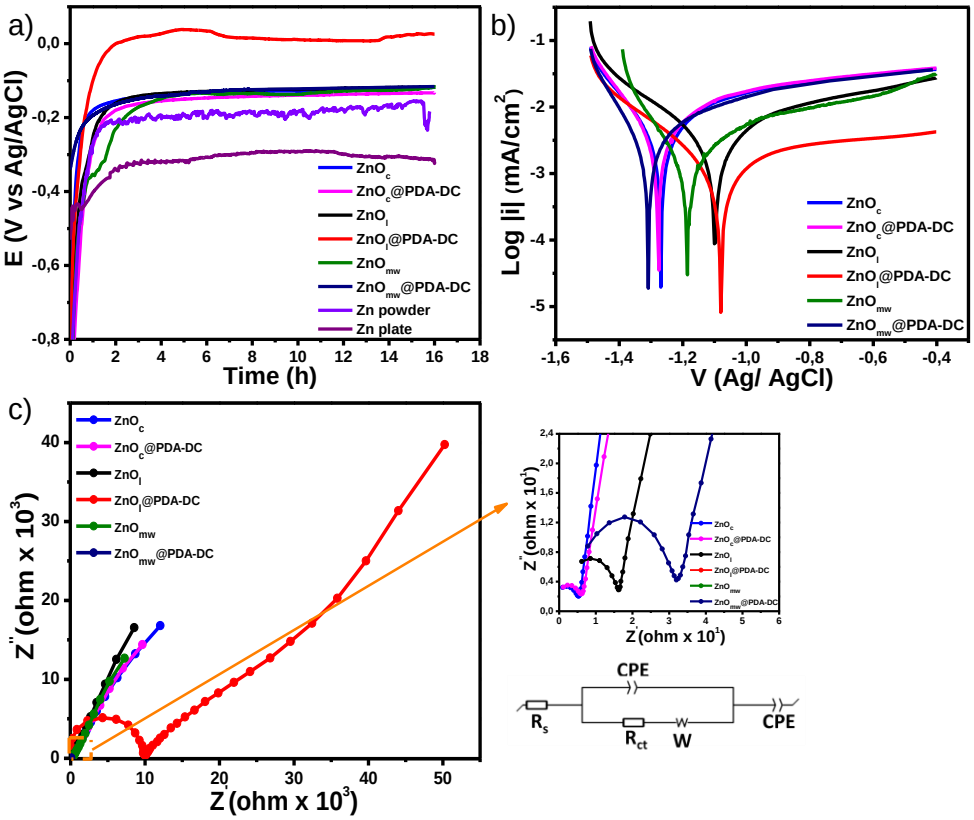

Figure 6.7: The OCP of (a) ZnO, ZnO@PDA-DC, Zn plate and Zn powder, (b) dynamic-potential polarization curves of ZnO and Zn@PDA-DC at 1 mV/s in 6 M KOH, and (c) the Nyquist curves of ZnO and ZnO@PDA-DC at i_{corr}.

The coating's effectiveness in protecting the zinc oxide was investigated by exposing the electrocatalyst in 6 M KOH in Figure 6.7a. The accelerated tests can used to rapidly assess and predict the material's ability to reduce hydrogen evolution and dissolution of zinc. This is because, when an electrode is submerged in an electrolyte, it adopts an open circuit potential (OCP), which specifies the equilibrium between

oxidation and reduction processes on the electrode [19]. OCP also called free corrosion potential is the potential difference that is measured between the working and reference electrodes [20]. This potential can fluctuate over time due to changes in the nature of the surface of the tested material (oxidation and development of a passive layer or activation and reduction that start corrosion) and can be used as a criterion for corrosion behaviour [19]. It shows a voltage change of less than ± 5 mV/s across time showing equilibrium and stability, making it suitable for perturbation-based experiments such as LPR [19].

The electrodes were (ZnO, ZnO@PDA-DC, Zn plate, Zn powder) firstly monitored for 180 s before starting the measurement. The electrodes were then fully stabilized by recording its open-OCP for 16 h (Figure 6.7a). The studied surfaces show a positive potential shift which indicates the formation or presence of a protective film. The initial increase in the voltage was due to the diffusion of the electrolyte on the electrolyte interface, which later reached a stable OCP value. The order of OCP response followed ZnO_l@PDA-DC > ZnO_{mw}@PDA-DC > ZnO_l > ZnO_c > ZnO_{mw} > ZnO_c@PDA-DC > zinc powder > zinc plate. Figure 6.4c shows ZnO_l@PDA-DC to exhibit a more positive shift, indicating a better barrier effect introduced by the thin film. This indicates that there was ion restriction on the surface of ZnO_l@PDA-DC than on the other studied electrocatalysts. When the electrolyte parameters are properly maintained, the OCP of a coated material reflects how well it can survive unfavourable environmental effects with passivation [21]. The more noble ZnO_l@PDA-DC potential value indicated that the thin film coating had the ability to reduce the aggressiveness of high molar KOH. If the shift is positive the partial anodic reaction predominates and the partial cathodic reaction may be neglected when it is in the opposite direction the cathodic reaction predominates [22]. This meant that the dominant reaction on ZnO_l@PDA-DC was anodic.

To corroborate OCP, linear polarization resistance (LPR) tests were performed by polarizing the working electrode ± 10 mV with respect to the OCP at a scan rate of 1.0 mV/s (Figure 6.7b). The Tafel plots in Figure 6.7b were extrapolated to determine the E_{corr} (corrosion potential), i_{corr} (corrosion current density), anodic and cathodic slopes (b_a and b_c, respectively), polarisation resistance (R_p), and the corrosion protection efficiency (CPE) of the zinc-based materials under study. The reaction parameters

from LPR are summarised in Table 6.2. In the case where a metal undergoes corrosion, polarisation resistance (R_p) is considered which is the combination of film resistance (R_f), diffusion layer resistance (R_d), and the resistance from other accumulations (R_a) [23]. The polarisation resistance was calculated using the Sterm-Geary equation:

$$R_p = \frac{b_c b_a}{2.3 i_{corr}(b_c + b_a)} \quad (6.5)$$

where b_a and b_c are Tafel anodic and cathodic slopes respectively.

The CPE was used to compare the protective effects of coating using equation 6.6:

$$CPE\% = \left|\frac{I^0_{corr} - I^c_{corr}}{I^0_{corr}}\right| \times 100\% \quad (6.6)$$

where I^o_{corr} is the corrosion current of the uncoated material, and I^c_{corr} is the corrosion current of the coated material.

Table 6.2: Comparative table for LPR extracted parameters for studied electrocatalysts.

Catalyst	E_{corr} (V)	i_{corr} (μA/cm^2)	b_a (V)	b_c (V)	R_p (Ω cm^2)	CPE%
ZnO_c	- 1.269	0.577	0.153	0.121	18 044.45	-
ZnO_c@PDA-DC	-1.278	0.460	0.167	0.121	15 971. 59	20.28
ZnO_l	-1.099	0.412	0.136	0.122	29 840.88	-
ZnO_l@PDA-DC	-1.079	0.107	0.147	0.121	80 829.87	74.03
ZnO_{mw}	-1.183	0.616	0.155	0.122	31 112.55	-
ZnO_{mw}@PDA-DC	-1.308	0.475	0.169	0.120	37 026.71	22.89

The ZnO_l@PDA-DC and ZnO showed anodic and cathodic curves with nearly parallel lines, indicating that there was no change in either the anodic or cathodic reaction mechanisms. The shift in the E_{corr} of the ZnO_l@PDA-DC materials with respect to the pristine (ZnO) materials can be classified as either anodic-type, cathodic-type, or mixed inhibition. Anodic-type inhibition is suggested by a E_{corr} shift of magnitude >85 mV in the positive direction relative to the blank, while cathodic-type inhibition is indicated by a shift of magnitude >85 mV in the negative direction [23]. Mixed corrosion

inhibition is defined as a shift in each direction of less than 85 mV [23]. Hydrogen evolution reaction happens solely as a cathodic process, a shift towards the left is a preference towards its inhibition. While an anodic shift indicates a preference for the prevention of metal dissolution. Hydrogen evolution was not observed for all the electrocatalysts under study (Figure 6.8). In Figure 6.7b, the anodic and cathodic reactions (represented by b_c and b_a) of ZnO_l@PDA-DC in relation to ZnO_l showed a decrease in current density indicating a reduction in corrosion active areas [24]. ZnO_{mw}@PDA-DC only showed a cathodic current reduction, while ZnO_c@PDA-DC showed a higher anodic and cathodic current response to its parent material. The E_{corr} magnitude shift of ZnO_c@PDA-DC (10 mV) and ZnO_l@PDA-DC (16 mV) were less than 85 mV indicating a mixed inhibition. ZnO_l@PDA-DC had a positive shift and ZnO_l@PDA-DC showed a slight negative shift, indicating an anodic and cathodic favoured reaction, respectively. ZnO_{mw}@PDA-DC showed a greater E_{corr} (125 mV) magnitude with a negative shift indicating a cathodic inhibition preference. The varying anti-corrosion properties can be influenced by the pore structure. The lower pore size of ZnO_l@PDA-DC might be creating a better barrier between the zinc oxide and the electrolyte during the electrochemical process, reducing the number of exposed electrochemical active sites. Making the corrosion protection due to the barrier protection of the coating. It was reported that in general low I_{corr} and high E_{corr} indicate better corrosion protection [25].

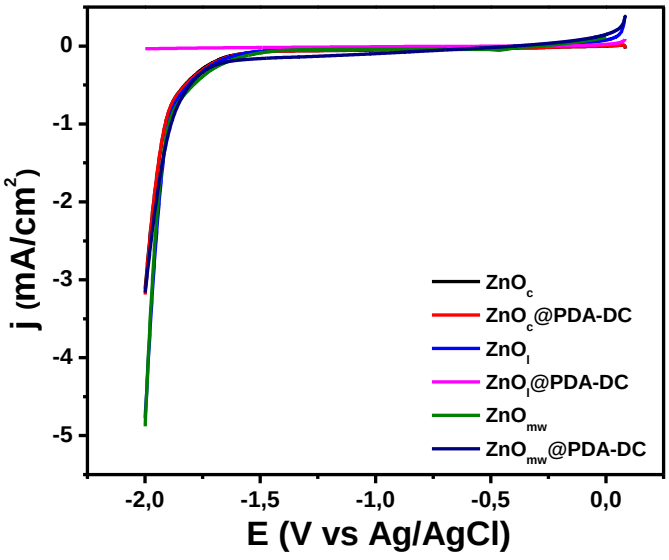

Figure 6.8: Hydrogen evolution reaction (HER) of ZnO and ZnO@PDA-DC in 6 M KOH.

Figure 6.7c shows the kinetics of the prepared ZnO and ZnO@PDA-DC nanocomposites depicted from the electrochemical impedance. EIS has been used to understand the electrochemical behaviour of the corroding system [23]. The EIS parameters of the studied materials are summarised in Table 6.2. The semicircles in the high-frequency region and the slopes in the low-frequency region depict charge transfer resistance (R_{ct}) and ionic diffusion impedance (W), respectively. The R_{ct} can be used to determine the rate of corrosion [23]. While the CPE was associated with the thickness of the protective film of the inhibitor molecules [23]. In terms of corrosion inhibition studies, a higher R_{ct} value is the reflection of a barrier that is created that needs to be overcome in order to promote the charge transfer during corrosion, which is an indication of decreased corrosion rate [19]. The Nyquist plot of ZnO_l@PDA-DC showed the highest R_{ct} frequency with a larger capacitive loop indicative of the highest adoption meaning a reduced charge transfer and corrosion rate. This was due to the low electrical conductivity of polydopamine-derived carbon. The increase in the diameter of the Nyquist plots upon adding an inhibitor can be attributed to the inhibitor adsorption at the metal/solution. A slight R_{ct} change could be observed for ZnO_c@PDA-DC. It can be seen that the ZnO_{mw}@PDA-DC anode nanocomposite had a lower semicircle radius than the ZnO_{mw} anode, which confirmed its lower charge transfer resistance. The lower R_{ct} values of ZnO_{mw}@PDA-DC and ZnO_{mw}@PDA-DC corresponded to the performance observed from OCP. The inhibitor efficiency was calculated from equation 6.7:

$$\eta_{EIS}\% = \frac{R_{ct}^{inh} - R_{ct}}{R_{ct}^{inh}} \quad (6.7)$$

where R_{ct}^{inh} is the resistance of the material with an inhibitor and R_{ct} is the resistance without the inhibitor [23]. ZnO_l@PDA-DC showed 99.86% inhibition efficiency indicating good corrosion resistance.

Table 6.3: EIS parameters of ZnO and ZnO@PDA-DC at i_{corr} in 6 M KOH.

EIS parameters	ZnO_c	ZnO_c@PDA-DC	ZnO_l	ZnO_l@PDA-DC	ZnO_{mw}	ZnO_{mw}@PDA-DC
R_s (Ω)	2.10 ± 0.09	1.18 ± 0.11	4.40 ± 0.02	0	24.76 ± 0.04	7.92 ± 0.22
CPE_1 ($\mu F.s^{\wedge(a-1)}$)	0.11 ± 0.12	0.11 ± 0.08	34.94 m ± 0.64m	96.75μ ± 6.26μ	1.34 ± 0.13	6.69 ± 0.04
a	1	1	1	1	0.69	0.91
R_{ct} (Ω)	5.43 ± 0.12	6.08 ± 0.09	13.62 ± 0.12	9589 ± 0.82	233.3 ± 0.63	28.08 ± 0.21
CPE_2 ($\mu F.s^{\wedge(a-1)}$)	24.67 ± 1.24	30.67 ± 1.39	73.43 ± 1.16	23.89 ± 0.66	93.8 ± 0.77	90.87 ± 0.59
W ($p\Omega.s^{-1/2}$)	67.55 ± 0.02	61. 61 ± 0.15	63.94 ± 4.18	1651 ± 0.65	55.85 ± 0.05	45.36 ± 0.01
$\eta_{EIS}\%$	-	10.69	-	99.86	-	-

6.3.3. Rechargeable Zinc-air battery

Due to the good inhibition effect of ZnO_l@PDA-DC over other studied electrocatalysts, the material was further used to analyse its performance in a RZAB. Figure 6.9a represents the peak power density of the material recorded at 33.2 mW/cm^2, with an OCV of 1.4 V. Figure 6.9b shows ZnO_l@PDA-DC anode cycled at 15 mA/cm^2, at 3 h charge and discharge cycles. The discharge time decreased with each discharge cycle, this might be due to zincate ion migration when deep cycling the material at 15 mA/cm^2 (Figure 6.9b). This was also evidenced by the deposition of zinc outside of the core shell (Figure 6.10). This might be caused by an accelerated zinc dissolution which mechanically stresses the structure forcing some zincate ions to leave the shell. On the other hand, the shallow charge-discharge performance of the material was evaluated at 2 mA/cm^2 in Figure 6.9c. The battery managed to cycle to 150 h (225 cycles) with a stable charge-discharge voltage gap of 0.76 V to 0.8 V. Under shallow charging the polydopamine coating was effective serving as an electrical pathway for the migration of OH^- ions while preventing zincate ion migration. More studies need to

be conducted with a focus on the use of ZnO pathway materials as anode materials in secondary zinc-air battery in order to improve its reversibility for deep cycling.

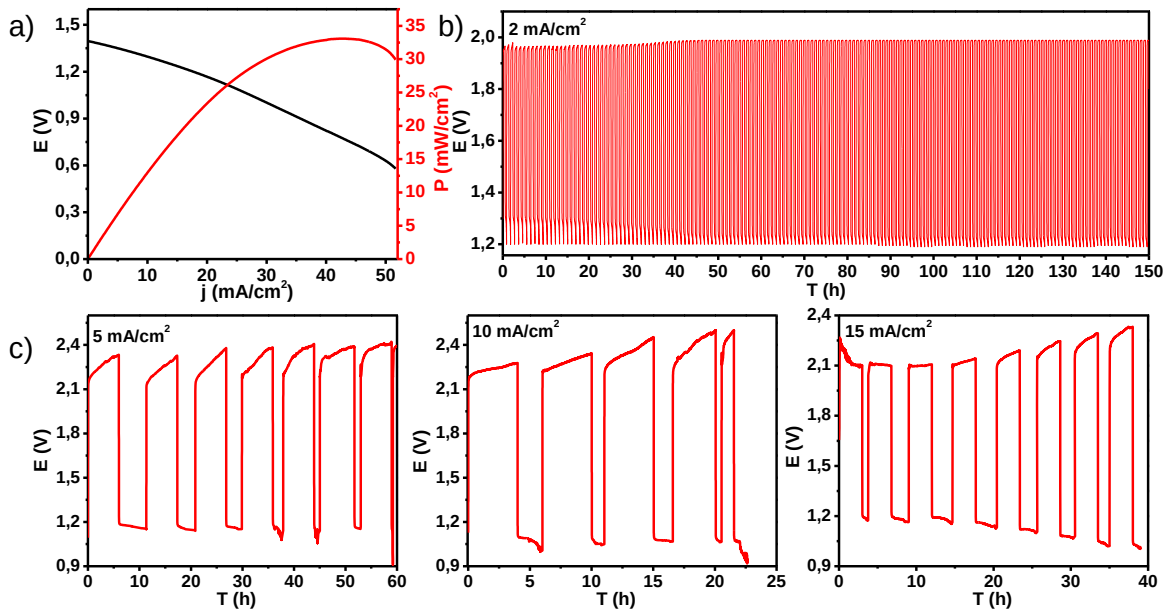

Figure 6.9: ZnO_l@PDA-DC (a) Peak Power density, (b) Galvanostatic discharge curves at a fixed current density of 5 mA/cm^2 at 6h charge-discharge and (c) Galvanostatic discharge curves at a fixed current density of 2 mA/cm^2 at 40 min charge-discharge in 6 M KOH and 0.2 M zinc acetate solution.

Figure 6.10: Deeply cycled free-standing ZnO_l@PDA-DC in 6 M KOH and 0.2 M zinc acetate solution

6.4. Conclusion

The corrosive behaviour of polydopamine-coated ZnO materials as potential anode materials in the application of RZAB has been studied. The study investigated different types of zinc oxide coated with polydopamine towards corrosion inhibition behaviour. The results showed ZnO_l@PDA-DC to have the best corrosion inhibition response with low i_{corr} (0.107 $\mu A/cm^2$) and E_{corr} (1.079 V) and a higher CPE of 74.03% (ZnO_c@PDA-DC (22.89%) and ZnO_l@PDA-DC (20.28%)) in 6 M KOH. Its Tafel polarisation study showed mixed-type inhibition behaviour with anodic predominance. EIS study revealed a high polarisation resistance of 99.86%, influenced by the coating thickness due to the difference in electrolyte adsorption at the metal/solution interface. The battery performance of ZnO_l@PDA-DC was investigated with shallow and deep charging where the battery could sustain over 150 cycles at 2 mA/cm^2. The material proved to solve ZnO passivation and zincate dissolution. However, the material showed discharge limitation under deep cycling with cycle time maintained for 35 h. Further studies still need to be conducted to improve the deep cyclability of ZnO pathway anode materials.

6.5. References

[1] A.K. Ipadeola, A.B. Haruna, L. Gaolatlhe, A.K. Lebechi, J. Meng, Q. Pang, K. Eid, A.M. Abdullah, K.I. Ozoemena, Efforts at enhancing bifunctional electrocatalysis and related events for rechargeable zinc-air batteries, ChemElectroChem 8 (2021) 3998-4018. doi.org/10.1002/celc.202100574.

[2] A.K. Ipadeola, A.K. Lebechi, L. Gaolatlhe, A.B. Haruna, M. Chitt, K. Eid, A.M. Abdullah, K.I. Ozoemena, Porous high-entropy alloys as efficient electrocatalysts for water-splitting reactions, Electrochem Commun 136 (2022) 107207. doi.org/10.1016/j.elecom.2022.107207.

[3] Z. Li, X. Hu, J. Kang, X. Wang, L. Kong, Z. Shi, Z. Wang, Porous ZnO nanosphere inherently encapsulated in carbon framework as a high-performance anode for Ni-Zn secondary batteries, Front Chem 10 (2022) 936679. doi.org/10.3389/fchem.2022.936679.

[4] M. Schmid, M. Willert-Porada, Zinc particles coated with bismuth oxide-based glasses as anode material for zinc air batteries with improved electrical rechargeability, Electrochim Acta 260 (2018) 246–253. doi.org/10.1016/j.electacta.2017.12.041.

[5] J. Fu, Z.P. Cano, M.G. Park, A. Yu, M. Fowler, Z. Chen, Electrically rechargeable zinc–air batteries: Progress, challenges, and perspectives, Advanced Materials 29 (2017) 1604685. doi.org/10.1002/adma.201604685.

[6] D. Stock, S. Dongmo, F. Walther, J. Sann, J. Janek, D. Schröder, Homogeneous coating with an anion-exchange ionomer improves the cycling stability of secondary batteries with zinc anodes, ACS Appl Mater Interfaces 10 (2018) 8640-8648. doi.org/10.1021/acsami.7b18623.

[7] L. Zhang, S. Roy, Y. Chen, E.K. Chua, K.Y. See, X. Hu, M. Liu, Mussel-inspired polydopamine coated hollow carbon microspheres, a novel versatile filler for fabrication of high-performance syntactic foams, ACS Appl Mater Interfaces 6 (2014) 18644-18652. doi.org/10.1021/am503774a.

[8] Y. Jiang, Y. Lu, L. Zhang, Preparation and characterization of silver nanoparticles immobilized on multi-walled carbon nanotubes by poly(dopamine) functionalization, Journal of Nanoparticle Research 14 (2012) 938. doi.org/10.1007/s11051-012-0938-x.

[9] R. Sa, Y. Yan, Z. Wei, L. Zhang, W. Wang, M. Tian, Surface modification of aramid fibers by bio-inspired poly(dopamine) and epoxy functionalized silane grafting, ACS Appl Mater Interfaces 6 (2014) 21730-21738. doi.org/10.1021/am507087p.

[10] H.D. Zhang, A.Y. Chen, B. Gan, H. Jiang, L.J. Gu, Corrosion protection investigations of carbon dots and polydopamine composite coating on magnesium alloy, Journal of Magnesium and Alloys 10 (2022) 1358-1367. doi.org/10.1016/j.jma.2020.11.021.

[11] N.K. Devaraj, T.C. Han, P.L. Low, B.H. Ong, Y.K. Sin, Synthesis and characterisation of zinc oxide nanoparticles for thermoelectric application, Materials Research Innovations 18 (2014) S6-350-S6-353. doi.org/10.1179/1432891714Z.000000000980.

[12] Y. Wu, Y. Zhang, Y. Ma, J.D. Howe, H. Yang, P. Chen, S. Aluri, N. Liu, Ion-Sieving carbon nanoshells for deeply rechargeable Zn-based aqueous batteries, Adv Energy Mater 8 (2018) 1802470. doi.org/10.1002/aenm.201802470.

[13] S. Alamdari, M. Sasani Ghamsari, C. Lee, W. Han, H.-H. Park, M.J. Tafreshi, H. Afarideh, M.H.M. Ara, Preparation and characterization of zinc oxide nanoparticles using leaf extract of sambucus ebulus, Applied Sciences 10 (2020) 3620. doi.org/10.3390/app10103620.

[14] A. Taufiq, H.N. Ulya, J. Utomo, N. Hidayat, Structural, optical, and antifungal characters of zinc oxide nanoparticles prepared by sol-gel method, IOP Conference Series: Journal of Physics: Conference Series 1093 (2018) 012001.

[15] H. Luo, C. Gu, W. Zheng, F. Dai, X. Wang, Z. Zheng, Facile synthesis of novel size-controlled antibacterial hybrid spheres using silver nanoparticles loaded with poly-dopamine spheres, RSC Adv. (2015) 13470-13477. doi.org/10.1039/c4ra16469e.

[16] F. Ghorbani, A. Zamanian, B. Torabinejad, The effect of oxygen plasma pretreatment on the properties of mussel-inspired polydopamine-decorated polyurethane nanofibers, Journal of Polymer Engineering 40 (2020) 109-119.

[17] W. Sheng, W. Li, G. Zhang, Y. Tong, Z. Liu, Study on the UV-shielding and controlled-release properties of a polydopamine coating for avermectin, New Journal of Chemistry 39 (2015) 2752–2757. doi.org/10.1039/c4nj01744g.

[18] S. Liu, Y. Chen, C. Liu, L. Gan, X. Ma, J. Huang, Polydopamine-coated cellulose nanocrystals as an active ingredient in poly(vinyl alcohol) films towards intensifying packaging application potential, Cellulose 26 (2019) 9599-9612. doi.org/10.1007/s10570-019-02749-7.

[19] D.S. Chauhan, K.R. Ansari, A.A. Sorour, M.A. Quraishi, H. Lgaz, R. Salghi, Thiosemicarbazide and thiocarbohydrazide functionalized chitosan as ecofriendly corrosion inhibitors for carbon steel in hydrochloric acid solution, Int J Biol Macromol 107 (2018) 1747–1757. doi.org/10.1016/j.ijbiomac.2017.10.050.

[20] S. Schilling, A. Janssen, N.J. Zaluzec, M.G. Burke, Practical aspects of electrochemical corrosion measurements during in situ analytical transmission

electron microscopy (TEM) of austenitic stainless steel in aqueous media, Microscopy and Microanalysis 23 (2017) 741–750. doi.org/10.1017/S1431927617012314.

[21] D.D. Thiruvoth, M. Ananthkumar, Evaluation of cerium oxide nanoparticle coating as corrosion inhibitor for mild steel, Mater Today Proc (2021). doi.org/10.1016/j.matpr.2021.08.157.

[22] H.-H.S. Philippe Marcus, Corrosion mechanisms in theory and practice third edition, 2012.

[23] M.A. Quraishi, D.S. Chauhan, V.S. Saji, Heterocyclic organic corrosion inhibitors, 2020.

[24] M. Nawaz, R.A. Shakoor, R. Kahraman, M.F. Montemor, Cerium oxide loaded with Gum Arabic as environmentally friendly anti-corrosion additive for protection of coated steel, Mater Des 198 (2021) 109361. doi.org/10.1016/j.matdes.2020.109361.

[25] M. Zhang, H. Wang, T. Nie, J. Bai, F. Zhao, S. Ma, Enhancement of barrier and anti-corrosive performance of zinc-rich epoxy coatings using nano-silica/graphene oxide hybrid, Corrosion Reviews 38 (2020) 497-513. doi.org/10.1515/corrrev-2020-0034.

CHAPTER 7
CONCLUSION AND RECOMMENDATIONS

This chapter summarises the conclusions of all the results obtained in this thesis and makes recommendations for future work.

7.1. Conclusion

Co atomic clusters MOF-derived carbon for high performance oxygen electrochemistry and rechargeable zinc-air battery

MOF was successfully used as a sacrificial template for the synthesis of Co MOF-derived carbon through a microwave-assisted method. After carbonisation, the Co nanoparticles (Co NP@C_{BPDC}) were covered with carbon derived from MOF. Surface treatment was strategically used on the Co NP@C_{BPDC} to remove the Co nanoparticles and create surface defects to form Co atomic clusters (Co AC@C_{BPDC}). Comparative physical characterisation techniques supported enhanced properties of Co AC@C_{BPDC} to Co NP@C_{BPDC} in terms of increased surface defects and high surface area for redox processes. OER and ORR of Co AC@C_{BPDC} continued to show improved performance to Co NP@C_{BPDC}.

As a proof of concept in RZAB the Co AC@C_{BPDC}/CB exhibited impressive OCV (1.23 V) and long-term stability for 210 h. The cell achieved Coulombic efficiency of ca. 100 % and 51.3% DOD. The performance was benched marked to reported literature which showed comparable response. The real-life practicality of the fabricated parallel plate RZAB was explored by lighting a 1.6 V bulb with excellent brightness. The all-solid-state RZAB showed a constant OCV (1.73 V) at varied bending angles (0 – 180 ^{o}C) and achieved excellent stability at 180 ^{o}C. This work showed the versatility of acid-treated MOF-derived carbon derivatives as highly active electrode materials for energy storage and conversion devices.

Noble metal-free bifunctional high-entropy spinel oxide for reversible zinc-air battery

A new and simple synthesis approach for the preparation of HEMs and the effect of annealing temperature (HESOx-500 and HESOx-750) on OER and ORR was explored. The synthesis approach was compared to what has been reported on HEMs. The materials prepared were of pure spinel phase with no trace of wurtzite or tenorite detected in the diffraction pattern. The effect of increasing annealing temperature resulted in HESOx with bigger particle sizes. Observed broader Raman modes have indicated the presence of lattice distortion in the prepared materials. The entropy stabilisation effect prevented metals from separating as evidenced by an even metal distribution. The porous structure of HESOx-500 allowed for the creation of oxygen vacancies from EPR and XPS. Though HEMs are normally prepared at high temperatures, low low-temperature annealing approach has shown to result in some beneficial properties for oxygen reactions.

In a three-electrode system, HESOx-500 showed higher oxygen redox properties attributed to the presence of a porous structure and higher oxygen vacancies. Its BI was the smallest at 0.69 V even outperforming Pt/C and IrO_2. Under a two-electrode system a two-electrode system, the OCV observed for HESOx-500 was 1.71 V and 1.66 V for Pt/C/IrO_2. However, the peak power density of HESOx-500 (136 mW/cm^2) was smaller than that of Pt/C/IrO_2 (212 mW/cm^2). A similar response was observed for their areal capacity. Its initial discharge voltage of the standard was reported at 1.30 V which quickly deteriorated to 1.00 V, this might be due to the detachment of Pt/C from the support and agglomeration during cycling. While IrO_2 might be subject to dissolution in the highly concentrated electrolyte. HESOx-500 on the other hand showed a steady state discharge plateau with a normal degradation profile caused by zinc depletion. The material underwent continuous discharge-charge cycling at a current density of 10 mA/cm^2 for 374 h. It was further used for proof of concept to light a 1.6 V LED. This work has proved that Pt/C/IrO_2 can be replaced in oxygen reactions by non-noble metals. Though they have high power the material has stability issues and will not be an appropriate material to be used in applications that require long-term cycling.

Polymer-coated zinc oxide: a promising anode material for next-generation rechargeable zinc-air batteries

Numerous types of research conducted on the evolution of the performance of cathode materials have proven to be the pitfalls to cell death. Though a flow battery can be employed, this work has looked at an alternative anode material to a zinc plate. Corrosion studies demonstrated superior corrosion inhibition properties of ZnO_I@PDA-DC compared to the other studied materials in a highly alkaline electrolyte (6 M KOH). This suggests the PDA-DC coating effectively shields the ZnO, influencing how the electrolyte interacts with the anode surface.

At shallow charge depths, ZnO_I@PDA-DC electrodes exhibited stable performance over 150 cycles at a low current density (2 mA/cm^2). This suggests the coating mitigates ZnO passivation and zincate dissolution, which are common problems during cycling. However, the material showed discharge limitation under deep cycling. This work demonstrates the potential of PDA-DC coating for significantly improving the corrosion resistance of ZnO anodes in ZABs. The enhanced stability allows for longer battery life, particularly at shallow charge depths. However, further development is necessary to address limitations during deep discharge cycles.

7.2. Recommendations

- Explore MOF-derived carbons with higher conductive properties as well as the incorporation of nitrogen-containing ligands or nitrogen-doping of carbon layer to prevent the aggregation and leaching of nanoparticles during carbonisation.
- Stabilise the 3d empty or semi-empty orbits of by filling the oxygen vacancies.
- Further research is needed to address the power limitations in the power density of HEMs. This could be achieved by optimising element selection by exploring compositions with non-equimolar ratios or strategically incorporating additional elements. Controlled synthesis of nanostructured HEMs with high surface area as well as creation of composite of HEMs.
- Further research is needed to improve the performance of ZnO_I@PDA-DC under deeper cycling conditions. Other coating materials that will be studied should be more mechanically resistant to high cycling stress.
- More focus needs to be shifted to investigating alternative zinc anode materials such as the zinc sponge as it has more advantages in addressing issues associated with the degradation of the anode.
- Up-scaled RZABs need to be exposed to test the material's viability. Real-life concepts for recharging ZABs need to be implemented. Like the use of solar to recharge the cell.
- Benchmarks need to be made for the analysis of RZABs in order for research to have the same harmony and be more forward-looking. This will assist in pushing materials from the lab to bigger scaled-up set-ups and eventually industrial applications.